



Vrije Universiteit Brussel

FACULTEIT WETENSCHAPPEN EN BIO-INGENIEURSWETENSCHAPPEN

Anomalous Project

Couplings

Progress Report and documentation of Tools

Annik Olbrechts

Started 4 April 2014
Version: July 24, 2015



Contents

1	Pending issues	1
2	Used Tools and Techniques	3
2.1	FeynRules	3
2.2	MadGraph	3
2.3	MadWeight	4
2.3.1	Synchronizing MadWeight with localgrid submission	5
2.3.2	Influence of the used Transfer Function	6
2.4	MadAnalysis	6
2.4.1	Content of analysis file in MadAnalysis	7
2.4.2	Analyzing the MadGraph files	7
3	Generator level bottlenecks	9
3.1	Uncorrect $\ln(\mathcal{L})$ minimization	9
3.1.1	Control check: Top Mass Measurement	12
3.1.2	Influence of the acceptance term	13
3.1.2.1	Understanding 1D-variation of V_L	14
4	Transfer Functions	19
4.1	Creation of the Transfer Function	20
4.1.1	Used analysis files	21
4.1.2	Applied $ \eta $ binning	22
4.1.3	Implementation in MadWeight – NEED TO UPDATE!	23
4.2	Obtained distributions	25
4.3	Control checks for Transfer Functions	25
5	Preliminary Results	29
5.1	Results on reconstructed level	29
5.2	Background influence	29
6	Understanding MadWeight Results	31
6.1	Comparing the two used MadWeight versions	31
6.2	Individual weight distribution for considered gridpoints	32
7	Analyzing FeynRules model	35
7.1	Normalized coupling parameters	35
7.2	Understanding parameters larger than 1	35
7.2.1	Performed checks	36
7.2.1.1	Cross section change	36

7.2.1.2	Relative increase visible in XS, but not in kinematic distributions	36
7.2.1.3	Model plots for fixed Pt Cut	38
7.2.1.4	Model plots for varying Pt Cut	40
8	MadGraph/MadWeight issues	41
8.1	Discussion with Olivier Mattelaer (8-9/01/2015)	41
8.1.1	Transfer Functions	41
8.1.2	Likelihood normalization	42
8.1.3	Cluster optimization	42
8.1.4	Optimizations and bug fix	43
9	Event Selection	45
9.1	Choice of b-tag requirements	45
9.1.1	Signal vs background comparison	45
9.2	Use of m_{lb} χ^2 method for selecting the correct b-jets	46
9.3	Histograms for event selection choice	47
9.4	Considering 2 or 3 light jets	49
9.4.1	Event selection numbers comparison	49
9.4.2	Mlb-algorithm numbers comparison	50
9.4.3	Compare efficiencies for 3 rd jet with 1 st and 2 nd	51
9.4.4	Considering separate categories	52
9.4.4.1	Histograms for number of selected, b-tagged and light jets	53
9.5	Studying optimal cut on χ^2 value	53
9.5.1	χ^2 required to be smaller than 5	55
9.5.2	χ^2 required to be smaller than 3	55
9.5.3	χ^2 required to be smaller than 1	55
9.6	Influence of using p_T cuts suggested by the TOP reference selection Twiki	55
9.6.1	Influence on choice of b-tag option and use of χ^2 m_{lb} - m_{qqb} method	58
10	Event corrections and reconstruction	63
11	Theory link with partial widths	65
11.1	Partial width of top-quark decay	65
11.2	Simplification in limit-cases	66
11.2.1	Only 1 coupling non-zero	66
11.2.2	Massless b-limit	67
11.2.3	Only 1 coupling non-zero within the massless b-limit	68
11.3	Understanding symmetric behavior	70
12	Likelihood optimization	73
12.1	Comparison between correct, wrong and un-matched jet combinations	73
12.1.1	Inefficiency of MadWeight depends on category-type	75
12.2	Measurement of top-quark mass using Matrix Element Method	75
12.2.1	Improvement of top-quark mass measurement by applying cuts on -ln(\mathcal{L})	77
12.3	Measurement of right-handed vector coupling, V_R , using Matrix Element Method	78

13 Likelihood event selection	81
13.1 Issue: Change of VR not found in likelihood shape	81
14 Obtained result after applying double fit	87
14.1 Double-check of method using gR coefficient	90
14.2 Bias-dependence on used V_R value MG sample	93
14.3 Influence of tighter χ^2 cuts	94
15 Comparison of SM behaviour	95
16 Influence of generator-level event selection	99
16.1 Reweighting MadWeight probability using $\cos \theta^*$	101
16.2 Difference between $\cos \theta^*$ reweighting and acceptance normalisation	105
16.3 Applying both $\cos \theta^*$ and acceptance normalisation?	109
16.4 Adapting the implementation used	111
16.5 Ensuring $\cos \theta^*$ normalisation	117
17 Effect of applying cut on FitDeviation in stead of on χ^2	119
18 Comparision between first and second polynomial fit	121
19 Results from gR coefficient	125
19.1 Results prior to any pT-cuts	125
19.2 Results afer applying the event selection cuts	127
19.2.1 Including $\cos \theta^*$ reweighting	128
19.2.2 Adding additional constraint on slope of fit	130
19.3 Cross-section dependency	132

Chapter 1

Pending issues

- Does this created FeynRules model still contain Effective Field Theory?
- If the kinematics doesn't change for coupling parameters larger than 1, how is it then possible to differentiate the different configurations which will be studied?
- Understand *CorrectPhi* comment in MadWeight name
→ Maybe related with phi issues of neutrino's ...
- EventWeight calculated in analyzer should be integrated into MadWeight output
(Should MadWeight weight just be multiplied with the EventWeight for each event?)
Otherwise all the effort to include JES and PU has no influence at all.
- Update EventNumberInformation file to only cout the information when the event has passed the eventSelection requirements. Otherwise just discard this event from the output file in order to avoid a long .txt file and long running time ...
- Construct nTuple in such a way that the likelihood and weight distributions can be calculated for specific p_T cuts without having to run the entire base code again. So perhaps also necessary to include some of the different python scripts which have been created. Hence avoid spending too much time on improving them.
- Need to understand how MadWeight deals with the permutations ... Should this permutation of the light jets be done within MadWeight or should two .lhco files be created and sent separately to MadWeight. If the latter is the case, how should they be combined afterwards ?
- Specific MadWeight question for the latest version:
The 'refine' option allows you to relaunch the computation of the weights which have a precision lower than X. But how can you find this precision?
- Should a ScaleFactor correction be applied for the Branching ratio ?
This is not the case in code of James, but should find recommendations somewhere.
- **To Check:** Does MadWeight give a different weight when the Neutrino Mass changes?
→ Currently mass is manually set to zero ...
- Check whether the created root file can be trusted when the number of considered b-tags is greater than 1 ... *Why this comment??*

Chapter 2

Used Tools and Techniques

2.1 FeynRules

Should be understood why the mass of the top quark is equal to 180 within the created FeynRules model!

2.2 MadGraph

In the beginning of this analysis only the MadGraph version *MadGraph_v155* was used since this was the v1511 version was not compatible with the FeynRules version used to create the model¹ A newer MadGraph version *MadGraph5_aMC@NLO* was released in the spring of 2014, together with a new *MadWeight* version. Finally in January 2015 a more up-to-date version of this *MadGraph5_aMC@NLO* release has been installed.

The different versions currently installed on the m-machines are:

```
/user/aolbrech/AnomalousCouplings/MadGraph_v155  
/user/aolbrech/AnomalousCouplings/MadGraph_v1511  
/user/aolbrech/AnomalousCouplings/MadGraph5_aMC@NLO/madgraph5  
/user/aolbrech/AnomalousCouplings/MadGraph5_aMC@NLO/MG5_aMC_v2_2_2
```

In this analysis MadGraph is only used to create .lhe files and study the variation of the cross section in order to understand the created model. The following two python scripts have been created for this reason:

RVL_RVR_XSGrid.py & *XSScript.py*

The first script automatically creates all the desired configurations for different RVL, RVR, Lepton Pt Cut and Jet Pt Cut values and stores them in the desired output directory. In order to save some disk space the events.lhe file is deleted directly and only the unweighted_events.lhe files are kept for analysis².

The second script loops over all the different directories and creates a .txt table and a .pdf table with the cross section results.

¹According to a mail of Olivier Mattelaere on 6 Feb 2014 the newer version is now compatible as well.

²According to Alexis the unweighted_events.lhe are the only relevant ones. *Still need to understand what is the difference between the two*

In order to use MadGraph and calculate the cross section values for the desired processes and decay channels the following commands should be used³:

```
./bin/mg5_aMC
import model MassiveLeptons(-MassiveLeptons)
generate pp > tt ~, (t > bw+, w+ > mu + vm)
           , (t ~> b ~ w-, w- > jj) @1 QED = 2
output Name
exit
```

The *index.html* file in the created directory contains all the Feynmann Diagrams of to the generated process and can be opened using *firefox* on mtop. When saved in .ps format the resolution is good enough to include in PDF documents.

The FeynRules model is created in such a way that it contains a **NP**, **QCD**, **QED** and **TEST** variable representing the different interaction vertices. Hence asking **QED** = 2 results in the desired 16 independent diagrams, namely an altered top quark decay while the other interaction vertices are still described by the Standard Model.

Whenever the cross section should be calculated for a specific process the following configuration files in the Cards directory should be updated:

- **run_card.dat** where the number of generated events is defined together with the beam energy of the considered collision process. This file also contains all kinematic cuts which can be applied. Since these will influence generator events they will have a different effect then the jet-level cuts applied in the event selection.
- **param_card.dat** where all the parameters of the considered model configuration can be be defined.
- **proc_card.dat** describes the type of generated event and the imported models. This file shouldn't be altered but is particularly useful to ensure that the correct event topology is considered.

Each of these files can still be adapted after the *./bin/generate_events* command since the MadGraph software always asks whether one or more of the configuration files should be changed before the command is executed (with a waiting time of 60s).

As a consequence, when using a script to run MadGraph continuously, the **me5_configuration.txt** file should be adapted to enable this waiting time. Otherwise using nohup to run the script results in a crash and the termination of the script.

2.3 MadWeight

As was the case with MadGraph, two different versions of the MadWeight event generator exist. All original tests have been performed with the older one, installed under *madweight_mc_perm*, and used until July 2014. The newer one, installed as *MadGraph5_aMC@NLO*, is supposed to be less CPU intensive and allows the user

³The model with name *MassiveLeptons-MassiveLeptons* is the one with the CKM restrictions applied and hence the FCNC decays excluded! This will result in a reduced CPU time needed.

to split the interaction points in two distinct steps. Since September 2014 this newest version is used as standard and has been updated in January 2015.

Each version can be installed using the following command:

- bzr⁴ branch lp:~maddevelopers/madgraph5/madweight
- bzr branch lp:~mg5amcnlo

After the MadWeight installation with the *bzr* command the created *MassiveLeptons* *FeynRules* model should be copied to the “model” directory. Otherwise it cannot be accessed by the MadWeight event generator. In order to generate a process with the model of choice, the following commands have to be executed:

```
./bin/mg5_aMC
import model MassiveLeptons - MassiveLeptons
generate pp > tt ~, (t > bw+, w+ > mu + vm), (t ~> b ~ w-, w- > jj) @1 QED = 2
output madweight Name
exit
```

In order to actually calculate Matrix Elements using this MadWeight software the relevant configuration files should be adapted in order to select the correct configuration. Just as was the case when using the MadGraph software, the concerned files are the **run_card.dat**, **param_card.dat** and the **proc_card.dat**.

The only relevant new card is the **MadWeight_card.dat** file where the simulated parameters of the corresponding **param_card.dat** can be introduced. For the rest this file contains all the different run options which can be set.

As a next step the correct Transfer Function should be chosen from the list of available ones. If no option is chosen within the 60s waiting time, the underlined one is chosen.

```
./bin/mw_options
define_transfer_fct
```

The actual running of MadWeight is done with the *./bin/madweight* command combined with the option *-1* to create all the *param_cards*, option *-2* to ..., option *-3* to ..., option *-4* to ..., option *-6* for actually starting to run MadWeight and afterwards with option *-8* to collect all the weights and store them in the corresponding Events directory.

2.3.1 Synchronizing MadWeight with localgrid submission

Running the MadWeight event generator is preferable done using localgrid submission since this allows to split the *.lhco* file containing all events in multiple jobs. However the standard MadWeight configuration is not directly compatible with the IIHE cluster submission. For this to work out-of-the-box the following adaptations should be done: For this first step the following two files have to be changed in the */bin/internal* directory. Both files are now included as default file in the *madgraph/interface/* and *madgraph/various/* directories respectively.

⁴The bzr package has been installed on the m-machines, but not on mtop. Due to some conflict with the *libz.so* package it cannot be executed after initializing the alias *setMGpython*.

- `madweight_interface.py`: Change ...
- `cluster.py`: Add ... on line ... and activate maximum local submission

The activation of the maximum local submission is rather important since it allows to continuously send 2000 jobs, the maximum allowed by the PBS Cluster. In case more than 2000 jobs are originally submitted this function keeps them in the queue and only submits once the number of running jobs is lower than the maximum specified.

In the **MadWeight_card.dat** file, the number of events in one job can be specified. This value should be chosen as low as possible without needing millions of jobs submitted to the cluster. The larger the number of jobs per event, the longer the run time of one job needs and the lower the priority will become. So with the possibility of specifying the maximum number of jobs which can be submitted at once, the number of jobs per event can be chosen rather low.

Once the jobs are running on localgrid their performance and running time can be checked using the `qstat` and, if needed, they can be killed using the `qdel`⁵ command.

```
qstat @cream02 | grep aolbrech & qdel XXX.cream02
```

2.3.2 Influence of the used Transfer Function

Location of script `PlotFittedPt.py` which plots the distribution of the different pT points integrated by MadWeight:

NewestMW_amcnlo_PTDependentTF/mg5amcnlo/ttbarSemiMuPlus_QED2_CKMRestrictions

2.4 MadAnalysis

Since the update of the m-machines to Scientific Linux 6 (`slc6`), MadAnalysis can only be used on `mtop`. Whenever MadAnalysis is compiled on any of the other m-machines an error message about a missing library appears, while compiling on `mtop` works without any problem.

MadAnalysis is most useful in the expert mode since this allows to develop a personal analysis file where an event selection can be applied and specific kinematic variables, such as the $\cos\theta^*$ one, can be defined. Also for MadAnalysis two different versions exist, but only the expert mode in version *v112* is compatible with the explanation in the manual (*arXiv* : 1206.1599). The expert mode of the more recent version, *v115*, does not work out-of-the-box and requires adaptations to the python files.

In order to start with a new analysis the following command has to be used:

```
./bin/ma5 --expert
```

This results in a series of questions such as the name of the directory which has to be created and the name of the analysis. The latter one should not be taken too complex since it has to be entered each time a series of plots is created for this analysis. After the

⁵Killing jobs should be avoided as much as possible since it negatively influences the priority.

desired directory is created, the *Name*/SampleAnalyzer directory should be initialized by executing the following two commands:

```
source setup.sh & make
```

The actual analysis should be created in the Analysis directory, and a similar approach as in *user.cpp* and *user.h* should be adopted. Everytime a change has been made to any these two files, *make* should be executed in the SampleAnalyzer directory in order to process the changes. The different *.lhe* files⁶ which should be considered should be defined in a *List.txt* file which is saved in the SampleAnalyzer directory.

The actual running of MadAnalysis is then done using the following command:

```
./SampleAnalyzer --analysis = "Name of analysis" List.txt
```

2.4.1 Content of analysis file in MadAnalysis

The analysis files which contain all the necessary information can be found in the following directory on the m-machines and are called *LeptonPtCutInfluence.cpp* and *JetPtCutInfluence.cpp*. They both consist of two different functions, namely the *Execute* and the *Finalize* function. The first one allows to access the information of each event while the second one is only accessed once for each file. Therefore the particle content is reconstructed in the *Execute* function and the histograms for all the considered files are constructed in the *Finalize* function.

MadAnalysis_v112/Wtb_PtCutInfluence/SampleAnalyzer/Analysis

These analyzer files look at 28 different kinematic variables, and store the kinematic information of each of the particles present in the expected semi-leptonic $t\bar{t}$ event. In order to separate the two b-quarks in the event, the Particle Id of the leptonic top quark needs to be known. Therefore an integer *LeptonicTopPdgId* is used and the kinematic information of the b-quarks can only be stored when this integer is different from zero. This will normally not result in by-passing the b-quark information since the events in the *.lhe* files are read in in the same order as they are created by the MadGraph command. So first the top quarks are considered and only then the final state particles.

2.4.2 Analyzing the MadGraph files

Currently the created model should be completely understood and the behavior of the model when the coupling coefficients are larger than 1 should be investigated. Therefore new MadGraph files have been processed for the following configuration:

$$\begin{aligned} Re(V_L) &\in [0.7, 1.3] \\ Re(V_R) &\in [-0.3, 0.3] \end{aligned}$$

These files can be found in the following directory on the m-machines and contain 100 000 events.

```
/user/aolbrech/AnomalousCouplings/MadGraph_v155/MassiveLeptons/
MadGraph5_v1_5_5/Wtb_ttbarSemiElMinus/ResultsXSGrid003
```

⁶MadAnalysis cannot process *.lhe.gz* files so they should be unpacked using *gunzip.lhe.gz*

Chapter 3

Generator level bottlenecks

The idea behind studying generator-level results is to ensure that no bottlenecks are encountered when running MadWeight. The advantage of only using these type of events is that one can be completely sure that they are actual semi-leptonic ttbar events. Hence MadWeight should not have any problems calculating the weight for these kind of events and no CPU time will be spent on uncorrect events. This implies that any deviation from the expected results implies a bias, or even a problem, concerning the MadWeight output.

Once the results correspond to the expectations, these preliminary results could be easily extended to reconstructed events. Finalizing the event selection then allows to fully trust the results obtained on reconstructed level and make sure that any new deviation can be explained by the influence of the applied event selection. These results can then be used to optimize the event selection with respect to the MadWeight output and CPU time needed.

3.1 Uncorrect $\ln(\mathcal{L})$ minimization

The first obtained results for the full grid ($V_L \in [0.8, 1.2]$ and $V_R \in [-1, 1]$) using only parton-level ttbar events did not result in the expected minimum of $(V_L, V_R) = (1, 0)$. This can be observed in Figure 3.1 which contains the distribution of the $\ln(\mathcal{L})$ for each point of the grid. Looking at these values in detail clearly shows that the minimum of this distribution can be found in both upper corners, and not in the expected center of the grid. It is even worse than at first sight, because the Standard Model value corresponds almost to the maximum of the distribution. The only two values which are still slightly higher are the $(0.9, 0.0)$ and $(0.8, 0.0)$ ones.

A possible explanation for this discrepancy is the missing normalisation of the cross section for each point in the grid. Figure 3.2 contains the relative cross section, $\frac{XS}{XS^{SM}}$, for each point in the grid and clearly shows that this distribution has the opposite behavior as the $-\ln(\mathcal{L})$. Hence normalising the MadWeight output with this relative cross section factor might result in a correct minimization.

Originally XS normalisation was applied in MadWeight, but has been removed in the MadGraph5 version. But correct implementation can easily be derived from the so-called

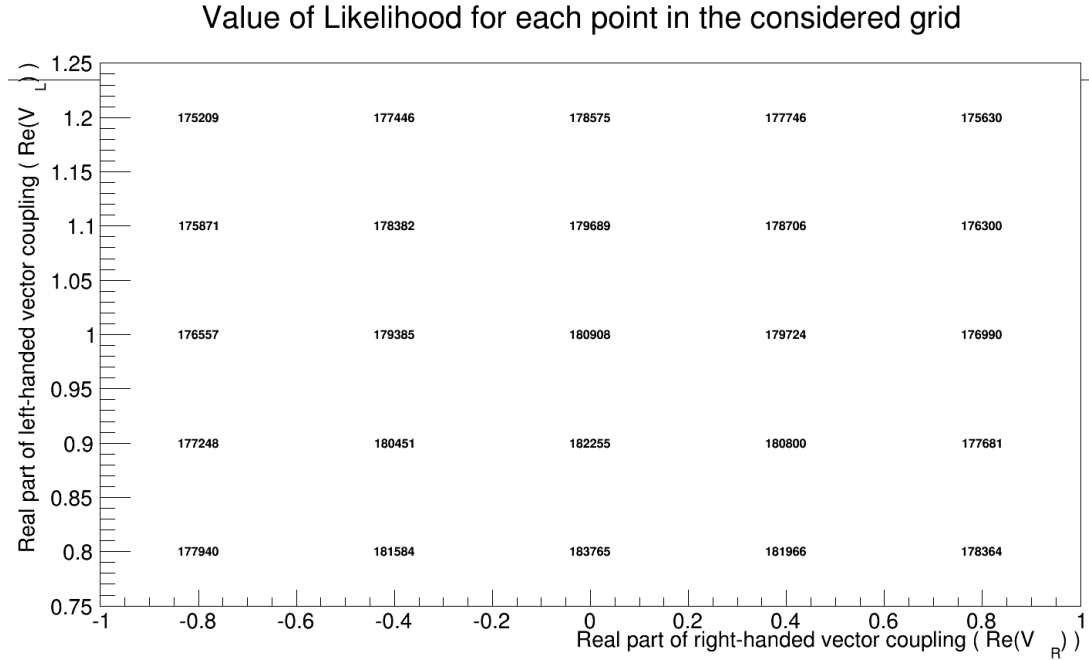


Figure 3.1: Distribution of the $\ln(\mathcal{L})$ for each point in the grid using 3200 parton-level positive semi-muonic ttbar events. The transfer function used to smear the parton-level kinematics is the single-gaussian function standard included in MadWeight.

general Matrix Element¹ formula which is given in Equation (3.1).

$$P(y|a) = \frac{1}{\sigma(a) * \text{Acc}(a)} \int W(y|x, a) |M(x, a)|^2 dx \quad (3.1)$$

$$\mathcal{L} = \prod P(y|a) \quad (3.2)$$

$$\sigma(a) = \int_{X_i} |M(x, a)|^2 dx \quad (3.3)$$

The factor $\sigma(a)$ is defined as the channel cross section and is the XS normalisation factor which should be applied. So the previous use of $\frac{XS}{XS_{SM}}$ was incorrect, especially because the new cross section value was placed in the numerator in stead of in the denominator. The additional part with normalising with respect to the Standard Model cross section, XS_{SM} , is less important because it will only introduce a general up- or down-scaling of the overall normalisation factor since it is the same for each point in the grid.

Since the negative log of the likelihood is used as MadWeight output, special care should be awarded to the correct implementation of this normalisation factor. Since it has to be applied for each weight separately, the correct formula is the one in Equation (3.4).

$$-\ln(\mathcal{L}_{Norm}) = -\ln(\sum P(y|a) * \frac{1}{XS}) = -\ln(\mathcal{L}) + N * \ln(XS) \quad (3.4)$$

After applying this normalisation, the minimization of $-\ln(\mathcal{L})$ returns the correct value for the V_R component but not for the V_L component. A possible explanation for the wrong results for the left-handed vector coupling is the fact that this parameter only influences the cross section and not the kinematics of the particles present in the decay.

¹Obtained from papers *arXiv* : 1101.2259 and *inspirehep* : 854451.

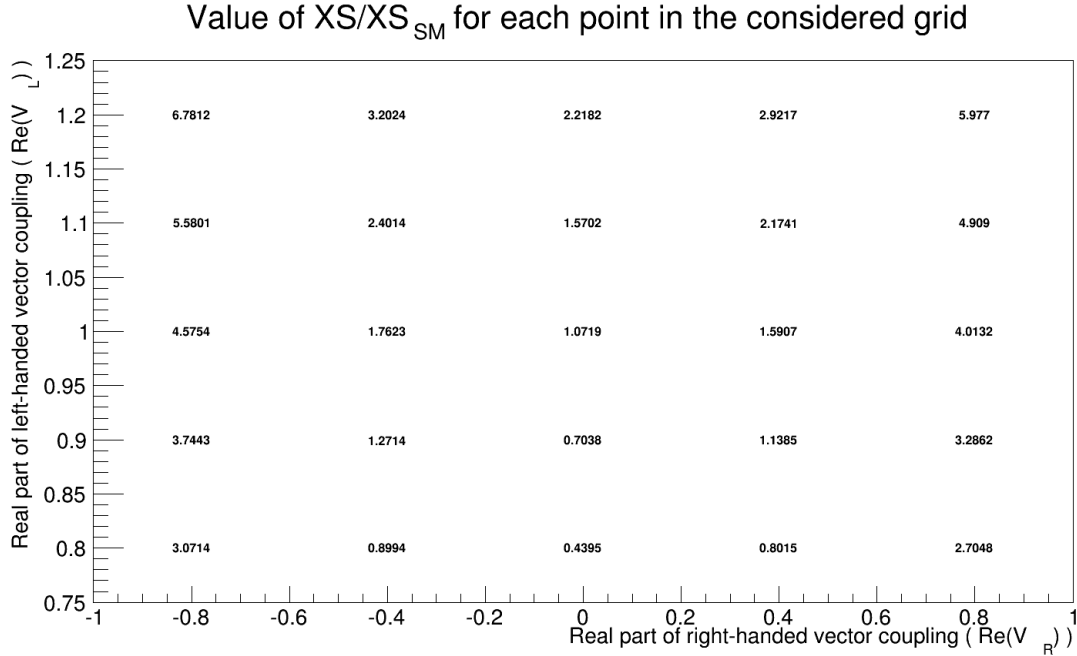


Figure 3.2: Distribution of the XS normalisation for positive semi-muonic ttbar events. As in the previous figure 3200 positive semi-muonic have been used to obtain this distribution and a single gaussian transfer function has been applied to smear the kinematics of these parton-level events.

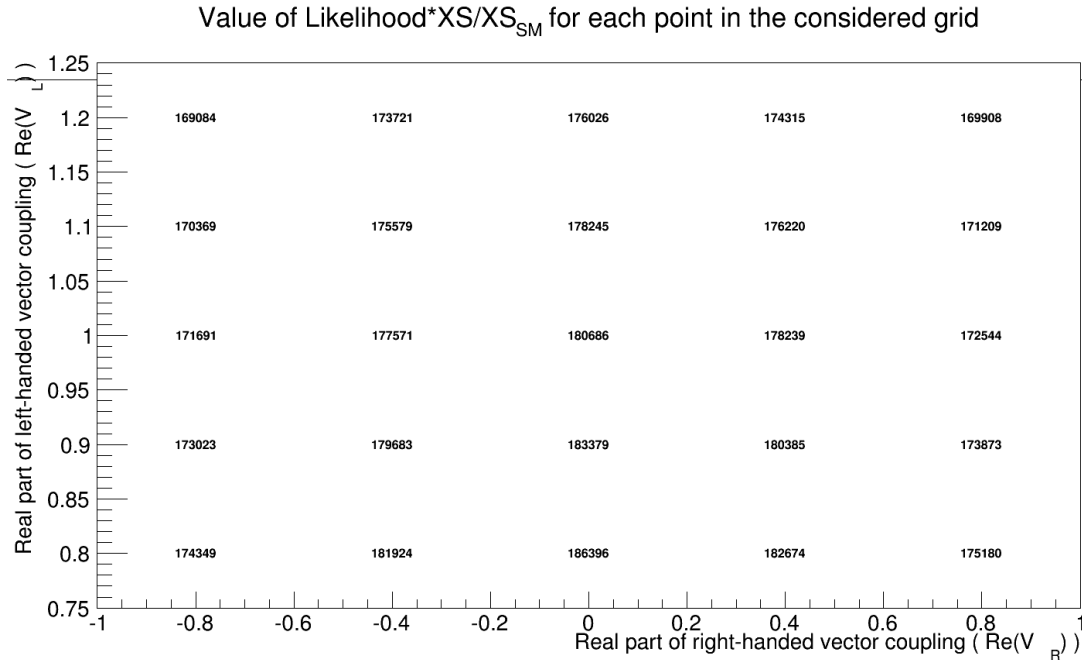


Figure 3.3: Distribution of the $\ln(\mathcal{L})$ after taking into account the XS normalisation. Again 3200 positive semi-muonic have been used and a single gaussian transfer function has been applied. **WRONG NORMALISATION!**

Hence it is possible that MadWeight is not optimized for measuring these kind of variables since it focusses on kinematic information. Variables which are directly influenced can be measured by a counting experiment, as is done for the V_L coupling in single-top events.

Some additional investigation in this subject is performed and will be discussed further.

3.1.1 Control check: Top Mass Measurement

In order to check whether this XS normalisation results in an overall influence on the obtained MadWeight output, the MadWeight generator had been used to select the most plausible top-quark mass. So instead of generator different (V_L, V_R) grid points, five different top-quark masses have been simulated. If this would also return a completely wrong, it would be an important indication of an important issue with MadWeight. This because MadWeight has already been used successfully to measure the top-quark mass.

In order to compare the top-quark mass result with the (V_L, V_R) one, a couple of additional comparisons have been performed as will be discussed in detail next. This mainly corresponds to comparing the predefined Standard Model FeynRules model with the newly created Anomalous Couplings one.

Comparing Feynman diagramsSM model with AnomalousCouplings model

As a first step the Feynmann diagrams belonging to the two different models should be compared. This information can be found in the *index.html* file in the following directories:

MadGraph5_aMC@NLO/madgraph5/SM_ttbarSemiMuPlus

MadGraph5_aMC@NLO/madgraph5/ttbarSemiMuPlus_QED2

Comparing SM cross section with MassiveLeptons cross section

In order to be sure that both models have the same Standard Model base, the cross sections for both models have been compared. This resulted in an unexpected outcome, namely that the obtained cross sections differ significantly depending on which MadGraph version is used to generate the considered events. A summary can be found in Table 3.1.

m_t	MadGraph aMC@NLO		MadGraph v155	
	SM model	MassiveLeptons model	SM model	MassiveLeptons model
153	9.23 pb	9.645 pb	6.692 pb	6.984 pb
163	11.12 pb	11.63 pb	7.844 pb	8.199 pb
173	12.98 pb	13.54 pb	8.897 pb	9.281 pb
183	14.77 pb	15.4 pb	9.884 pb	10.3 pb
193	16.5 pb	17.22 pb	10.78 pb	11.25 pb

Table 3.1: Cross section values for semi-muonic (+) ttbar decay obtained using two different MadGraph versions.

From this table can be seen that there is, for both considered MadGraph versions, a small difference between the SM FeynRules model and the MassiveLeptons one. This could be caused by the different treatment of the leptons. In the SM model they are considered to be massless while in the MassiveLeptons one they are defined to have their actual mass.

A larger difference occurs when both MadGraph versions are compared. From the answer received by Olivier it is not clear whether this difference is worrisome or could

be explained by the LO theoretical uncertainties. Should also be investigated whether this difference is related to the NLO behavior of the newest MadGraph version. In case the MadGraph v155 version is not up to NLO a difference in cross section is definitely expected.

Understanding why Top Mass simulation does result in correct Likelihood minimum

When using the *MadGraph5_aMC@NLO* MadWeight version is used to scan over the different top mass values the correct minimum is obtained directly, so without any normalisation or acceptance influences. This simulation only uses the Standard Model information and doesn't consider the AnomalousCouplings FeynRules model.

Repeat with smaller top quark differences ...

The results can be found in Table ??

m_t	Negative log likelihood ($-\ln(\mathcal{L})$)		
	MW_aMC@NLO	MW_aMC@NLO	ML model
153	196 499		118 238
163	188 002		114 778
173	181 027		112 803
183	186 284		116 174
193	192 926		119 717

Table 3.2: caption ..

3.1.2 Influence of the acceptance term

As could be seen from the general Matrix Element formula, Equation (3.1), also the acceptance $\text{Acc}(a)$ has to be taken into account. This term represents the influence of the event selection, which can be different for each point in the considered grid. Since no reconstructed events exist for the different vector coupling coefficients, the influence of the event selection is currently only be measured on generator-level². This can introduce a slight bias since applying the reco-level cuts on generator-level result in slightly tighter cuts due to the smaller width of the kinematic distributions. But it is a good way to get an idea of the influence of the event selection and, as long as a flat dependency is found throughout the vector couplings, an acceptable one.

The event selection influence is investigated by looking at the variation in cross section and influence on the kinematic distributions. The variation in cross section is measured using 1-dimensional scans of both the left-handed as right-handed vector coupling coefficients while the other is set to its Standard Model expectation value. The results are given in Table 3.3 and Table 3.4 for the 1D change of V_L and V_R , respectively. All the created MadGraph files are located in the following directory:

MadGraph5_aMC@NLO/madgraph5/TopMassCheckQED2_ttbarSemiMuPlus_ML

From these Tables can be concluded that the influence of the event selection on the cross section is flat and equal throughout the entire vector coupling grid. This would be

²A Fast/FullSim comparison should be done afterwards for a full detailed influence!

(V_L, V_R)	1D change of $\text{Re}(V_L)$		
	All events	Reco p_T cuts applied	Reduction (%)
(0.8, 0.0)	3.62605 pb	0.9423 pb	25.99
(0.9, 0.0)	5.81248 pb	1.51 pb	25.98
(1.0, 0.0)	8.85979 pb	2.30454 pb	26.01
(1.1, 0.0)	12.96357 pb	3.37064 pb	26.00
(1.2, 0.0)	18.3674 pb	4.768 pb	25.96

Table 3.3

(V_L, V_R)	1D change of $\text{Re}(V_R)$		
	All events	Recop $_T$ cuts applied	Reduction (%)
(1.0, -1.0)	37.7415 pb	11.98 pb	31.74
(1.0, -0.5)	14.5606 pb	4.466 pb	30.67
(1.0, 0.0)	8.85979 pb	2.661 pb	30.03
(1.0, 0.5)	13.1236 pb	4.04 pb	30.78
(1.0, 1.0)	33.1415 pb	10.61 pb	32.01

Table 3.4

a positive result since it would imply that no additional analytical function is necessary to normalise the MadWeight output. Hence the MadWeight output should only be normalized for the Cross Section influence, but not for the event selection one.

The influence of the event selection on the kinematic distributions is measured by comparing the distributions before and after the event selection is applied. Also here, no significant change is observed implying again that the influence of the event selection can be assumed to be flat throughout the entire grid. All the distributions can be found in the local directory *KinematicDistributions_AcceptanceTerm_Dec2014*, but the ones for the $\cos \theta^*$ variable, the p_T distribution for the lepton, for the b-quark originating from the hadronically decaying top quark and for the down-quark originating from the W-boson decay are given in Figure 3.4, Figure 3.5, Figure 3.6 and Figure 3.7, respectively.

From the distributions given here can easily be concluded that some shape differences are visible for the 1D-variation of the right-handed vector coupling. However for the left-handed one no influence is visible when varying the value of V_R , besides some negligible statistical fluctuations. It is also clear that the influence of the V_R 1D-variation is not the same for each of the kinematical distributions, and even negligible for the p_T distribution of the b-jet originating from the hadronically decaying top quark. Since the shift of the distribution is different for the p_T distribution of the lepton and the down-type quark of the W-boson, the result is still in agreement with the flat change in cross section. This because the additional events for one distribution are balanced out by the reduced number of events for another distribution resulting a net effect of zero and hence a flat behavior throughout the entire vector coupling coefficients grid.

3.1.2.1 Understanding 1D-variation of V_L

The influence of the variation of the right-handed vector coupling V_R on the kinematic distributions was rather satisfactory and in some way agreeing with expectations. How-

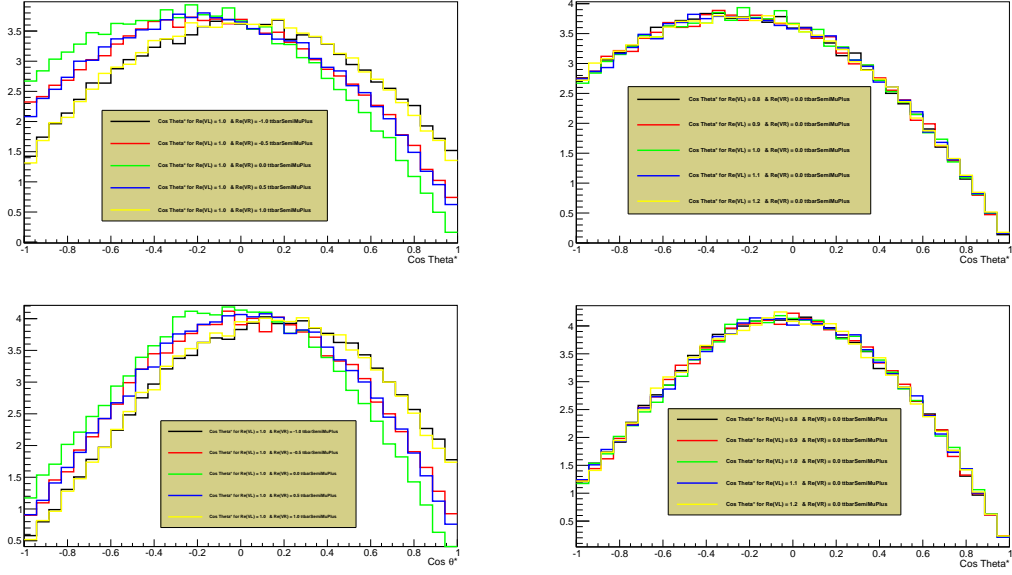


Figure 3.4: Distribution of $\cos \theta^*$ variable for both 1D-variation of the vector coupling coefficients. The top figures depict the distributions before the application of any event selection while the lower ones show the same distribution but after the reco-level p_T cuts have been applied.

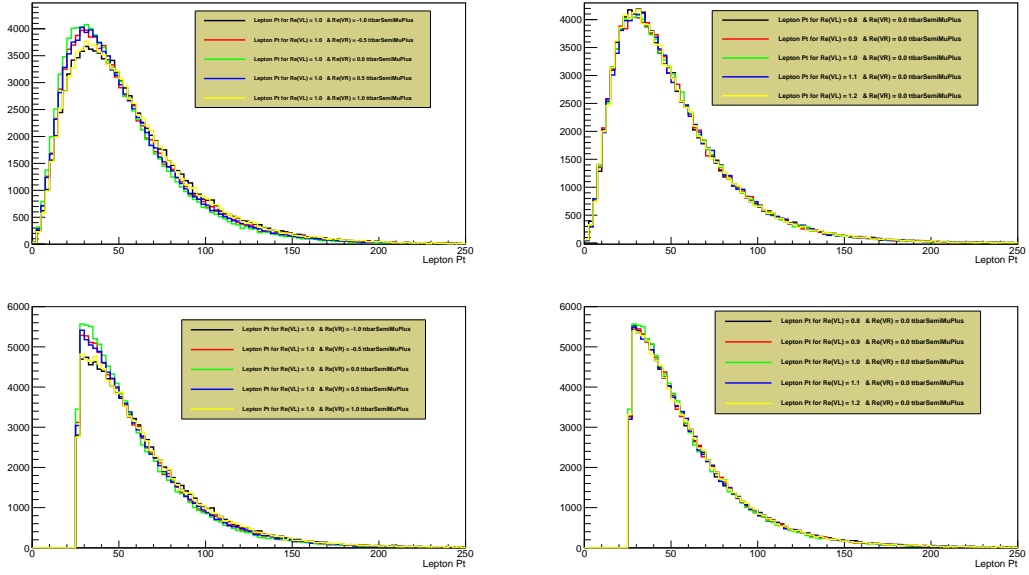


Figure 3.5: Distribution of transverse momentum of the lepton for both 1D-variation of the vector coupling coefficients. The top figures depict the distributions before the application of any event selection while the lower ones show the same distribution but after the reco-level p_T cuts have been applied.

ever the same is definitely not true for the variation of the left-handed vector coupling V_L . On the contrary, it can even be stated that the obtained result was a complete surprise and needs to be understood as soon as possible in order to keep confidence in the created FeynRules model. This because a possible explanation can still be a wrong configuration of the anomalousCouplings FeynRules model.

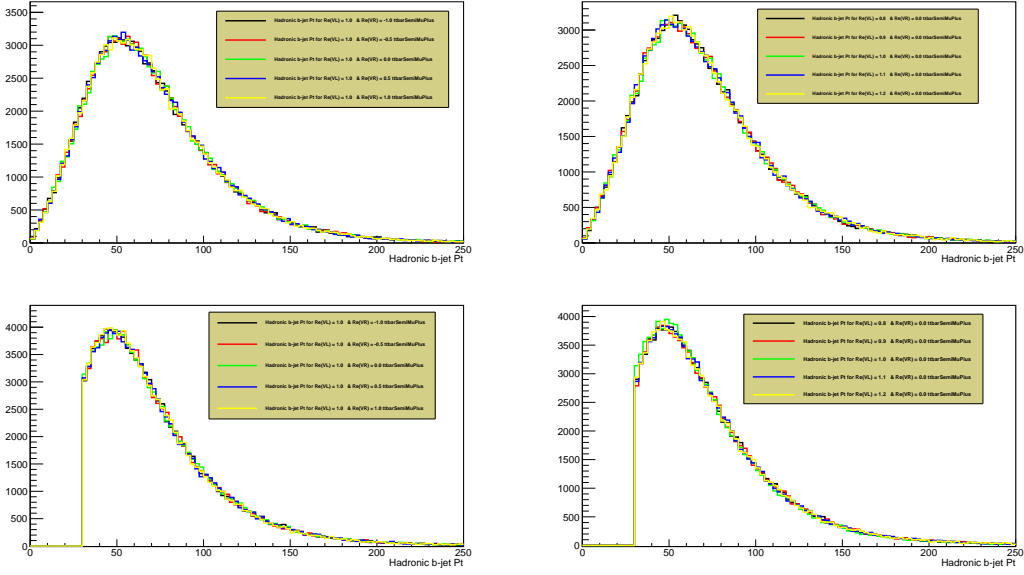


Figure 3.6: Distribution of the transverse momentum of the b-quark originating from the hadronically decaying top quark for both 1D-variation of the vector coupling coefficients. The top figures depict the distributions before the application of any event selection while the lower ones show the same distribution but after the reco-level p_T cuts have been applied.

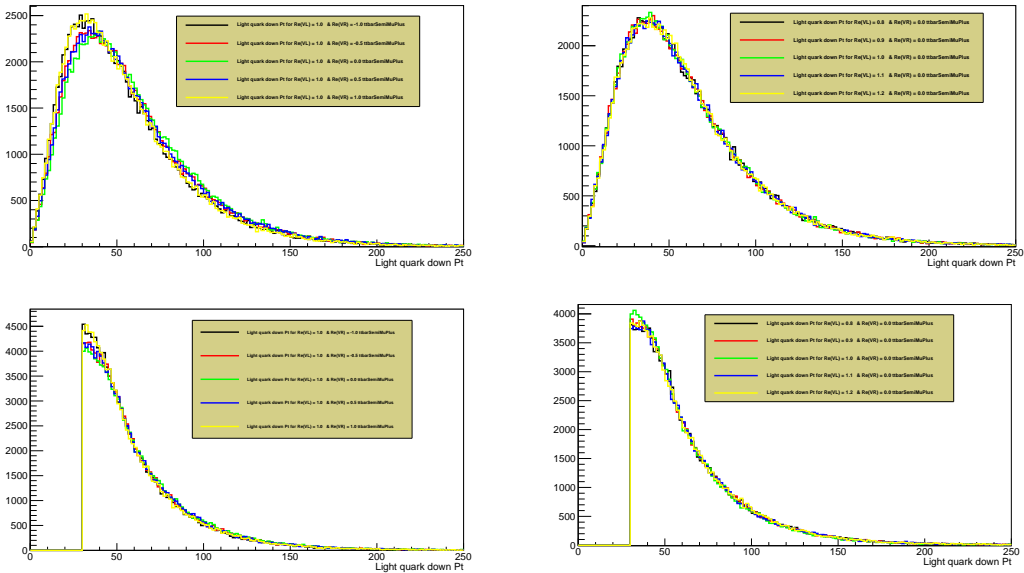


Figure 3.7: Distribution of the transverse momentum of the down-type quark originating from the W-boson for both 1D-variation of the vector coupling coefficients. The top figures depict the distributions before the application of any event selection while the lower ones show the same distribution but after the reco-level p_T cuts have been applied.

Therefore new MadGraph files, and kinematic distributions, have been created with the same 1D-variation of the left-handed vector coupling V_L but in stead of setting the V_R value equal to its Standard Model expectation of 0 it was set to 0.2. The reason behind this different value for V_R is the idea that when the right-handed vector coupling

is excluded from the full Wtb Lagrangian any change of V_L only affects the $|V_{tb}|$ value and hence the cross section. This would imply that no real change of physical concepts is done since the Lagrangian is in a sense unchanged because no mixing of the different vector couplings appears. The results for this 1D-variation can be found in Table 3.5 and in Figure 3.8, and show identical results as for the 1D-variation of V_L with V_R fixed to 0.

(V_L, V_R)	1D change of $\text{Re}(V_L)$		
	All events	Reco p_T cuts applied	Reduction (%)
(0.8, 0.2)	4.223 pb	1.201 pb	28.43
(0.9, 0.2)	6.615 pb	1.882 pb	28.45
(1.0, 0.2)	9.995 pb	2.787 pb	27.88
(1.1, 0.2)	14.46 pb	4.043 pb	27.96
(1.2, 0.2)	20.26 pb	5.695 pb	28.11

Table 3.5

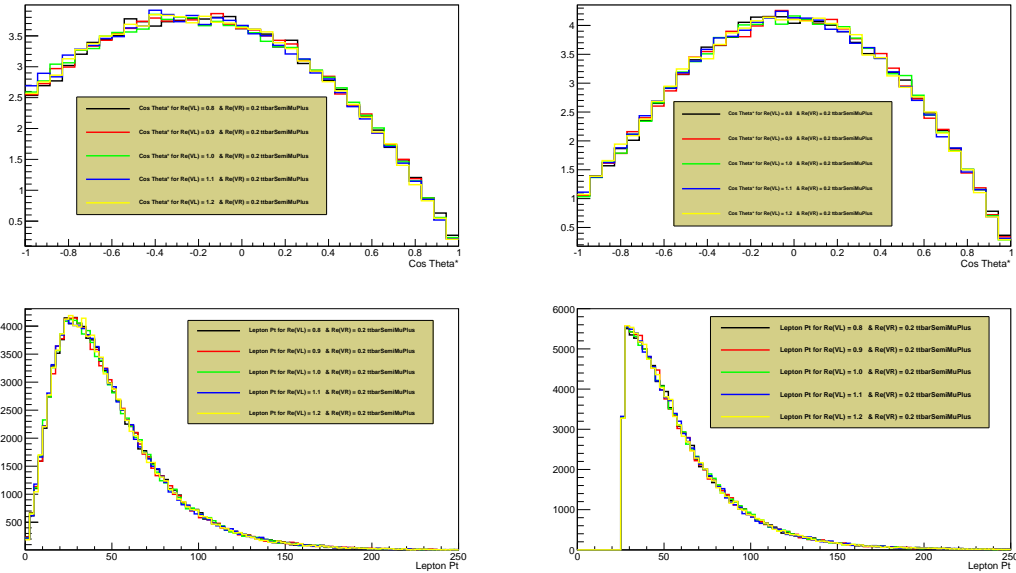


Figure 3.8

The obtained results for the 1D-variation of V_L with $V_R = 0.2$ seem to suggest that either the V_L component only influences the cross section and alters in no way the kinematic distributions or otherwise that this component is wrongly implemented in the created FeynRules model. As a final test, a larger 1D-variation of V_L is performed with the V_R component still equal to 0.2. This resulted in a slightly unexpected outcome, as can be seen in Figure 3.9, since some deviation of the kinematic distribution is found for the configuration where V_L is equal to 0. However there is no difference between the four other configurations, which is unfortunate because there was some hope that the lack of influence on the kinematic distributions for the V_L component could be caused by the small variation applied.

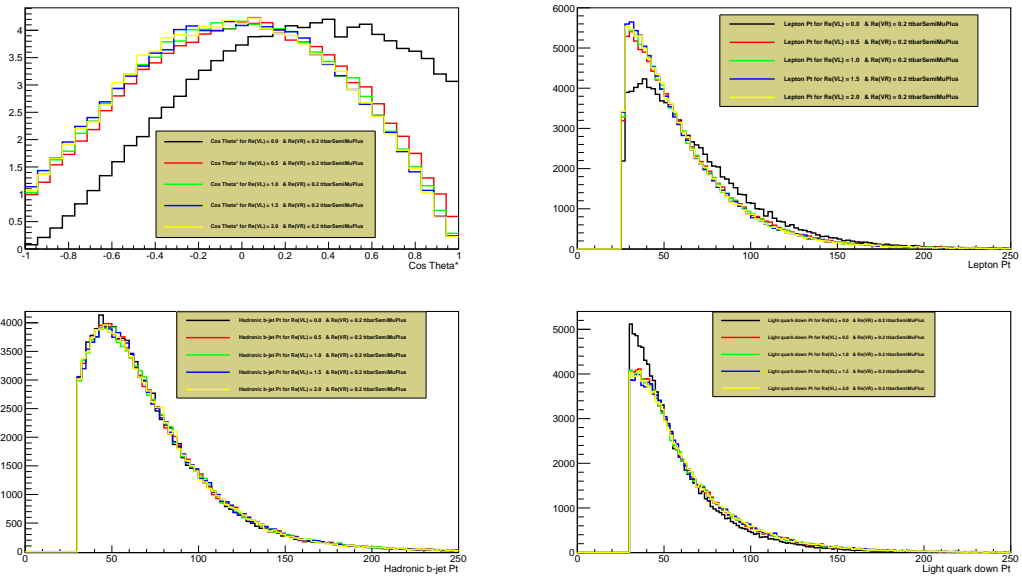


Figure 3.9

Chapter 4

Transfer Functions

In order to obtain reliable MadWeight results, the Transfer Functions which link the reconstructed energy distribution with the actual energy distributions should be taken into account. In the case of generator-level events this is less relevant since no significant smearing of the energy is expected. However in order to avoid any bias related to the used Transfer Functions it has been opted to use the constructed Transfer Functions, possibly with reduced width.

In this analysis it has been chosen to use a double Gaussian Transfer Function¹. This type of function is successful in describing both the Gaussian distribution of the peak of the distributions, but also correctly takes into account the tail. This is preferred to a single Gaussian which only fits the peak and just discards the tail of the distribution. However, as can be seen from some of the distributions further in the text, the tail can become rather significant depending on the amount of available statistics. Equation 4.1 gives explicitly the functional form of the double Gaussian fit and Equations (4.2)-(4.3) the p_T -dependent “calorimeter” formula. This name should not be taken to literally since it is only the actual calorimeter p_T -dependency for the σ -parameters (2 & 5) of the two Gaussian fits.

$$\frac{1}{\sqrt{2\pi}} * \frac{1}{a_2 a_3 + a_3 a_5} \left(a_3 \exp \left[-\frac{(x - a_1)^2}{2 * a_2^2} \right] + a_6 \exp \left[-\frac{(x - a_4)^2}{2 * a_5^2} \right] \right) \quad (4.1)$$

$$a_{x,0} + a_{x,1} \times \sqrt{p_T} + a_{x,2} \times p_T \quad (\text{for } x = 2 \& 5) \quad (4.2)$$

$$a_{x,0} + a_{x,1} \times p_T + a_{x,2} \times p_T^2 + a_{x,3} \times p_T^3 + a_{x,4} \times p_T^4 \quad (\text{for } x = 1, 3, 4 \& 6) \quad (4.3)$$

The method used to calculate the Transfer Functions is based on the *FitSlicesY()* *ROOT* class, however originally some differences existed². The most important difference between the two approaches was the treatment of the underflow and overflow bin. In the original method these two bins were added to the first and last bin, respectively, and hence included in the fit input. This is not desired since the size of the underflow/overflow bin can be relatively large compared to the first/last bin and significantly change the bin

¹Some information about this kind of TF can be found in the thesis of Arnaud Pin (cp3.irmp.ucl.ac.be/upload/theses/phd/). The main difference is that he has chosen to use only 5 parameters and hence a slightly different normalisation factor. The current definition is based on code received from Petra and Lieselotte, which has been applied in the Master Thesis of Lieselotte.

²Even after carefully ensuring that both methods are identical the obtained results were not. Up to now it is not clear what is the reason for the discrepancy between the two results and the only way to find out is comparing the distributions and results for a significant amount of statistics.

content. This could then result in a wrong position of the first/last bin and, especially in the case of a limited number of bins, have a significant influence on the fit output. Now these underflow and overflow bins are excluded from the fit range and will have no influence on the final result.

The benefit of using this method is that it is able to save much more histograms than the *ROOT* class. It saves for each considered distribution, the *ProjectionY* distribution together with the double Gaussian fit for this bin.

Detailed information is stored in the following directories:

AnomalousCouplings/PrepareGenLevelRunning_Sep2014/TransferFunctions
m – machines directory?

STILL TO REVIEW

4.1 Creation of the Transfer Function

In this section the different steps which were performed in order to built and implement the Transfer Function (TF) will be discussed in detail. The TF's used in this analysis are assumed to be uncorrelated, as shortly discussed in the PhD thesis of Arnaud. This assumption is important since otherwise it allows to built them for each variable separately, as given in Equation 4.4. The correctness of this assumption can be checked by looking at E vs θ , E vs ϕ and θ vs ϕ histograms.

$$W(E, \theta, \phi) = W(E)W(\theta)W(\phi) \quad (4.4)$$

In this analysis it has been opted to use p_T -dependent TF in stead of the generally used E -dependent ones. This results in a large amount of adaptations of the MadWeight configuration files as will be briefly explained here. Since the TF configuration files in MadWeight allow the change of the considered kinematic variables it seemed more relevant to utilize the transverse momentum of the considered partons and jets in stead of the energy. This choice was especially motivated by the fact that the used *.lhco* file was constructed to contain the transverse momentum as input variable. As a consequence the TF configuration file **file** should be adapted to use the $pt(p)$ and $pt(pexp)$ variables in stead of $p(0)$ and $pexp(0)$.

Since MadWeight contains some hard-coded information about the kinematical information used in the calculation of the TF's, the use of p_T -dependent ones resulted in some difficulties. One important observation was the fact that as soon as the configuration files are adapted to be compatible with the p_T -dependent ones, there is no easy turning back to the original E -dependent TF's. This is not the desired behavior since it excludes the possibility of quickly testing any discrepancy between the created TF and the original ones. Hence it has been decided to include the relevant MadWeight directory on GitHub and develop two separate branches, one for each type of kinematic variable. This allows to easily switch between the TF's and conduct as much tests as desired. The corresponding branches on GitHub are **TF_EDependent** and **TF_PtDependent**.

Within these branch also all the different Event directories containing all executed tests are stored. This is used as a back-up since these results are only stored on localgrid where no back-up scheme is foreseen. The only disadvantage of this is that a clear overview of the performed changes to the configuration files is missing. **Give a short overview of what had to be changed!**

4.1.1 Used analysis files

The Transfer Functions are calculated using the simulated $t\bar{t}$ sample which will be used throughout the entire analysis. A very small nTuple is created from this simulated sample containing only the TLorentzVector information of both generated and reconstructed particles. From this the necessary diagrams, such as the 2D distributions of the p_T - , θ - and η -difference between the generated and reconstructed particle with respect to the generated value, are created and saved in the following ROOT file (located on the m-machines **or also copied locally??**):

AnomalousCouplings/TFInformation/PlotsForTransferFunctions_FromTree.root

The main analyzer, called *TFFit.cc*, performs the double Gaussian fit of these 2D histograms and afterwards the E -dependent calorimeter fit. The technicalities and specific details of these fit procedures are documented in the *TFCreation* class which can be found in the *PersonalClasses* directory.

The results of the two consecutive fits performed on the Y-projections of these 2D distributions are stored in a different ROOT file, together with the original 2D histograms. Also the function form of the double Gaussian fit formula using the obtained fit parameters, added in order to test the robustness of the fit results outside the fitted range, can be found in this ROOT file.

AnomalousCouplings/TFInformation/CreatedTFFromDistributions_FromTree.root

This analyzer also has the flexibility to perform the fit on the entire range or on pre-defined ranges set by the user. For this a separate function, called *SetFitRange*, is created where for each histogram the fit range for each separate bin can be defined. This is extremely useful to optimize the doubleGaussian fit which has to cover both the peak and the tail of the distributions in order to correctly calculate the 6 fit parameters.

Another useful aspect of this analyzer is the automatic creation of the necessary *.dat* Transfer Function files needed for implementation in MadWeight. This is done in the *WriteTF* class and the created files are³:

AnomalousCouplings/TFInformation/TF_user.dat

AnomalousCouplings/TFInformation/transfer_card_user.dat

This first file contains the functional form of both the E -dependent calorimeter fit and the functional form of how these 6 parameters should be included in the double Gaussian formula. Also the width for the different kinematic variables is defined within this file. For the moment the method used in the Transfer Functions already implemented in MadWeight is followed, implying that the width of the Transfer Function is defined as the maximum of the σ -parameter of the two Gaussians considered in the double Gaussian fit. The only difference is that instead of the generated kinematic information, which is the variable on the abscissa of the considered 2D histograms, the reconstructed one is used.

The second file contains the actual values of the different fit parameters for all the considered kinematic variables and particle types. Therefore this file is an extensive list of values to which is referred in the previous *TF_user.dat* file. For each particle type and kinematic variable the numbering used should be unique such that the correct values are implemented in the functional forms of the used fit formulas.

³Currently two different files are created, one for separate η bins and one for all of the events.

Separating narrow and wide gaussian

In order to differentiate between the narrow and wide gaussian both the amplitude and the σ -parameter should be compared. However the most important parameter is the latter one, σ , since this represents the width of the corresponding Gaussian distribution. Nevertheless it is expected that the distribution with the narrowest distribution also has the highest peak.

In order to easily compare the two distributions a stacked canvas is added to the ROOT file which shows both distributions for different $p_{T,gen}$ values together. The distinction between narrow and wide gaussian distribution is currently being made by the size of the σ variable. Hence the histogram with the narrowest distribution is plotted in red while the widest one is plotted in green. Such a canvas is made for each of the considered 2D-histograms. They should be analyzed in detail in order to understand the correctness of the double Gaussian fit applied for the creation of the Transfer Functions. For the moment there are still a couple of 2D-histograms which don't show the expected behavior. **Additional investigation of these stacked canvasses should be performed as soon as possible.**

Remark: Should check whether this splitting in narrow and wide gaussian is actually necessary for the MadWeight implementation. MadWeight only seems to need the general fit formula and doesn't need to know which of the two distributions is the narrow and which is the wide one.

Importance of start values

Since the double Gaussian fit really needs accurate information of both the peak and the tails, detailed review of the start values for each of the 6 fit parameters significantly improves the success rate of the fitting method. Hence special care should be awarded to ensure the correctness of these start values by comparing the fit distributions for the different particles. After quite a while it is possible to quickly see whether the fit distribution has the expected shape and whether the used start values can be considered as stable. The start values used for the different 2D histograms is given in Table 4.1.

4.1.2 Applied $|\eta|$ binning

Since the kinematic variables tend to depend on the pseudorapidity η the considered 2D histograms are created for four distinctive $|\eta|$ regions. It has been chosen to split the barrel region into three separate bins while the entire endcap region is contained within one single bin. The chosen binning is given in Table 4.2 together with the percentage of events present in each of the considered $|\eta|$ bins. This clearly shows the lower statistics available in the endcap region which results in larger difficulties of properly reconstructing the fit parameters in this region. This is shortly discussed below.

The analyzer mentioned above is developed in such a way that both the fit results for all events as the results for the four separate $|\eta|$ bins are stored together. Therefore all the results can always be compared in the created ROOT files and in the distinct *.dat* files.

One important difference between the 2D-distributions containing all events and the 2D-distributions specific for one of the $|\eta|$ bins is the number of bins used. Since the statistics is significantly lower for the $|\eta|$ specific histograms, the predefined bin number is lowered with 25%. This ensures a more stable tail for the distribution and still a correct

2D histogram	Used start value for fit parameter					
	First (narrow) gaussian			Second (wide) gaussian		
	Mean a_1	Sigma a_2	Amplitude a_3	Mean a_4	Sigma a_5	Amplitude a_6
b-jet $\Delta\phi$	0.0002	0.022	8000	0.0002	0.06	3000
b-jet Δp_T	10	-12	20000	13	10	-5000
b-jet $\Delta\theta$	0	0.013	6000	0	0.04	2000
light jet $\Delta\phi$	0	0.022	8000	0.0004	0.002	3000
light jet Δp_T	0	8	4000	0	12	4000
light jet $\Delta\theta$	0	-0.014	6000	0	-0.05	2000
electron $\Delta\phi$	0	0.0012	1500	0	0.006	600
electron Δp_T	0	0.9	1500	0	-2	600
electron $\Delta\theta$	0	0.0013	2500	0	0.007	600
muon $\Delta\phi$	0	0.0004	800	0	0.0026	600
muon $\frac{1}{\Delta p_T}$	0	0.0003	2000	0	0.0006	500
muon $\Delta\theta$	0	0.002	500	0	0.0004	500

Table 4.1: caption ... Need to make sure that the narrow and wide gaussian is always the same ... Otherwise are the start values not correct for the different eta-bins ...!!

	$ \eta \leq 0.375$	$0.375 < \eta \leq 0.75$	$0.75 < \eta \leq 1.45$	$1.45 < \eta \leq 2.5$
Relative # events	26.21 %	23.91 %	32.54 %	17.34 %

Table 4.2: Different $|\eta|$ bins used for the Transfer Function creation. It is important to note that the η -values used for this binning are the reconstructed ones since generated values could be higher than the 2.5 cut-value.

reconstruction of the peak. However for the last $|\eta|$ bin considered, the endcap part, a slightly different method is used. Since the statistics is much lower in this part of the detector the used range had to be slightly stretched in order to ensure a nice overview of the tails. This is necessary for the correctness of the double Gaussian fit. Therefore the range of the abscissa is enlarged on both sides with 20% and the used number of bins for this axis is identical to the one used for the overall 2D-distribution.

Coping with low statistics in last $|\eta|$ bin

Solution : Excluding bins! + combining bins

Explanations!!

4.1.3 Implementation in MadWeight – NEED TO UPDATE!

All the possible Transfer Functions which are implemented in MadWeight can be found in the *Source/MadWeight/transfer_function/data* directory. Any file can be added to this list and used within MadWeight.

The relevant files used for the creation of the Transfer Functions are given below. The first one is the translation of the used *TF_user.dat* into a MadWeight readable file which can be implemented. The second file is only relevant around line 292 where the function used for the Transfer Function creation is explained. This is the general MadWeight

constructor file where all the different MadWeight functions are defined.

*Source/MadWeight/transfer_function/transfer_function.f
bin/internal/madweight_interface.py*

What about call_tf.f file which has to be changed every time a new TF is initialized!

The implementation in MadWeight should be done in such a way that the value of the outermost bins is used for all the p_T values outside the fitted region. This is necessary since the extrapolation using the obtained fit parameters doesn't result in the desired double Gaussian behavior for these p_T values. For values outside the fitted region, an inverted double Gaussian distribution or a distribution with two distinct peaks occurs rather often. This can be seen in Figure 4.1

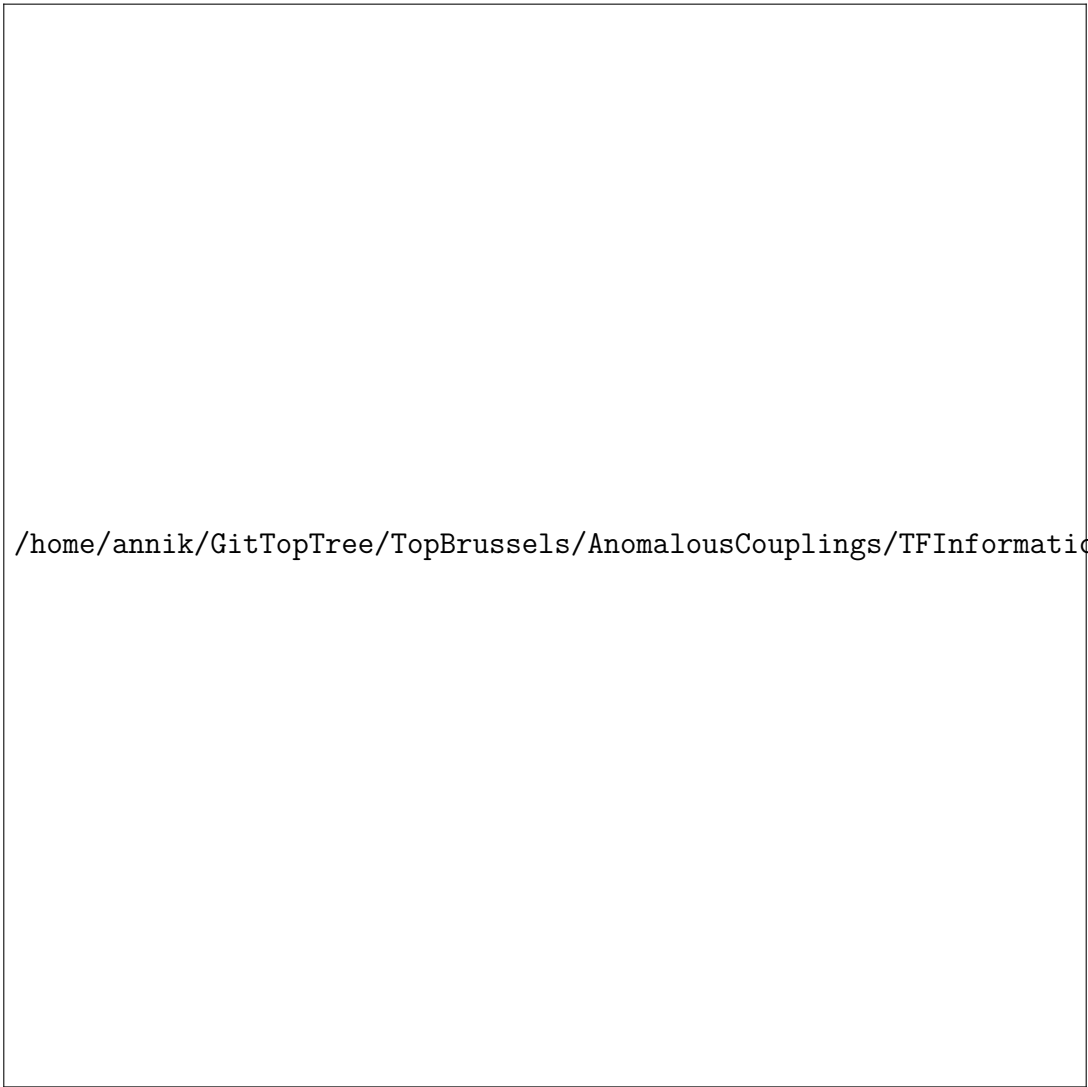


Figure 4.1: Extrapolation obtained using the fit parameters of the double Gaussian functional form. Values outside the fitted range show a distinctly different shape with respect to the ones actually fitted. *Maybe consider to lower the number of bins and make the titles more visible (Only p_T cut value is really important!)*

4.2 Obtained distributions

Each of the considered histograms is a 2D histogram where the abscissa represents the transverse momentum of the generator level parton and the ordinate the difference between the generator level parton and the reconstructed matched particle. This is done for the difference in transverse momentum and in θ and ϕ angles.

All the interesting histograms can be created automatically, for each of the desired $|\eta|$ bins separately, using the following ROOT analyzer:

```
AnomalousCouplings/TFInformation/FitDistributions/SaveFitHistograms.C
```

This analyzer is able to create each of the histograms separately, both as *.pdf* and *.png*⁴, and automatically saves all the histograms of one type in a large stacked canvas. This allows to quickly see the used 2D distributions for each of the particle types (b-jets, light jets, electrons and muons) and the three kinematic variables (p_T , η and ϕ). This stacked canvas is shown in Figure 4.2. Also the general behavior of each of the fitted diagrams together with the overall χ^2 distribution is created for each 2D histogram as can be seen from Figure 4.3, showing this for the p_T distribution of the b-jets. Finally the distribution of the 6 double Gaussian fit parameters together with the fit result of the E -dependent calorimeter formula is also collected in a stacked canvas, as can be seen in Figure 4.4. The 2D distributions for the difference in transverse momentum tend to show a slightly asymmetric behavior, as can be seen from Figure 4.2. This can be explained by the influence of the event selection, which has a difference effect on the generated particle than the reconstructed particle. This because a particle surviving the p_T cut actually has a different p_T value on generated level due to **bad resolution, detector effects** (???). This effect is almost negligible for the ϕ and θ angles (**Definitely sure that this is the case ??**).

4.3 Control checks for Transfer Functions

Compare results with normal (single) Gaussian

Still to do ...

Compare result with previous analyses

This will imply to put $p_{T,reco}$ information on the abscissa in stead of the current $p_{T,gen}$ one. Also it will result in a huge change of the start values which are however necessary to perform a successful double Gaussian fit.

Compare results with predefined ROOT class

Still to do ...

⁴.*png* files are less interesting since with the package *graphicx* *.pdf* figures can be included in *LaTeX*.

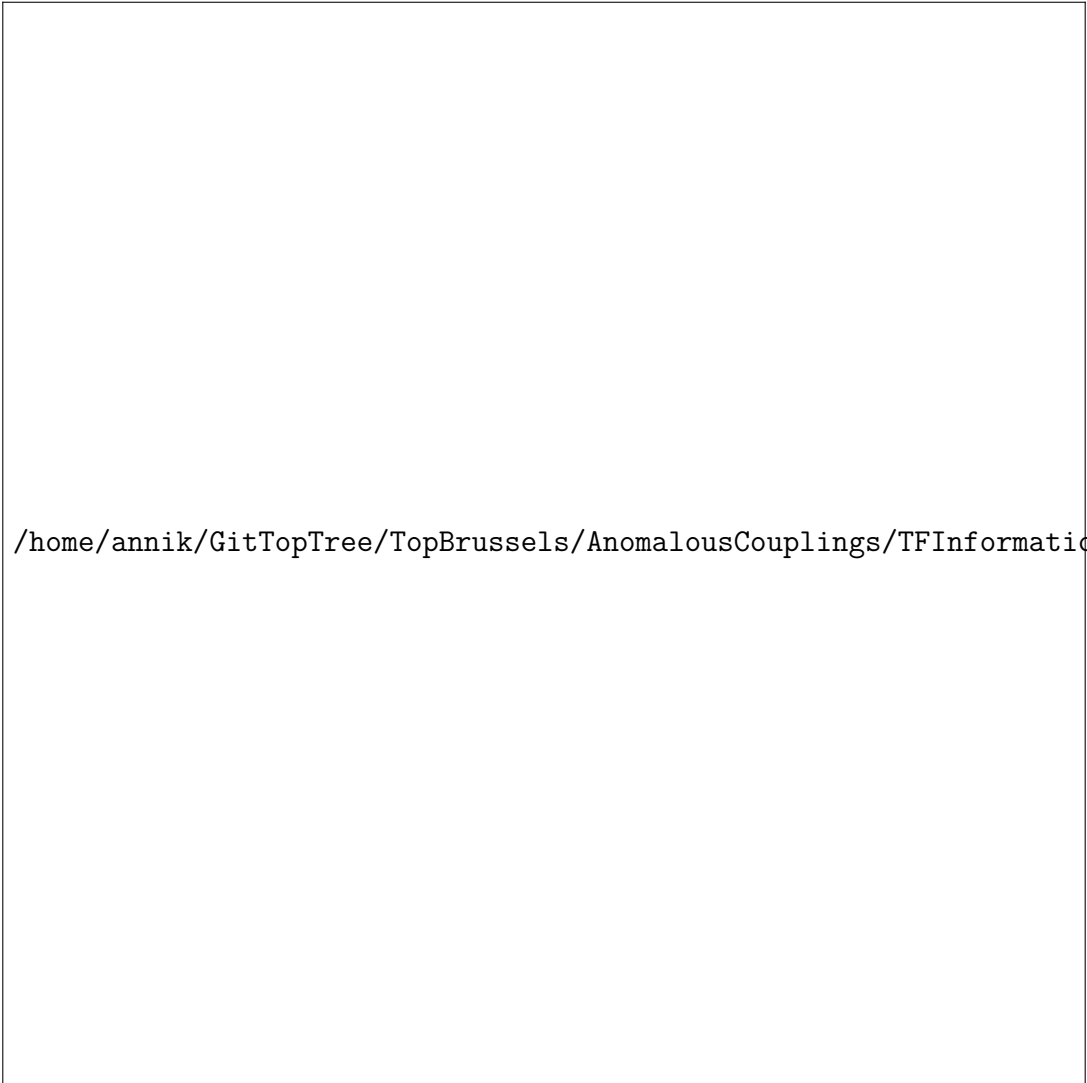


/home/annik/GitTopTree/TopBrussels/AnomalousCouplings/TFInformation/FitDistributi

Figure 4.2: Used 2D distributions for double Gaussian fit. **IMPROVE CAPTION!**

```
/home/annik/GitTopTree/TopBrussels/AnomalousCouplings/TFInformation/FitDistributi
```

Figure 4.3: Distribution of the energy difference between the generator level parton and the corresponding light quark jet for each of the 10 considered bins and the overflow bin. All distributions were fitted with a double Gaussian function.



/home/annik/GitTopTree/TopBrussels/AnomalousCouplings/TFInformation/FitDistributi

Figure 4.4: Energy dependency of the 6 parameters of the double Gaussian fit function. The result of the double Gaussian fit for each p_T bin is combined in a p_T dependent histogram and then fitted with the Calorimeter energy function as explained in the PhD Thesis of Arnaud Pin.

Chapter 5

Preliminary Results

5.1 Results on reconstructed level

5.2 Background influence

Chapter 6

Understanding MadWeight Results

6.1 Comparing the two used MadWeight versions

Since it was found that the latest MadWeight version (aMC@NLO) resulted in many events with weight equal to 0 it was decided to compare this version with the previous one (mc_perm). It is expected that both versions result in similar weights when identical events are considered, otherwise the used version of MadWeight would have a too large influence on the analysis result.

Therefore two events which could successfully run in the newest MadWeight version were also calculated using the old version. The obtained weights and their uncertainty can be compared in the following table and all the relevant information can be found in:

*/home/annik/Documents/Vub/PhD/ThesisSubjects/AnomalousCouplings
/CompareMWVersions_May2014*

Event Number	V_L value	aMC@NLO version		mc_perm version	
		Weight	Uncertainty	Weight	Uncertainty
1	1.5	9.7610^{-28}	4.0710^{-30}	1.4410^{-26}	4.1910^{-29}
	1.0	1.9210^{-28}	8.0410^{-31}	2.8410^{-27}	8.2810^{-30}
	0.5	1.2010^{-29}	5.0310^{-32}	1.7810^{-28}	5.1710^{-31}
2	1.5	1.8610^{-23}	1.1510^{-25}	1.7710^{-24}	1.2310^{-26}
	1.0	3.6510^{-24}	2.2510^{-26}	3.5710^{-25}	2.7510^{-27}
	0.5	2.2710^{-25}	1.4710^{-27}	2.2310^{-26}	1.7210^{-28}

Table 6.1: Weight obtained from MadWeight for two specific ttbar semi-muonic (+) events. For these events the V_R was fixed to its Standard Model expectation value, which is 0, while the V_L value was varied.

Comparing these values clearly shows that there is a significant difference between the two MadWeight versions which were considered in this analysis. With some effort a general difference of a facto 10 can be identified between the two versions, with a higher weight value for the older mc_perm MadWeight version.

However when showing the relative differences between the different weights it can be seen that the behavior of these two MadWeight versions is actually very similar. Therefore the histograms below give firstly the actual weight value and secondly the weight value normalised to the weight corresponding to the coupling parameter $V_L = 0$.

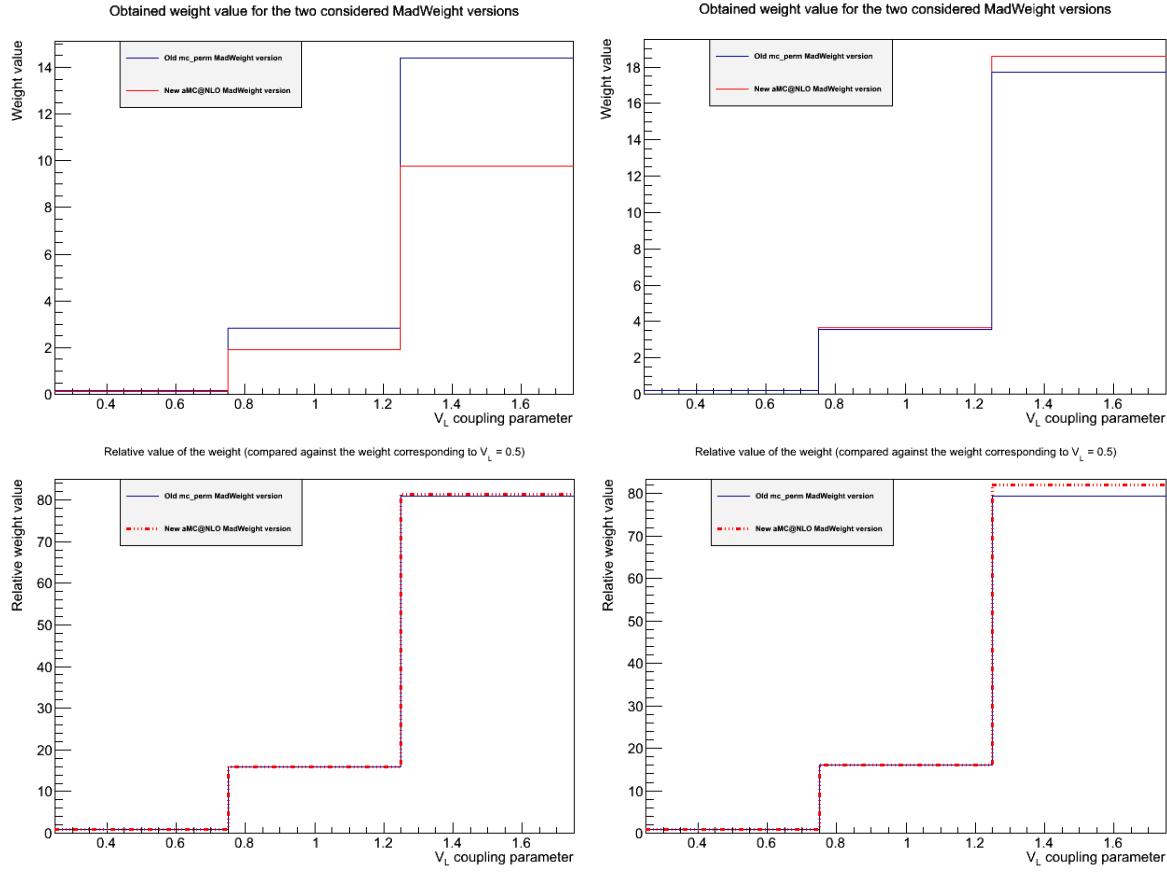


Figure 6.1: Distribution of the weights obtained from MadWeight for the two considered MadWeight versions (aMC@NLO and mc_perm) for two specific ttbar semi-muonic (+) events.

The above histograms clearly indicate that however the actual values of the weight significantly differ, the normalized results are almost identical.

This implies that the results obtained with MadWeight should always be normalized with respect to another MadWeight result (obtained using the same MadWeight version of course).

6.2 Individual weight distribution for considered gridpoints

The first Likelihood distribution for the considered gridpoints gave rise to an unexpected result. In order to understand whether this strange behavior can be explained by a couple of events with a bad weight, the individual weight distribution for a couple random events was studied. If these distributions indeed result in the correct behavior the events which influence the overall Likelihood distribution can be studied individually.

All the relevant information can be found in the following directory:

*/home/annik/Documents/Vub/PhD/ThesisSubjects/AnomalousCouplings/
UnderstandLikelihoodDistr_July2014*

And the creation of the MadWeight weights together with the python scripts making the corresponding histograms can be found in:

```
/localgrid/aolbrech/madweight/ttbarSemiMuPlus_QED2/Events
```

The relevant python scripts are the following:

- **CalculateLikelihood.py** which simultaneously creates the histograms for the XS distribution, the raw and normalized Likelihood distribution, and if required the individual weight distributions for the selected events. All these histograms are saved in the Histos.root file.
- **RemoveZeroWeightEvents.py** which removes the events with weight equal to zero from the list and saves the non-zero events in a new .out file. On the other hand the events which failed the MadWeight computation are saved on a new .lhco file together with one successful control event and are send again through MadWeight for a new weight calculation. **This should be updated since the new computation of MadWeight also results in weights equal to zero for these failing events. So should be investigated what is different about these events ...**

The first three histograms show the obtained Likelihood distribution for the different gridpoints which were considered. From these can be concluded that the behavior of the Likelihood normalized with the corresponding cross section divided by the Standard Model cross section is dominated by the distribution of the normalized cross section values. This means that any small deviations of the raw Likelihood values gets washed out by the multiplication with the normalized cross section values.

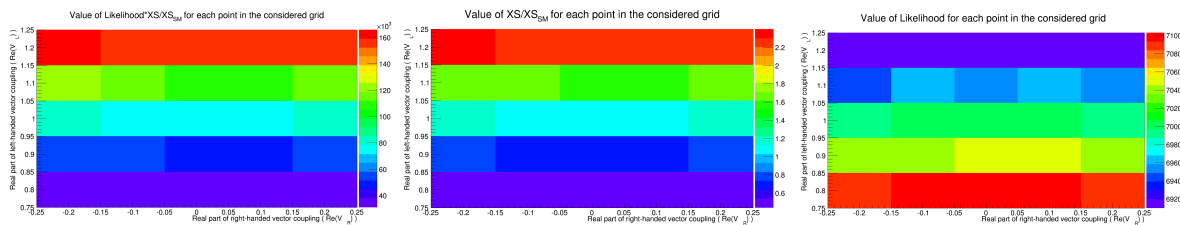


Figure 6.2: ...

The individual weight distribution for some random events can be found here.

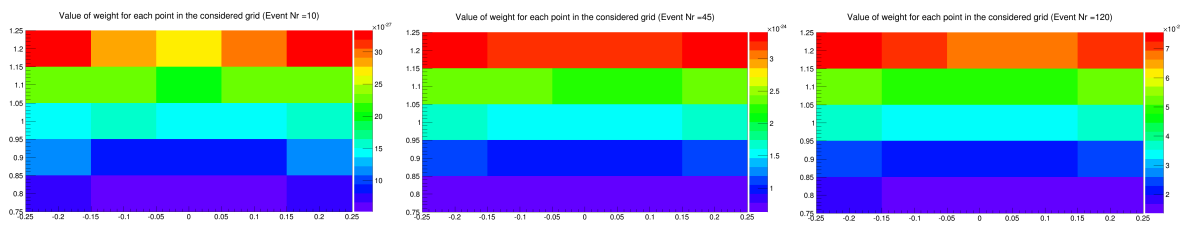


Figure 6.3: ...Script should be ran again, and names for the axis should be added for these individual weight histograms!

Chapter 7

Analyzing FeynRules model

7.1 Normalized coupling parameters

In order to investigate the actual influence of the value of the coupling parameters on the kinematics of the event, the considered coupling parameters should be normalized to unitarity before any hard conclusions can be made. Therefore the configurations which should be investigated in large detail are the ones for which the width of the decay remains unchanged. This is explained in detail in one of the previous sections (?? on page ??).

7.2 Understanding parameters larger than 1

Before starting to look at the ttbar Monte Carlo and reweighting the events with MadWeight, the created model in FeynRules should be completely understood. Special care goes out to the behavior of the kinematic distributions for values of the coupling parameters larger than 1. Since the Standard Model expectation puts the real part of the left-handed vector coupling V_L almost equal to 1, simulation should be available around this Standard Model expectation value. Therefore the created model should be able to cope with coupling parameters larger than 1.

For this reason .lhco files were generated with MadGraph with the following configuration, as mentioned in 2.4.2:

$$\begin{aligned} Re(V_L) &\in [0.7, 1.3] \\ Re(V_R) &\in [-0.3, 0.3] \end{aligned}$$

For these generated events the main kinematic distributions have been investigated. No clear difference between the behavior below and above 1 has been found.

7.2.1 Performed checks

7.2.1.1 Cross section change

RVR RVL	-0.30	-0.20	-0.10	0.00	0.10	0.20	0.30
0.70	0.3775	0.3120	0.2724	0.3275	0.2632	0.2910	0.3436
0.80	0.5964	0.5097	0.4595	0.4385	0.4444	0.4816	0.5471
0.90	0.9011	0.7950	0.7308	0.7026	0.7103	0.3229	0.8356
1.00	1.3187	1.1874	1.1085	1.0711	1.0823	1.1317	1.2263
1.10	1.8700	1.7116	1.6154	1.5669	1.5763	1.6335	1.7522
1.20	2.5858	2.3996	2.2789	2.2200	2.2263	2.2983	2.4322
1.30	3.4896	3.2711	3.1278	3.0626	3.0655	3.1506	3.2983

Table 7.1: Cross sections for the different RVR-RVL couplings normalized to the SemiElMinus Standard Model Cross section (8.261 pb)

From this table can be seen that the cross section increases when the real component of V_L gets larger. The value of the right-handed vector coupling has only a minor influence on the cross section.

7.2.1.2 Relative increase visible in XS, but not in kinematic distributions

Since the observed model cannot represent physics at values larger than 1, one option is to look at specific fixed values of the real part of the left-handed and right-handed vector couplings. A proportional change in both of these coupling parameters should change the cross section values, but the kinematic should remain unchanged. Therefore the following configurations will be investigated:

$$\begin{aligned} Re(V_L) &= 0.5 \quad \& \quad Re(V_R) = 0.5 \rightarrow 2.07115 \text{ pb} \\ Re(V_L) &= 1.0 \quad \& \quad Re(V_R) = 1.0 \rightarrow 33.1479 \text{ pb} \\ Re(V_L) &= 2.0 \quad \& \quad Re(V_R) = 2.0 \rightarrow 530.027 \text{ pb} \end{aligned}$$

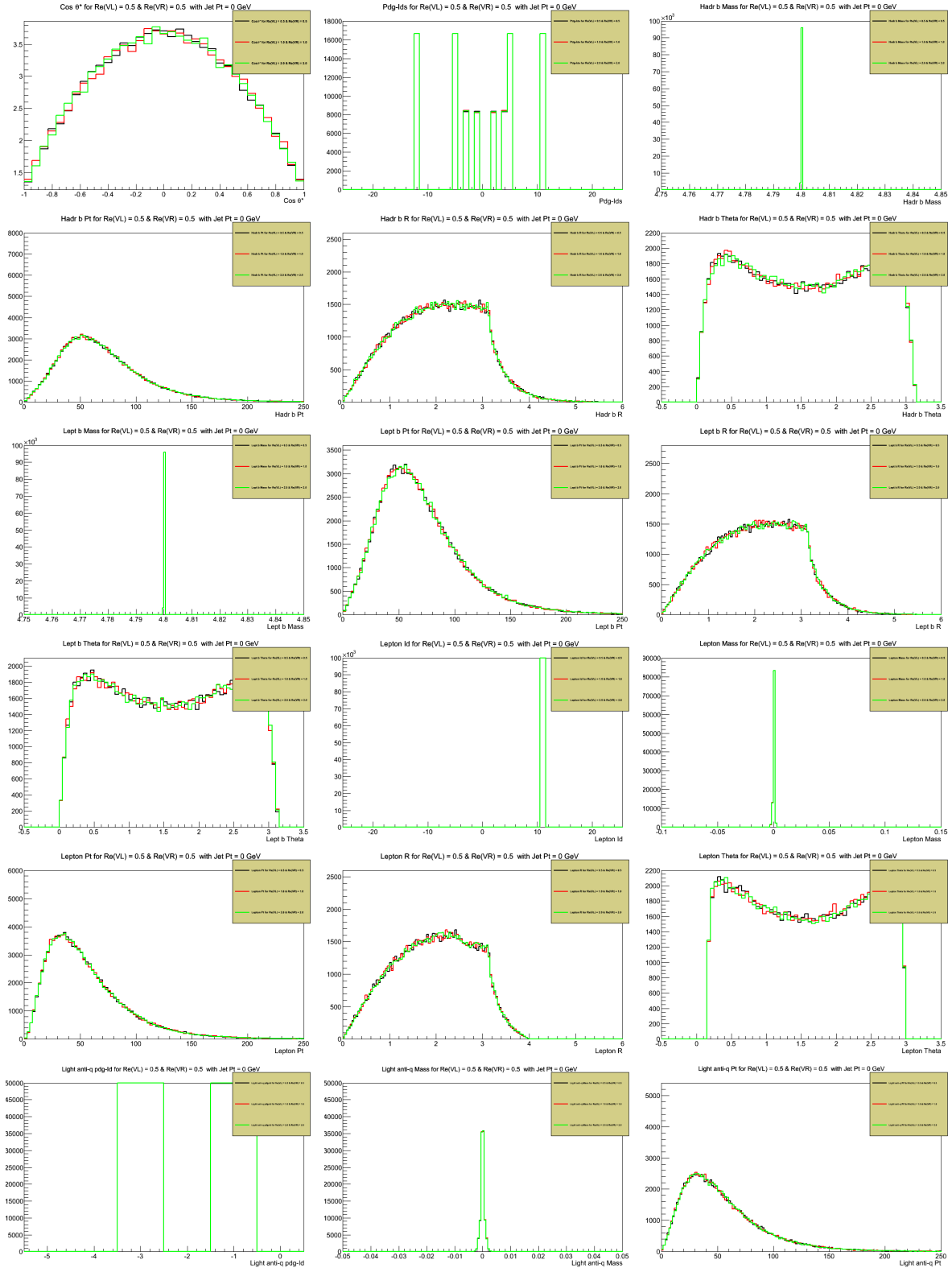
From the above numbers is clear that the Cross section becomes very large when the two coupling parameters increase. This can be understood quite easily since the second option allows much more decay options since the top quarks can decay both through the left-handed and the right-handed vector coupling side of the interaction vertex. The width of this configuration is not equal to the width of the Standard Model expectation and hence does not correspond to an actual physical solution. It is merely seen as a test of the model since the kinematics of the interaction should not differ.

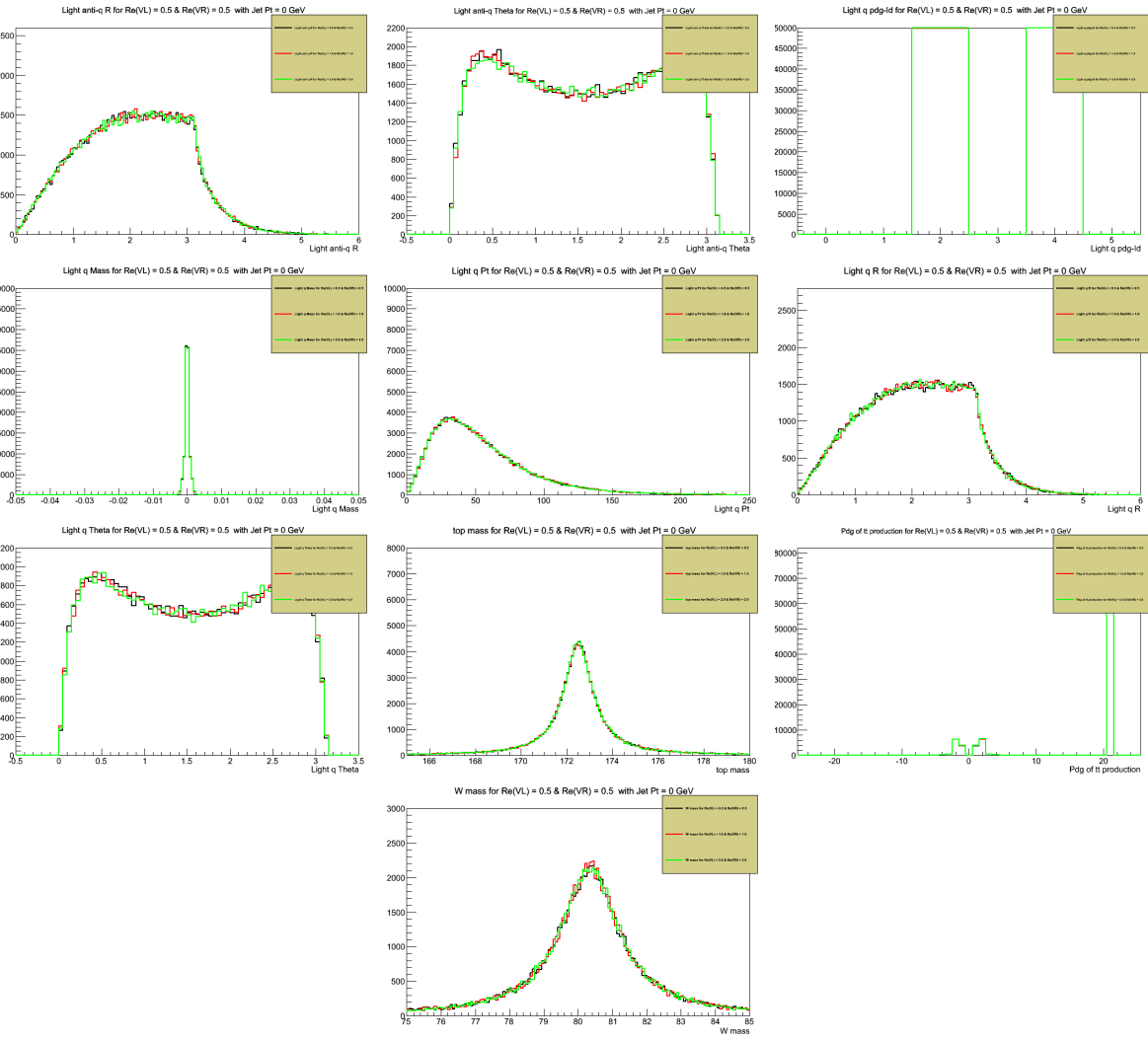
Looking at these plots clearly indicates that the kinematics doesn't change at all. Hence the created FeynRules model is able to deal in a correct way with these coupling parameters larger than 1.

These MadGraph files have been created and can be found in:

```
/user/aolbrech/AnomalousCouplings/MadGraph_v155/MassiveLeptons/
MadGraph5_v1_5_5/Wtb_ttbarSemiElMinus/RelativeChange
```

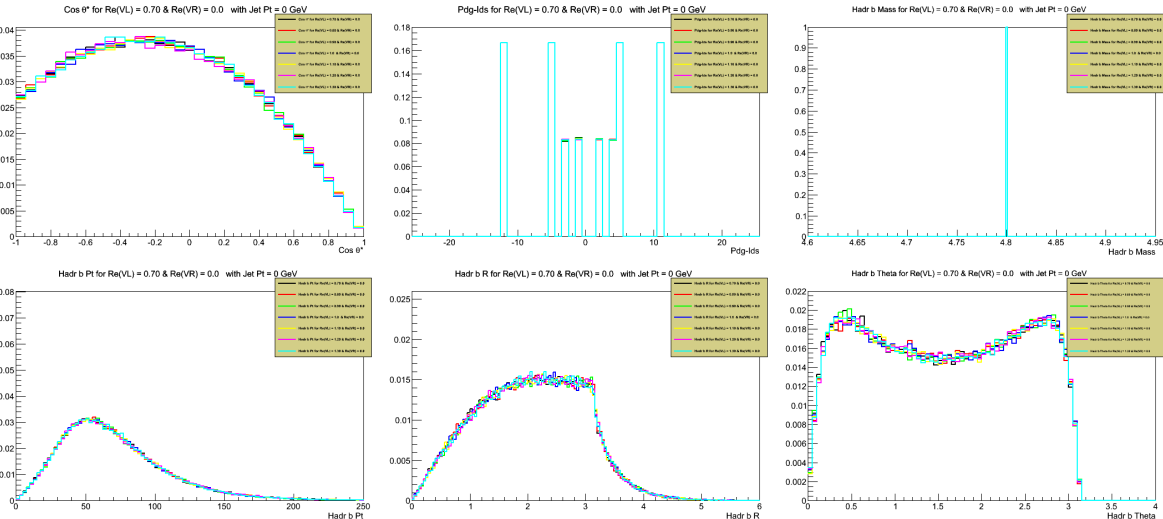
The distributions shown in this subsection are for fixed Jet Pt Cut value, set to 0. Also no Pt cut on the lepton was applied. Both coupling parameters have been changed proportionally.

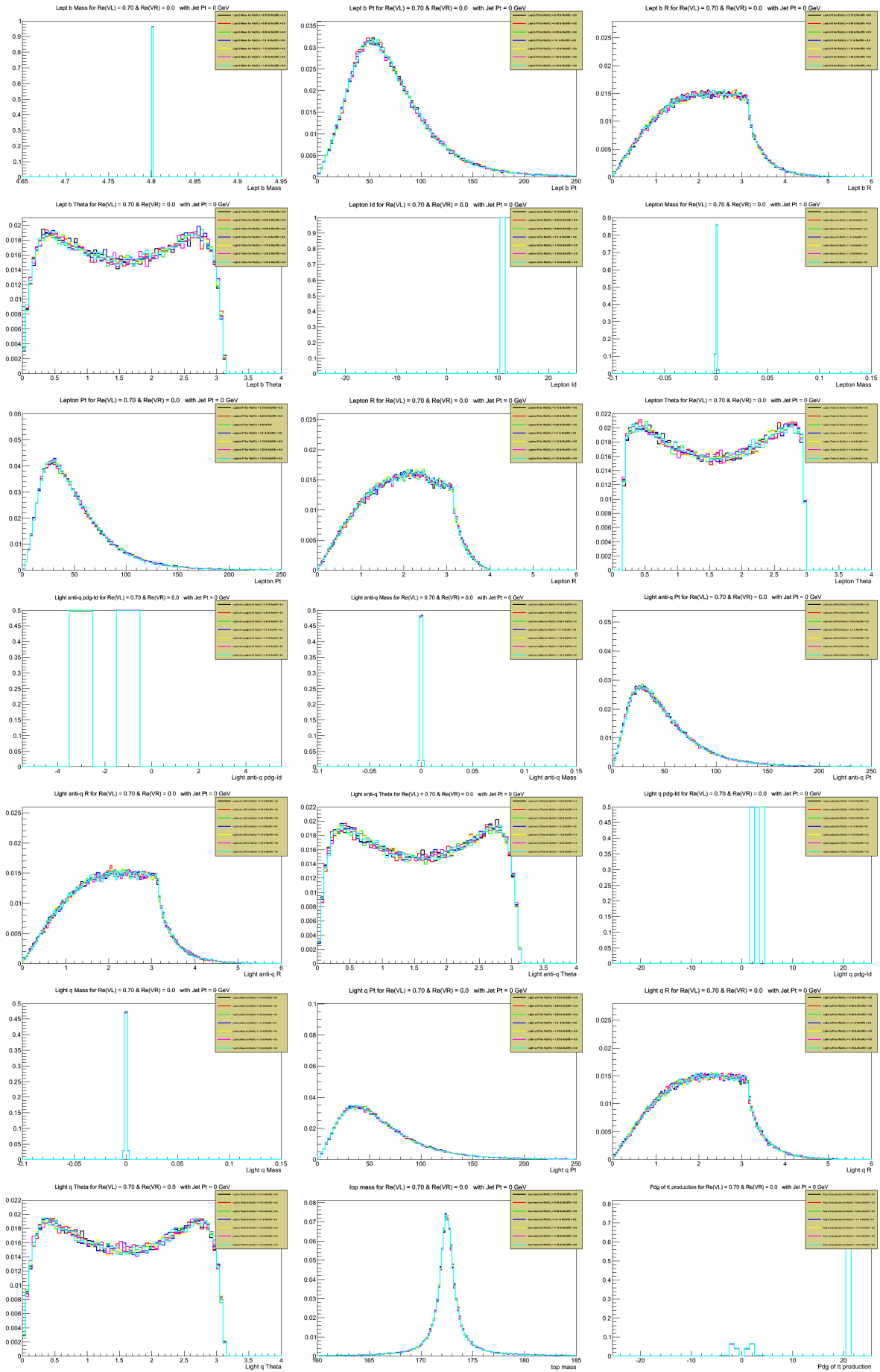


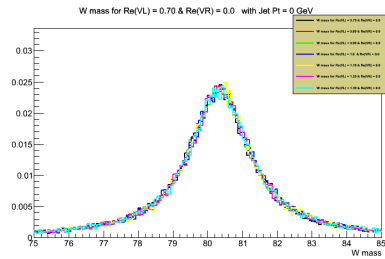


7.2.1.3 Model plots for fixed Pt Cut

The distributions shown in this subsection are for fixed Jet Pt Cut value, set to 0. Also no Pt cut on the lepton was applied. In this case the real part of the left-handed vector coupling has been varied between 0.7 and 1.3 in steps of 0.1 while the right-handed parameter has been fixed to its Standard Model value (0.0).







7.2.1.4 Model plots for varying Pt Cut

Script adapted, but error obtained when running the python script ...

Worked when everything was copied to the TestDir ...

Maybe the use of nohup gives the problem ...

Chapter 8

MadGraph/MadWeight issues

8.1 Discussion with Olivier Mattelaer (8-9/01/2015)

During this discussion moment with Olivier Mattelaer many interesting subjects have been discussed, the most important of them are summarized below. A detailed overview with all suggestions and recommendations is also created, but not all of them have been added in this document. Many of these items ended up in the to-do list added further in the section.

8.1.1 Transfer Functions

The suggested way to investigate the influence of the created Transfer Functions is by first running the sample with a pure delta function for parton-level events. Afterwards the kinematics of the parton-level events of this sample should be smeared with the created Transfer Functions and then the sample should be ran again, this time with the new Transfer Functions. This ensures that in both cases the Transfer Function which is applied corresponds to the kinematics of the considered events. Any difference between the two results indicates a bias introduced by the Transfer Function.

An important remark was the missing normalisation of the double Gaussian Transfer Function. Currently the necessary normalisation factors have not been added and should be done as soon as possible. This because a non-normalized Transfer Function could result in wrong weights and introduce a significant bias to the obtained results.

A final important comment about the correct implementation of personal Transfer Functions is the behaviour outside the considered fit range. The strange distributions obtained for p_T values outside the considered fit range did not appear in the results of Olivier (and Arnaud) because they had a different fitting algorithm which explicitly forced the Minuit fitter to search only for a local minimum where the relative normalisation of both Gaussians was positive¹.

Since probabilities should always remain positive, the negative distributions should be excluded from the allowed options. This can be done by either adapting the used fitting algorithm to only consider positive probabilities or by simply changing the fit formula to use $\max(0, a_3)$ in stead of a_3 . The second solution is the most straightforward to

¹This is actually an allowed and physically motivated restriction which can be applied since it simply corresponds to requiring a probability to always stay positive.

implement, but has as disadvantage that any event with very high or low p_T will have weight 0 and hence be thrown away.

8.1.2 Likelihood normalization

The correct formula for the $\ln(\mathcal{L})$ is given in Equation (8.1):

$$-\sum_i^N \ln\left(\frac{1}{\sigma Acc} weight_{MW}\right) = N \ln \sigma + N \ln Acc - \sum_i^N \ln weight_{MW} \quad (8.1)$$

The above given normalisation formula has already been applied successfully on 1D-variation of the V_R parameter while keeping the V_L value fixed to its Standard Model expectation value. However similar success has not been obtained for the variation of the V_L component. It is currently been investigated whether this is caused by considering a too restricted grid or whether it is caused by a lack of sensitivity of the V_L variable. Both possibilities are likely because the observed variation between the different V_L configurations is comparable to the uncertainty introduced by the XS normalisation part in the formula.

This directly points the largest danger of using such a normalisation based on the XS of the considered configuration, namely the strong dependence on the uncertainty of the calculated cross section. This is illustrated in Equation (8.2):

$$unc \sim N \frac{\Delta \sigma}{\sigma} + \sum \frac{\Delta weight_{MW}}{weight_{MW}} \quad (8.2)$$

The first term in this Equation scales as N while the second term only scales as \sqrt{N} meaning that the first term quickly starts to dominate the total uncertainty. Therefore it is important to calculate these MadGraph cross sections for a large number of events in order to reduce the uncertainty as much as possible. The size of the relative uncertainty is also closely related to the number of events which will be calculated by MadWeight and hence a good balance should be found².

8.1.3 Cluster optimization

When discussing with Olivier about the restrictions of the IIHE cluster he mentioned the possibility to set a maximum number of jobs which can be submitted simultaneously to the cluster. This means that this maximum can be set to 2000 in order to be in agreement with the maximum number of allowed jobs at the IIHE cluster. There exists even the option to explicitly set the number of remaining jobs which should be reached before a new bunch of jobs should be submitted. Hence this allows to wait until the number of jobs running is reduced to about 1500 before a new set of jobs is submitted in order to reach again the maximum number of 2000.

This can all be changed in the *cluster.py* file which has a class “PBSCluster” at about line 1016.

²Important to note is that the N in the uncertainty formula should not be the same as the number of events used to calculate the MadGraph cross section. This N variable is really the number of events which are submitted to MadWeight in order to calculate the corresponding weight for each specific configuration.

The huge benefit of the above mentioned cluster optimization is that it allows to keep using the “collect” option of MadWeight without the necessity of combining multiple separate runs of each 2000 jobs. Hence one should just wait until all the events have been submitted and run the final collect step of the MadWeight setup.

8.1.4 Optimizations and bug fix

During this two-day discussion moment a couple of small optimizations of the used MadWeight configuration have been discovered.

At first it was clear that the used MadWeight version was considered to be an old version for Olivier. Since rather recently a stable version is kept with multiple updates and necessary bug-fixes. The installation command for this newer version is the following and is currently installed as a new directory *NewestMW_amcnlo* on */localgrid*.

```
bzr branch lp:mg5amcnlo
```

Secondly the issue of negative weights when using a δ Transfer Function was resolved. This was caused by a discrepancy between the integral implemented in MadWeight and the one developed by Olivier. The reason for a second integral is in order to deal with multiple Transfer Functions during one single submission. The bug-fix was directly created by Olivier and is currently implemented in all directories on */localgrid*.

A final but rather important remark was the fact that the developed model allowed CKM suppressed W-boson decays. This did not influence the final result since the probability for such decays was extremely small but significantly enlarged the CPU time since MadWeight considers each possible decay and does the calculation of the probability for all of them. Hence excluding these types of decays should improve the CPU running time with possibly a factor 4.

The restrictions on the model can easily be added in MadGraph as explained in the launchpad FAQ, and are currently implemented in the newest */localgrid* directory.

Chapter 9

Event Selection

9.1 Choice of b-tag requirements

9.1.1 Signal vs background comparison

Since the complete event should be reconstructed as accurately as possible the 'signal' is represented by the case that all four particles are matched correctly while the 'background' events are the events for which at least one particle is matched wrongly. Events which are not matched using the JetPartonMatching algorithm (currently ptOrderedMinDist with dR of 0.3 is used) are not included in either of these two variables and are shown separately in the tables found below.

First the different b-tag options are compared for the four possible combinations which are still allowed, namely the interchange of both the two light quarks and the two b-jets.

Option (no $\chi^2 m_{lb}$)	all 4 correct	≥ 1 wrong	$\frac{s}{\sqrt{b}}$	$\frac{s}{b}$	non-matched
2 L b-tags,	55967	50416	249.257	1.1101	225217
2 M b-tags,	49983	32012	279.361	1.56138	146633
2 M b-tags, light L-veto	39661	27751	238.081	1.42917	118389
2 T b-tags,	31444	16061	248.114	1.95779	78062
2 T b-tags, light M-veto	29160	15585	233.579	1.87103	73570
2 T b-tags, light L-veto	23159	14093	195.082	1.6433	59997

Table 9.1: Overview of correct and wrong reconstructed events for the different b-tags without the use of a $\chi^2 m_{lb} - m_{qqb}$ method

Option (no $\chi^2 m_{lb}$)	2 b's good	≥ 1 b wrong	$\frac{s}{\sqrt{b}}$	$\frac{s}{b}$	non-matched
2 L b-tags,	78896	27487	475.873	2.8703	225217
2 M b-tags,	70073	11922	641.765	5.87762	146633
2 M b-tags, light L-veto	58778	8634	632.57	6.80774	118389
2 T b-tags,	43804	3701	720.036	11.8357	78062
2 T b-tags, light M-veto	41617	3128	744.11	13.3047	73570
2 T b-tags, light L-veto	34908	2344	721.018	14.8925	59997

Table 9.2: Overview of correct and wrong reconstructed b-jets for the different b-tags without the use of a $\chi^2 m_{lb} - m_{qqb}$ method

Option (no $\chi^2 m_{lb}$)	2 light good	≥ 1 light wrong	$\frac{s}{\sqrt{b}}$	$\frac{s}{b}$	non-matched
2 L b-tags,	58707	47676	268.869	1.23137	225217
2 M b-tags,	50676	31319	286.351	1.61806	146633
2 M b-tags, light L-veto	40361	27051	245.398	1.49203	118389
2 T b-tags,	31690	15815	251.993	2.00379	78062
2 T b-tags, light M-veto	29466	15279	238.382	1.92853	73570
2 T b-tags, light L-veto	23456	13796	199.7	1.7002	59997

Table 9.3: Overview of correct and wrong reconstructed light jets for the different b-tags without the use of a $\chi^2 m_{lb} - m_{qqb}$ method

Above tables show a clear improvement for the 2 Tight b-tag case since suddenly the $\frac{s}{b}$ value goes up to almost 2. An additional benefit of the 2 Tight bt-tag case is that it as well will take care of a large part of the process backgrounds. Hence the motivation for selecting this b-tag option.

Comparing the normal 2 Tight b-tag case, where the light jets are defined as not being Tight b-tagged jets, against the two possibilities using a light-jet veto indicates no motivation to go for the light-veto option.

However the second table, showing only the reconstruction efficiency of the b-jets, shows an improvement when using a light-jet veto.

This means that, even if the number of selected events gets lower, the percentage of correct events does improve when asking for a light-jet veto since it ensures that mistagged b-jet events doesn't by mistake get identified as light jets. So events with a b-jet with a too low CSV discriminant now don't get selected anymore because these so-called light-jets don't survive the veto cut.

But, as confirmed by the last table, the efficiency of the light-jet reconstruction shows no distinct improvement. So for some reason the light-jets which are chosen with this veto method are not by definition the actual light-jets.

9.2 Use of $m_{lb} \chi^2$ method for selecting the correct b-jets

Option (with $\chi^2 m_{lb}$)	all 4 correct	≥ 1 wrong	$\frac{s}{\sqrt{b}}$	$\frac{s}{b}$	non-matched
2 L b-tags,	51055	55328	217.053	0.92277	514406
2 M b-tags,	45664	36331	239.572	1.25689	538794
2 M b-tags, light L-veto	36271	31141	205.539	1.16473	553377
2 T b-tags,	28580	18925	207.752	1.51017	573284
2 T b-tags, light M-veto	26513	18232	196.355	1.4542	576044
2 T b-tags, light L-veto	21073	16179	165.673	1.30249	583537

Table 9.4: Overview of correct and wrong reconstructed events for the different b-tags when a $\chi^2 m_{lb} - m_{qqb}$ method is applied

The two tables in this subsection require a different interpretation. The first one is actually a combined test of the $\chi^2 m_{lb} - m_{qqb}$ method and the optimal b-tag choice while

Option (with $\chi^2 m_{lb}$)	Correct b's	Wrong b's	$\frac{s}{\sqrt{b}}$	$\frac{s}{b}$	Correct option exists
2 L b-tags,	66882	12014	610.19	5.56701	78896
2 M b-tags,	59520	10553	579.395	5.6401	70073
2 M b-tags, light L-veto	49556	9222	516.04	5.37367	58778
2 T b-tags,	37013	6791	449.146	5.4503	43804
2 T b-tags, light M-veto	35015	6602	430.94	5.3037	41617
2 T b-tags, light L-veto	29139	5769	383.64	5.05096	34908

Table 9.5: Overview of the number of times the correct b-jet combination is chosen when using a $\chi^2 m_{lb} - m_{qqb}$ method

the second one is merely a performance check of the mlb method.

This second table had to be added since the first table can't be directly compared against the tables in the previous subsection since currently only one b-jet combination is left while in the previous case an iteration between the different b-jets was allowed. So the numbers will be lower by definition when the $\chi^2 m_{lb} - m_{qqb}$ method is applied.

Therefore the second table is relevant in order to select whether some clear gain can be obtained when applying this method since it represents the number of times the correct b-jet combination. If this percentage is higher than 50%, which is the case, an improvement is obtained compared to an iteration between the two possible combinations.

The first table indicates again that no real difference is found between the different b-tag options, but that as soon as 2 Tight b-tags are applied the $\frac{s}{b}$ improves slightly. Also the second table shows no difference in efficiency between the different b-tag options, but shows however that the use of this $\chi^2 m_{lb} - m_{qqb}$ method significantly enhances the correct choice of the b-jet combination. In about 84% of the cases the correct b-jet combination is chosen.

9.3 Histograms for event selection choice

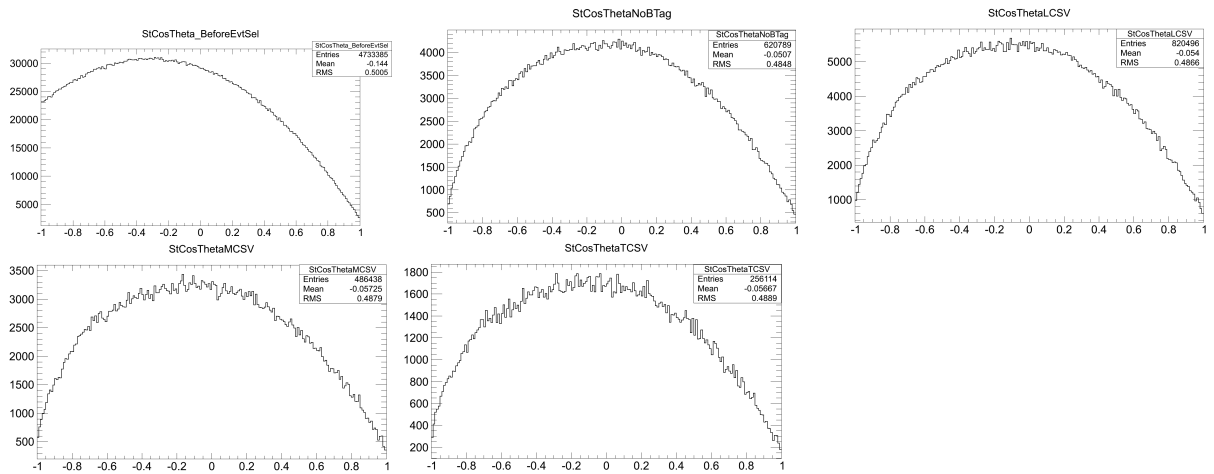


Figure 9.1: The $\cos \theta^*$ distribution for the different b-tag options (all of them imply double b-tag), which are not really influenced by the application of a b-tag. The only relevant distortion is caused by the event selection which is applied.

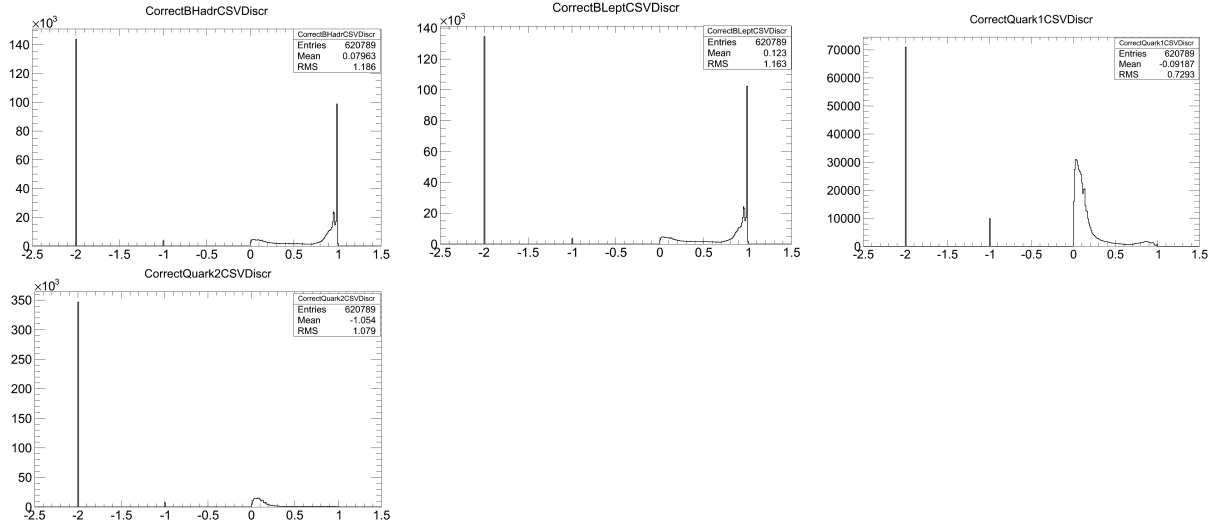


Figure 9.2: Distribution of the CSV discriminant for the different correctly matched quark-jet pairs. The value -2 is used to represent a non-matched jet. As expected the b-jets have a large peak at 1 , so the Tight b-tag of 0.898 will not take away too many correct b-jets. The problem in the matching is clearly represented in distribution of the second quark which is only reconstructed in less than half of the cases.

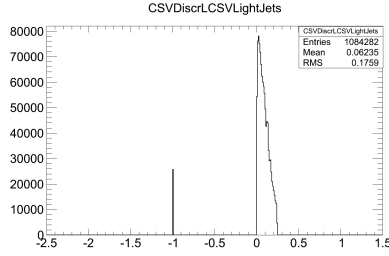


Figure 9.3: Distribution of the CSV discriminant of the selected light jets (all of them). Add same histograms for Medium and Tight option, this will show how many of the light jets actually have a large CSV discriminant (maybe only focus on the two/three leading light jets)

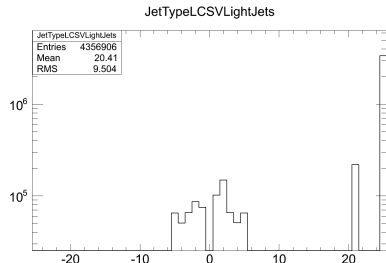


Figure 9.4: Jet type of the of the light jets (all of them). The value 25 means that the found light jet couldn't be matched to a Parton with the JetPartonMatching method. Same for M and T ... ?

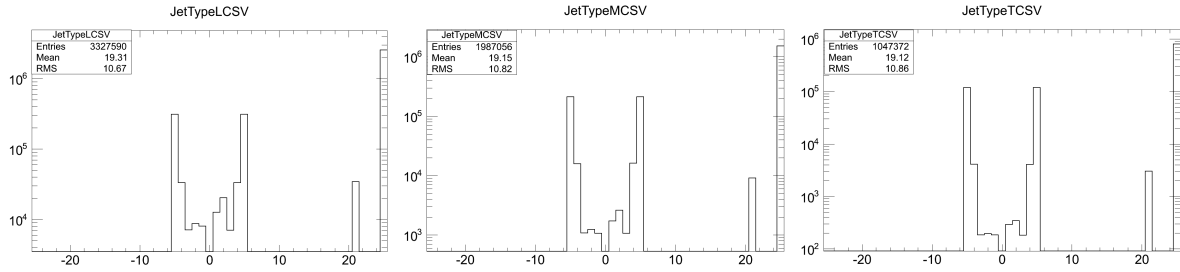


Figure 9.5: Jet type of the b-tagged jets (all of them) with the same convention for the non-matched jets.

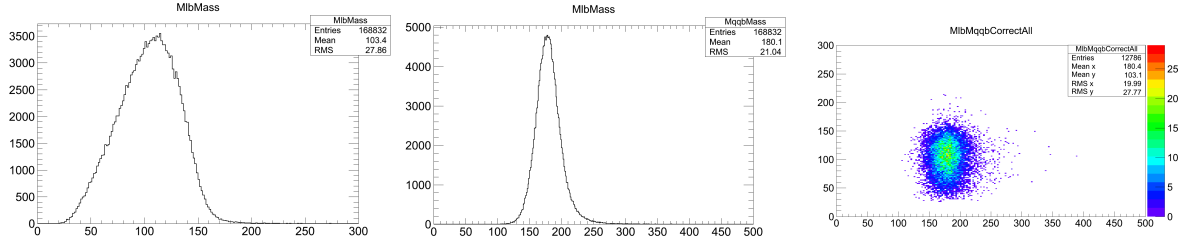


Figure 9.6: The first two histograms show the mass distribution for the correctly matched and reconstructed particles. A gaussian fit is applied in order to obtain both the m_{lb} and m_{qqb} mass and sigma. The last histogram shows the 2D behavior of these distributions.

9.4 Considering 2 or 3 light jets

In order to try to improve the signal efficiency it can be considered to add a third light jet to the particles which have to be taken into account for the jet selection. Adding this third jet will however result in 4 additional combinations which have to be considered so this method will only benefit when the χ^2 m_{lb} - m_{qqb} method is applied. Since MadWeight uses so much CPU sending the 6 possible combinations to MadWeight will not be beneficial.

9.4.1 Event selection numbers comparison

Option (no $\chi^2 m_{lb}$)	chosen jets are correct (%)	$\frac{s}{b}$	3rd jet is correct (%)
5 jet case, 2 T b-tags	76.2852	3.21677	70.244
4 jet case, 2 T b-tags	66.9091	2.02198	X

Table 9.6: Overview of correct and wrong reconstructed events for the different b-tags without the use of a $\chi^2 m_{lb}$ - m_{qqb} method

Option (no $\chi^2 m_{lb}$)	2 b's chosen correctly (%)	$\frac{s}{b}$	3rd jet is correct (%)
5 jet case, 2 T b-tags	90.5014	9.52784	64.5863
4 jet case, 2 T b-tags	92.3745	12.1138	X

Table 9.7: Overview of correct and wrong reconstructed b-jets for the different b-tags without the use of a $\chi^2 m_{lb}$ - m_{qqb} method

Option (no $\chi^2 m_{lb}$)	chosen light jets are correct (%)	$\frac{s}{b}$	3rd jet is correct (%)
5 jet case, 2 T b-tags	79.2892	3.8284	70.2241
4 jet case, 2 T b-tags	67.4722	2.0743	X

Table 9.8: Overview of correct and wrong reconstructed light jets for the different b-tags without the use of a $\chi^2 m_{lb} - m_{qqb}$ method

These three tables look at either a pure 5 jet case or a pure 4 jet case and comparing the numbers in each table with eachother is probably not extremely relevant. This because in the pure 5 jets case the matching requirement is loosened to two out of the three chosen light jets correctly matching with the partons. So in 1 out of 3 possibilities the so-called correct event will not be correct resulting in too high numbers for this case.

The first column gives the percentage how often the chosen jets are indeed the correct partons, hence in the 5-jet case the number of times the 5 possible jets match with the 4 correct partons. In the 4-jet case it implies that the four chosen jets are matched correctly with the 4 partons. The second column gives a similar value since the signal is defined as the number of times the matching was done correctly for the four partons while the background stands for the events where one of the matching is not succesful. The third column checks how often the third jet is one of the two correct light jets and compares it against the number in the first column. So it represents the number of times adding the third jet results in an improvement of the event reconstruction.

The numbers which are relevant in these tables are exactly these two last columns. These numbers show that in about 70% of the cases the third jet is actually one of the correct quarks. Therefore it can be decided from these numbers that in quite a lot of events, an improvement can be obtained when this third light jet is considered as well.

9.4.2 Mlb-algorithm numbers comparison

Option (with $\chi^2 m_{lb}$)	4 chosen jets are correct (%)	$\frac{s}{b}$	3rd jet is one of the 2 correct light jets (%)	3rd jet is chosen and correct (%)
5 jet case, 2 T b-tags	73.2413	2.73711	21.3059	89.2513
4 jet case, 2 T b-tags	76.9258	3.33384	0	-nan
Pure 5 jet case, 2 T b-tags	65.6683	1.91276	74.3984	89.2513

Table 9.9: Overview of correct and wrong reconstructed events for the different b-tags when a $\chi^2 m_{lb} - m_{qqb}$ method is applied

Option (with $\chi^2 m_{lb}$)	% b's correct	$\frac{s}{b}$		
5 jet case, 2 T b-tags	90.3229	9.33364	0	0
4 jet case, 2 T b-tags	90.7656	9.82911	0	0
Pure 5 jet case, 2 T b-tags	89.9057	8.90659	0	0

Table 9.10: Overview of the number of times the correct b-jet combination is chosen when using a $\chi^2 m_{lb} - m_{qqb}$ method

When the m_{lb} method is applied, the two first columns in the given tables represent similar quantities with the only difference that now the 4 jets which are actually chosen by the χ^2 m_{lb} - m_{qqb} method are considered. In this case the third column represents the number of times the third jet is chosen when the two light jets are matched correctly, implying that the third jet is one of the correct ones and that the second light jet is also correctly matched. The final column only looks at the third jet and puts no requirement on the matching of the second light jet. So it compares the number of times one of the chosen jets is the third jet and in how many cases this chosen third jet is one of the correct partons.

9.4.3 Compare efficiencies for 3rd jet with 1st and 2nd

The obtained efficiency numbers for the 3rd jet seemed to be rather high so to exclude any possible double-counting mistakes the percentages for the 1st and 2nd jet where also calculated and compared. Since the considered percentage represents the number of times the 3rd jet corresponds to one of the actual light quarks should the sum of the three percentages not become any larger than 200%.

The percentages were calculated both before and after the application of the χ^2 algorithm and the results can be found in Tables 9.11 and 9.12. The first table shows the numbers before the application of the χ^2 algorithm implying that for correctly matched events 2 of the 3 light jets are correctly matched. The second table gives the results after the χ^2 minimization method.

	Number of events	Percentage (%)
Matched events	2455	
First jet	1596	65
Second jet	1740	70.9
Third jet	1574	64.1
Total	4910	200

Table 9.11: Number of times the first, second or third jet corresponds to one of the two correct light jets before the application of the χ^2 method.

	Number of events	Percentage (%)
Matched events	241	
First jet	162	67.2
Second jet	178	73.8
Third jet	142	58.9
Total	842	200

Table 9.12: Number of times the first, second or third jet corresponds to one of the two correct light jets after the application of the χ^2 method.

From these tables can be concluded that the obtained percentage of about 70% for the 3rd jet is actually correct and that the result can be trusted. It also implies that in the 5-jet case (meaning that there actually is a third light jet) the three jets have a rather similar probability of being the correct jet.

9.4.4 Considering separate categories

In order to be certain whether the 3rd light jet should be considered the considered events have been divided into two categories. The first only consists of events with exactly 2 light jets, hence 2 or more b-tagged jets¹ and 2 light jets, while the second category allows for more light jets. In case of multiple b-tagged jets only the two highest p_T jets are considered.

In the second category each event is treated in two separate ways. First the event is seen as a pure 4-jet event implying that only the two leading light jets are kept while for the second approach the third light jet is also included in the χ^2 algorithm resulting in 6 possible solutions.

For these three cases the matching and χ^2 minimization efficiency have been compared in order to ensure that the most efficient event selection will be used. The results can be found in Table 9.13 and indicates that including the third light jet doesn't result in a large gain of efficiency. On the contrary, including events with more than 4 jets but discarding the third light jet results in a significant decrease of efficiency.

	N(2 light jets)	N(2+ light jets)
# events	9328	6436
# matched events	4018	3319
# good combi chosen	3273	788 – 1604

Table 9.13: Number of events, number of matched events and number of events for which the correct jet combination is chosen using the $\chi^2 m_{lb} - m_{qqb}$ algorithm for the two considered categories. The first number in the right-hand bottom corner respresents the number of good combinations chosen when the event is treated as a 4-jet event while the second number is for the treatment of a 5-jet event. An event is considered as matching if the 4 jets corresponding to the generator event are included in the collection of selected jets.

The obtained results seem rather surprising since it implies that only asking the 4 leading jets results in the worst efficiencies.

However it should be noted that for this configuration the 2 Tight b-tag constraint might influence this result. It could be possible that for looser b-tag requirements the mis-identification of the two b-jets results in a worse “combination choice” efficiency.

	Only 4-jet events	All, but treated as 4-jet	All, but treated as 5-jet
% matched events	43.07	46.5	46.5
% good combi	81.4	55.3	66.5

Table 9.14: Percentages for matching the reconstructed event with the generated and for selecting the good combination using the $\chi^2 m_{lb} - m_{qqb}$ algorithm.

Is it possible to understand these results using the percentages for the first, second and third jet being correct .. ?

¹The number of events with a third b-tagged jet is extremely small and will probably not really influence the efficiency as can be seen from the plots shown in 9.4.4.1.

When treating a 5-jet event as a 4-jet event the correct jet would have been the third, discarded, jet in $\frac{1}{3}$ of the cases which explains the significant reduction. However the difference between treating the event as a 4-jet or a 5-jet event doesn't result in a large difference. It seems that in much of the $N(2+ \text{ light jet})$ cases the correct jet is actually still one of the following jets and is not included in the three leading light jets.

9.4.4.1 Histograms for number of selected, b-tagged and light jets

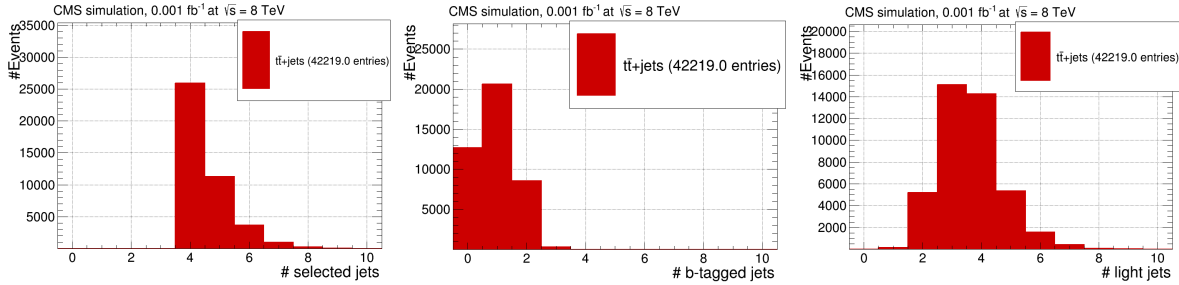


Figure 9.7: Number of selected, b-tagged and light jets, respectively, before requiring two Tight b-tags. These distributions are for the muon channel only.

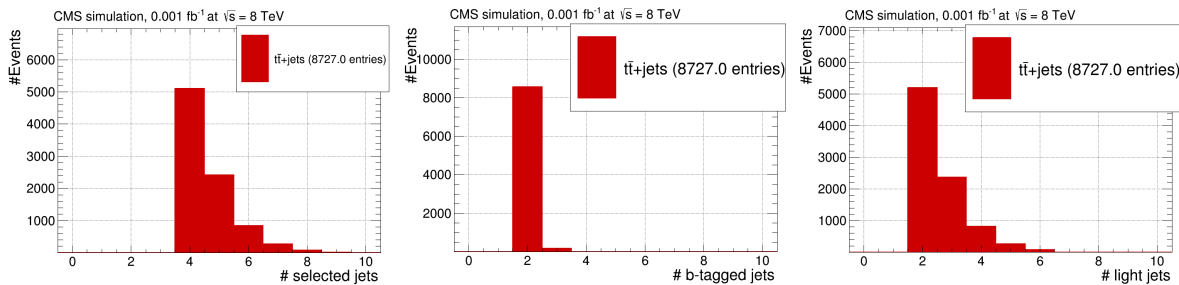


Figure 9.8: Number of selected, b-tagged and light jets, respectively, after requiring two Tight b-tags. These distributions are for the muon channel only.

9.5 Studying optimal cut on χ^2 value

The tables shown here indicate that the application of a cut on the χ^2 value of the m_{lb} - m_{qgb} method doesn't change the rates of good and wrong chosen events. Therefore it will only reduce the number of selected events, and hence reduce the needed CPU time, but still keep an as pure sample as obtained without any cut.

Since there is no real difference visible between setting the cut value to 3 or 5 it is advisable to use the cut value of 3 to reduce the number of selected events.

Option (with $\chi^2 m_{lb}$)	4 chosen jets are correct (%)	$\frac{s}{b}$	3rd jet is one of the 2 correct light jets (%)	3rd jet is chosen and correct (%)
5 jet case, 2 T b-tags	73.1485	2.72419	21.5302	89.0292
4 jet case, 2 T b-tags	76.89	3.32712	0	-nan
Pure 5 jet case, 2 T b-tags	65.5254	1.90068	74.5263	89.0292

Table 9.15: Overview of correct and wrong reconstructed events for the different b-tags when a $\chi^2 m_{lb} - m_{qqb}$ method is applied

Option (with $\chi^2 m_{lb}$)	% b's correct	$\frac{s}{b}$		
5 jet case, 2 T b-tags	90.3451	9.35743	0	0
4 jet case, 2 T b-tags	90.8573	9.93767	0	0
Pure 5 jet case, 2 T b-tags	89.8465	8.84884	0	0

Table 9.16: Overview of the number of times the correct b-jet combination is chosen when using a $\chi^2 m_{lb} - m_{qqb}$ method

Option (with $\chi^2 m_{lb}$)	4 chosen jets are correct (%)	$\frac{s}{b}$	3rd jet is one of the 2 correct light jets (%)	3rd jet is chosen and correct (%)
5 jet case, 2 T b-tags	72.8939	2.68921	21.7785	88.6241
4 jet case, 2 T b-tags	77.0226	3.3521	0	-nan
Pure 5 jet case, 2 T b-tags	64.7571	1.83745	74.192	88.6241

Table 9.17: Overview of correct and wrong reconstructed events for the different b-tags when a $\chi^2 m_{lb} - m_{qqb}$ method is applied

Option (with $\chi^2 m_{lb}$)	% b's correct	$\frac{s}{b}$		
5 jet case, 2 T b-tags	90.1586	9.16114	0	0
4 jet case, 2 T b-tags	90.8239	9.89789	0	0
Pure 5 jet case, 2 T b-tags	89.4472	8.47619	0	0

Table 9.18: Overview of the number of times the correct b-jet combination is chosen when using a $\chi^2 m_{lb} - m_{qqb}$ method

Option (with $\chi^2 m_{lb}$)	4 chosen jets are correct (%)	$\frac{s}{b}$	3rd jet is one of the 2 correct light jets (%)	3rd jet is chosen and correct (%)
5 jet case, 2 T b-tags	72.4364	2.62798	21.6013	87.5833
4 jet case, 2 T b-tags	77.3908	3.42298	0	-nan
Pure 5 jet case, 2 T b-tags	62.9538	1.69934	73.7615	87.5833

Table 9.19: Overview of correct and wrong reconstructed events for the different b-tags when a $\chi^2 m_{lb} - m_{qqb}$ method is applied

9.6. INFLUENCE OF USING p_T CUTS SUGGESTED BY THE TOP REFERENCE SELECTION TWIKI

Option (with $\chi^2 m_{lb}$)	% b's correct	$\frac{s}{b}$		
5 jet case, 2 T b-tags	90.233	9.23861	0	0
4 jet case, 2 T b-tags	90.9792	10.0854	0	0
Pure 5 jet case, 2 T b-tags	89.5385	8.55882	0	0

Table 9.20: Overview of the number of times the correct b-jet combination is chosen when using a $\chi^2 m_{lb} - m_{qgb}$ method

9.5.1 χ^2 required to be smaller than 5

9.5.2 χ^2 required to be smaller than 3

9.5.3 χ^2 required to be smaller than 1

9.6 Influence of using p_T cuts suggested by the TOP reference selection Twiki

The TOP Reference Selection Twiki, and the different subgroup Twikis, suggest to use different event selection requirements than used before. The values suggested can be found in the table below, together with the values which were used for producing the tables and figures given above.

In this section the different results will be compared for these two event selections in order to ensure that the influence of this event selection can be ignored. If this is not the case, all the above tables have to be replaced and updated (which will however happen on a larger time-scale since these will be the correct values which will be used further in this analysis). The main goal is to quickly check whether the conclusion obtained from the above figures and tables still remain valid.

	Old values	TOP RefSel values
selected jets	40 GeV	30 GeV
selected muons	25 GeV	26 GeV
selected electrons	32 GeV	30 GeV
veto muons	10 GeV	10 GeV
veto electrons	10 GeV	20 GeV

In the following table the number of selected events after the different event selection cuts which are applied in this analysis can be found. The left-handed columns contain the information when the old p_T cuts are applied while the right-handed columns gives the number of selected events when the recommendations of the Top Reference Selection Twiki are followed.

From the comparison of the two columns can be seen that lowering the p_T cut on the selected jets significantly improves the percentage of selected events, especially because of the improved selection efficiency for the third and fourth jet. This can easily be understood from the p_T distribution histogram for the different leading jets which can be found below. These distributions show that in the case of the fourth jet, moving the p_T cut from 30 GeV to 40 GeV cuts away the largest percentage of this fourth jet since its distribution is peaked at a lower p_T value. The influence is much lower for the first and

Table 9.21: Event selection table before (left) and after (right) the p_T cuts were updated to the ones suggested by the TOP reference twiki, for Semi-elec channel $t\bar{t} + jets$. (19600.8 pb^{-1} of int. lumi.)

	Old p_T cuts		New p_T cuts	
preselected	1.91516e+07		1.91516e+07	
triggered	3.52179e+06	18.4 %	3.52179e+06	18.4 %
Good PV	3.52179e+06	100 %	3.52179e+06	100 %
1 selected electron	2.76014e+06	78.4 %	2.85992e+06	81.2 %
Veto muon	2.75335e+06	99.8 %	2.8529e+06	99.8 %
Veto 2nd electron from Z-decay	2.7483e+06	99.8 %	2.84766e+06	99.8 %
Conversion veto	2.7483e+06	100 %	2.84766e+06	100 %
≥ 1 jets	2.72998e+06	99.3 %	2.84406e+06	99.9 %
≥ 2 jets	2.50625e+06	91.8 %	2.77442e+06	97.6 %
≥ 3 jets	1.74245e+06	69.5 %	2.34978e+06	84.7 %
≥ 4 jets	0.753281e+06	43.2 %	1.38732e+06	59.0 %

second jet because their distribution is maximal around 100 GeV so changing this p_T cut only affects the left side of the tail of the distribution.

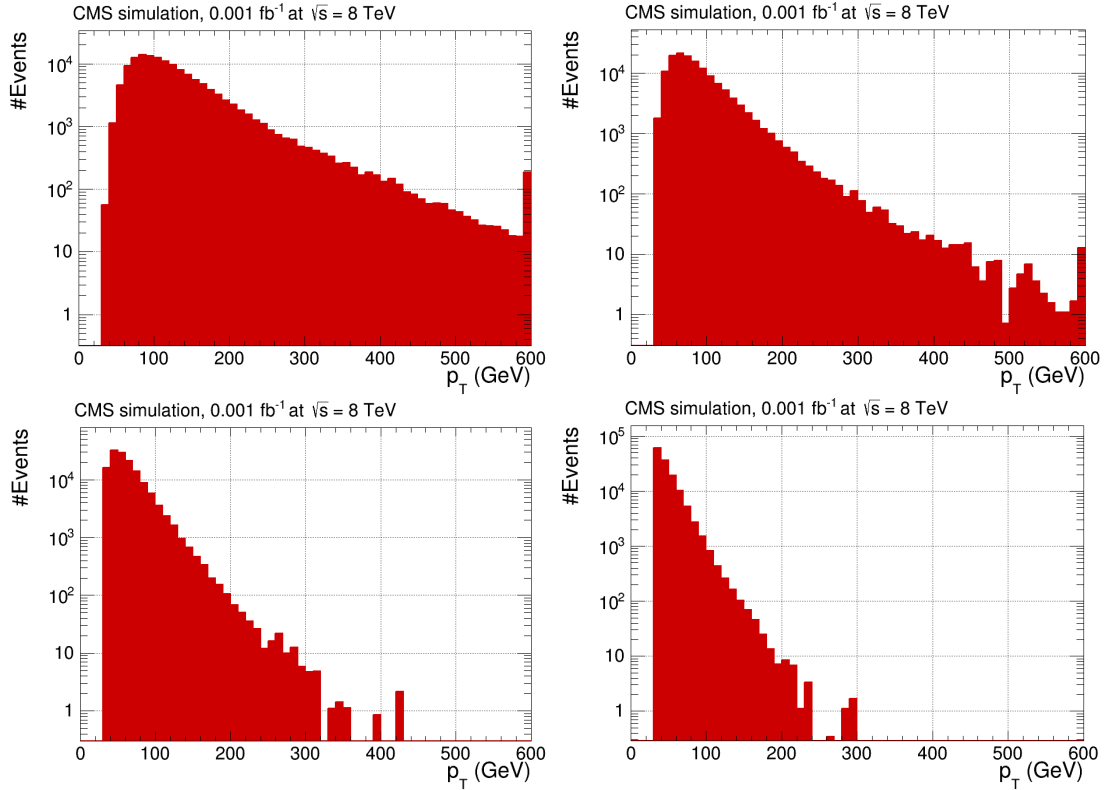


Figure 9.9: P_T distributions for the first, second, third and fourth jet respectively. All four histograms are for the semi-electronic decay channel. (Information about the Cross Section and number of events should be ignored for the moment. Correct Cross Section value is not yet used ...)

Table 9.22: Event selection table before (left) and after (right) the p_T cuts were updated to the ones suggested by the TOP reference twiki, for Semi-muon channel $t\bar{t} + jets$. (19600.8 pb^{-1} of int. lumi.)

	Old p_T cuts		New p_T cuts	
preselected	1.91516e+07		1.91516e+07	
triggered	4.01265e+06	20.9 %	4.01265e+06	20.9 %
Good PV	4.01265e+06	100 %	4.01265e+06	100 %
1 selected muon	3.46903e+06	86.4 %	3.40822e+06	84.9 %
Veto 2nd muon	3.46369e+06	99.8 %	3.40291e+06	99.8 %
Veto electron	3.45244e+06	99.7 %	3.39184e+06	99.7%
≥ 1 jets	3.4281e+06	99.3 %	3.38698e+06	99.9 %
≥ 2 jets	3.14456e+06	91.7 %	3.30209e+06	97.5 %
≥ 3 jets	2.19456e+06	69.8 %	2.80066e+06	84.8 %
≥ 4 jets	944572	43.0 %	1.65345e+06	59.0 %

The same table can be created for the semi-muonic decay channel which shows a similar result.

9.6.1 Influence on choice of b-tag option and use of $\chi^2 m_{lb} - m_{qqb}$ method

With these new values considered for the event selection requirements, the obtained percentages and $\frac{s}{b}$ values should be compared again. The values which are obtained using these new p_T cuts can be found in the following tables.

The first three tables show the results before the use of a $\chi^2 m_{lb} - m_{qqb}$ method while the last two tables give the obtained numbers when this $\chi^2 m_{lb} - m_{qqb}$ method is applied.

Analyzing the numbers in these tables clearly indicates that the obtained results for the old p_T cuts correspond to the values obtained earlier, which implies that the obtained values can easily be compared against each other and still represent the same variables. The small differences which are however visible can be easily explained by statistical deviations.

Comparing the results obtained using the new p_T cut values with the ones using the old cut values clearly indicates that the old values resulted in slightly better selection efficiency and $\frac{s}{b}$ value. Both for the selection efficiency of the b-quark jets and the light jets a higher percentage is found when using the old p_T cut values.

A positive remark corresponding to the new p_T cut values is that the behavior of the different considered b-tag options is similar. The 2 Tight b-tag case without any veto on the light jets results in the highest selection efficiency and $\frac{b}{s}$ value. Hence the choice of the used b-tag option does not need to be updated.

Even the use of a $\chi^2 m_{lb} - m_{qqb}$ method doesn't improve the selection efficiency and $\frac{s}{b}$ values when changing to the newer p_T cut values. However compared to the previous case when no $\chi^2 m_{lb} - m_{qqb}$ method is applied the difference between the two p_T cut options becomes slightly less significant (from 18 % to 13 % difference). Still no improvement can be found implying that lowering the p_T cut on the jets only increases the number of selected events but doesn't insure selection more good events, on the contrary the selection efficiencies decreases even.

		Option (no $\chi^2 m_{lb}$)	all 4 correct	≥ 1 wrong	correct (%)	$\frac{s}{b}$	non-matched
New p_T cuts	L b-tags	31797	36132	46.8092	0.880023	103988	
	2 M b-tags	28380	21485	56.9137	1.32092	63717	
	2 M b-tags, light L-veto	21578	18821	53.4122	1.14649	50549	
	2 T b-tags	17858	10684	62.5674	1.67147	33551	
	2 T b-tags, light M-veto	16574	10496	61.2264	1.57908	31778	
	2 T b-tags, light L-veto	12664	9552	57.004	1.3258	25440	
Old p_T cuts	2 L b-tags	15285	13577	52.9589	1.1258	61307	
	2 M b-tags	13480	8590	61.0784	1.56927	39800	
	2 M b-tags, light L-veto	10718	7461	58.9581	1.43654	32048	
	2 T b-tags	8555	4231	66.9091	2.02198	21234	
	2 T b-tags, light M-veto	7915	4097	65.8924	1.9319	19946	
	2 T b-tags, light L-veto	6327	3701	63.0933	1.70954	16156	

Table 9.23: Overview of correct and wrong reconstructed events for the different b-tags without the use of a $\chi^2 m_{lb} - m_{qqb}$ method

	Option (no $\chi^2 m_{lb}$)	2 b's correct	≥ 1 b wrong	b's correct (%)	$\frac{s}{b}$	non-matched
New p_T cuts	2 L b-tags	47926	20003	70.5531	2.39594	103988
	2 M b-tags	42045	7820	84.3177	5.3766	63717
	2 M b-tags, light L-veto	34622	5777	85.7001	5.99308	50549
	2 T b-tags	26117	2425	91.5037	10.7699	33551
	2 T b-tags, light M-veto	24974	2096	92.2571	11.9151	31778
	2 T b-tags, light L-veto	20585	1631	92.6584	12.6211	25440
Old p_T cuts	2 L b-tags	21456	7406	74.34	2.89711	61307
	2 M b-tags	18863	3207	85.469	5.88182	39800
	2 M b-tags, light L-veto	15859	2320	87.238	6.83578	32048
	2 T b-tags	11811	975	92.3745	12.1138	21234
	2 T b-tags, light M-veto	11203	809	93.2651	13.848	19946
	2 T b-tags, light L-veto	9424	604	93.9769	15.6026	16156

Table 9.24: Overview of correct and wrong reconstructed b-jets for the different b-tags without the use of a $\chi^2 m_{lb} - m_{qqb}$ method

	Option (no $\chi^2 m_{lb}$)	2 light good	≥ 1 light wrong	light correct (%)	$\frac{s}{b}$	non-matched
New p_T cuts	2 L b-tags	33731	34198	49.6563	0.986344	103988
	2 M b-tags	28893	20972	57.9424	1.37769	63717
	2 M b-tags, light L-veto	22118	18281	54.7489	1.20989	50549
	2 T b-tags	18030	10512	63.1701	1.71518	33551
	2 T b-tags, light M-veto	16788	10282	62.017	1.63276	31778
	2 T b-tags, light L-veto	12868	9348	57.9222	1.37655	25440
Old p_T cuts	2 L b-tags	16015	12847	55.4882	1.24659	61307
	2 M b-tags	13688	8382	62.0208	1.63302	39800
	2 M b-tags, light L-veto	10938	7241	60.1683	1.51056	32048
	2 T b-tags	8627	4159	67.4722	2.0743	21234
	2 T b-tags, light M-veto	8005	4007	66.6417	1.99775	19946
	2 T b-tags, light L-veto	6409	3619	63.911	1.77093	16156

Table 9.25: Overview of correct and wrong reconstructed light jets for the different b-tags without the use of a $\chi^2 m_{lb} - m_{qqb}$ method

	Option (with $\chi^2 m_{lb}$)	all 4 correct	≥ 1 wrong	4 chosen jets correct (%)	$\frac{s}{b}$	non-matched
New p_T cuts	2 L b-tags	24611	43318	77.4004	0.568147	103988
	2 M b-tags	21813	28052	76.8605	0.777592	63717
	2 M b-tags, light L-veto	16731	23668	77.5373	0.706904	50549
	2 T b-tags	13681	14861	76.6099	0.920598	33551
	2 T b-tags, light M-veto	12674	14396	76.4692	0.880383	31778
	2 T b-tags, light L-veto	9757	12459	77.0452	0.783129	25440
Old p_T cuts	2 L b-tags	11893	16969	77.8083	0.700866	61307
	2 M b-tags	10422	11648	77.3145	0.894746	39800
	2 M b-tags, light L-veto	8369	9810	78.0836	0.853109	32048
	2 T b-tags	6581	6205	76.9258	1.0606	21234
	2 T b-tags, light M-veto	6080	5932	76.8162	1.02495	19946
	2 T b-tags, light L-veto	4903	5125	77.4933	0.956683	16156

Table 9.26: Overview of correct and wrong reconstructed events for the different b-tags when a $\chi^2 m_{lb} - m_{qqb}$ method is applied

	Option (with $\chi^2 m_{lb}$)	Correct b's	Wrong b's	% b's correct	$\frac{s}{b}$	Correct option exists
New p_T cuts	2 L b-tags	28190	3607	88.6562	7.81536	31797
	2 M b-tags	25143	3237	88.5941	7.76738	28380
	2 M b-tags, light L-veto	19183	2395	88.9007	8.0096	21578
	2 T b-tags	15736	2122	88.1174	7.41565	17858
	2 T b-tags, light M-veto	14586	1988	88.0053	7.33702	16574
	2 T b-tags, light L-veto	11178	1486	88.266	7.52221	12664
Old p_T cuts	2 L b-tags	13935	1350	91.1678	10.3222	15285
	2 M b-tags	12306	1174	91.2908	10.4821	13480
	2 M b-tags, light L-veto	9808	910	91.5096	10.778	10718
	2 T b-tags	7765	790	90.7656	9.82911	8555
	2 T b-tags, light M-veto	7172	743	90.6128	9.65276	7915
	2 T b-tags, light L-veto	5743	584	90.7697	9.8339	6327

Table 9.27: Overview of the number of times the correct b-jet combination is chosen when using a $\chi^2 m_{lb} - m_{qqb}$ method

Chapter 10

Event corrections and reconstruction

Chapter 11

Theory link with partial widths

11.1 Partial width of top-quark decay

The partial width of the top-quark decay can be expressed in terms of the anomalous couplings in the Wtb interaction as represented in the following equations. The first and less extensive one describes the longitudinal decay.

$$\begin{aligned} \Gamma_0 = & \frac{g^2 |\vec{q}|}{32\pi} \left\{ \frac{m_t^2}{m_W^2} \left[|V_L|^2 + |V_R|^2 \right] (1 - x_W^2 - 2x_b^2 - x_W^2 x_b^2 + x_b^4) - 4x_b \text{Re} V_L V_R^* \right. \\ & + \left[|g_L|^2 + |g_R|^2 \right] (1 - x_W^2 + x_b^2) - 4x_b \text{Re} g_L g_R^* \\ & - 2 \frac{m_t}{m_W} \text{Re} [V_L g_R^* + V_R g_L^*] (1 - x_W^2 - x_b^2) \\ & \left. + 2 \frac{m_t}{m_W} x_b \text{Re} [V_L g_L^* + V_R g_R^*] (1 + x_W^2 - x_b^2) \right\} \end{aligned} \quad (11.1)$$

with:

$$x_W = \frac{m_W}{m_t} \quad (11.2a)$$

$$x_b = \frac{m_b}{m_t} \quad (11.2b)$$

$$|\vec{q}| = \frac{1}{2m_t} \sqrt{m_t^4 + m_W^4 + m_b^4 - 2m_t^2 m_W^2 - 2m_t^2 m_b^2 - 2m_W^2 m_b^2} \quad (11.2c)$$

A similar equation can also be formulated for the left- and right-handed top-quark decay, which only differ partially with a minus sign. The right-handed part corresponds

to the plus-sign option while the left-handed contribution contains the minus-sign.

$$\begin{aligned}
\Gamma_{R,L} = & \frac{g^2 |\vec{q}|}{32\pi} \left\{ \frac{m_t^2}{m_W^2} \left[|V_L|^2 + |V_R|^2 \right] (1 - x_W^2 + x_b^2) - 4x_b \text{Re} V_L V_R^* \right. \\
& + \frac{m_t^2}{m_W^2} \left[|g_L|^2 + |g_R|^2 \right] (1 - x_W^2 - 2x_b^2 - x_W^2 x_b^2 + x_b^4) - 4x_b \text{Re} g_L g_R^* \\
& - 2 \frac{m_t}{m_W} \text{Re} [V_L g_R^* + V_R g_L^*] (1 - x_W^2 - x_b^2) \\
& \left. + 2 \frac{m_t}{m_W} x_b \text{Re} [V_L g_L^* + V_R g_R^*] (1 + x_W^2 - x_b^2) \right\} \\
& \pm \frac{g^2 m_t^3}{64\pi m_W^2} \left\{ -x_W^2 \left[|V_L|^2 - |V_R|^2 + |g_L|^2 - |g_R|^2 \right] (1 - x_b^2) \right. \\
& + 2x_W \text{Re} [V_L g_R^* + V_R g_L^*] + 2x_W x_b \text{Re} [V_L g_L^* + V_R g_R^*] \\
& \times (1 - 2x_W^2 - 2x_b^2 + x_W^4 - 2x_W^2 x_b^2 + x_b^4) \tag{11.3}
\end{aligned}$$

In order to transform these partial width formulas into helicity fractions, also the total width of the top quark decay is needed. This because each helicity fraction is defined as the corresponding partial width divided by the total width.

$$\begin{aligned}
\Gamma = & \frac{g^2 |\vec{q}| m_t^2}{32\pi m_W^2} \left\{ \left[|V_L|^2 + |V_R|^2 \right] (1 + x_W^2 - 2x_b^2 - 2x_W^4 + x_W^2 x_b^2 + x_b^4) - 4x_b \text{Re} V_L V_R^* \right. \\
& - 12x_W^2 x_b \text{Re} V_L V_R^* + 2 \left[|g_L|^2 + |g_R|^2 \right] \left(1 - \frac{x_W^2}{2} - 2x_b^2 - \frac{x_X^4}{2} - \frac{x_W^2 x_b^2}{2} + x_b^4 \right) \\
& - 12x_W^2 x_b \text{Re} g_L g_R^* - 6x_W \text{Re} [V_L g_R^* + V_R g_L^*] (1 - x_W^2 - x_b^2) \\
& \left. 6x_W x_b \text{Re} [V_L g_L^* + V_R g_R^*] (1 + x_W^2 - x_b^2) \right\} \tag{11.4}
\end{aligned}$$

11.2 Simplification in limit-cases

11.2.1 Only 1 coupling non-zero

If we consider the case where only the V_L coupling parameter is non-zero, the above definitions get reduced to the following formulas.

$$\Gamma_0 = \frac{g^2 |\vec{q}| m_t^2}{32\pi m_W^2} |V_L|^2 (1 - x_W^2 - 2x_b^2 - x_W^2 x_b^2 + x_b^4) \tag{11.5}$$

$$\Gamma_{R,L} = \frac{g^2 |\vec{q}|}{32\pi} |V_L|^2 (1 - x_W^2 + x_b^2) \pm \frac{g^2 m_t^3}{64\pi m_W^2} \left\{ -x_W^2 |V_L|^2 (1 - x_b^2) \right\} \tag{11.6}$$

$$\Gamma = \frac{g^2 |\vec{q}| m_t^2}{32\pi m_W^2} |V_L|^2 (1 + x_W^2 - 2x_b^2 - 2x_W^4 + x_W^2 x_b^2) \tag{11.7}$$

So this implies that the helicity fractions can be defined as follows:

$$F_0 = \frac{\Gamma_0}{\Gamma} = \frac{(1 - x_W^2 - 2x_b^2 - x_W^2 x_b^2 + x_b^4)}{(1 + x_W^2 - 2x_b^2 - 2x_W^4 + x_W^2 x_b^2)} \quad (11.8)$$

$$\begin{aligned} F_{R,L} = \frac{\Gamma_{R,L}}{\Gamma} &= \frac{m_W^2}{m_t^2} \frac{(1 - x_W^2 + x_b^2)}{(1 + x_W^2 - 2x_b^2 - 2x_W^4 + x_W^2 x_b^2)} \\ &\pm \frac{m_t}{2|\vec{q}|} \frac{-x_W^2(1 - x_b^2)}{(1 + x_W^2 - 2x_b^2 - 2x_W^4 + x_W^2 x_b^2)} \end{aligned} \quad (11.9)$$

From the above two equations can easily be concluded that in cases where only one of the Wtb-coupling coefficients is non-zero, there will be no influence visible on the helicity fractions. This because no interference between different coupling coefficients occurs which allows the cancellation of this single coupling coefficient. This behavior is indeed retrieved in the different $\cos \theta^*$ distributions which have been studied in detail. The ones with only one coupling constant active can be found in Figure 11.1.

It is important to note that the same is also true when only the real and imaginary part of one coupling are varied. In those cases there is also no interference between different coupling constants which is necessary in order to introduce a different between the partial widths and the total width. For example when considering only the left-handed vector coupling, the only term which remains in the width definitions is $|V_L|^2 = Re(V_L)^2 + Im(V_L)^2$. However since it does not matter whether this term consists of both the real and the imaginary part or only the real part, it will cancel out when dividing the partial width part by the total width. This behavior is indeed retrieved in the $\cos \theta^*$ distributions, as can be seen in Figure 11.2.

11.2.2 Massless b-limit

Within the Wtb interaction the mass of the bottom quark is almost negligible compared to the massive W-boson and the top quark. Hence it is rather standard to use a so-called massless b-limit when considering the Wtb interaction, an approach which also explains the suppression of the right-handed helicity fraction of the W-boson.

When applying this assumption, the partial and total width formulas can be simplified significantly as will be shown in the following equations since the terms containing x_b can be neglected. For simplicity only the real parts of the vector couplings are considered, but the same is true for other combinations.

$$\Gamma_0 = \frac{g^2 |\vec{q}| m_t^2}{32\pi m_W^2} [|V_L|^2 + |V_R|^2] (1 - x_W^2) \quad (11.10)$$

$$\begin{aligned} \Gamma_{R,L} &= \frac{g^2 |\vec{q}| m_t^2}{32\pi m_W^2} [|V_L|^2 + |V_R|^2] (1 - x_W^2) \\ &\pm \frac{g^2}{64\pi} \frac{m_t^3}{m_W^2} \left\{ -x_W^2 [|V_L|^2 - |V_R|^2] \right\} (1 - 2x_W^2 + x_W^4) \end{aligned} \quad (11.11)$$

$$\Gamma = \frac{g^2 |\vec{q}| m_t^2}{32\pi m_W^2} [|V_L|^2 + |V_R|^2] (1 + x_W^2 - 2x_W^4) \quad (11.12)$$

From this can be seen that the longitudinal helicity fraction is not influenced at all when working in the massless b-limit. The right-handed and left-handed helicity fractions,

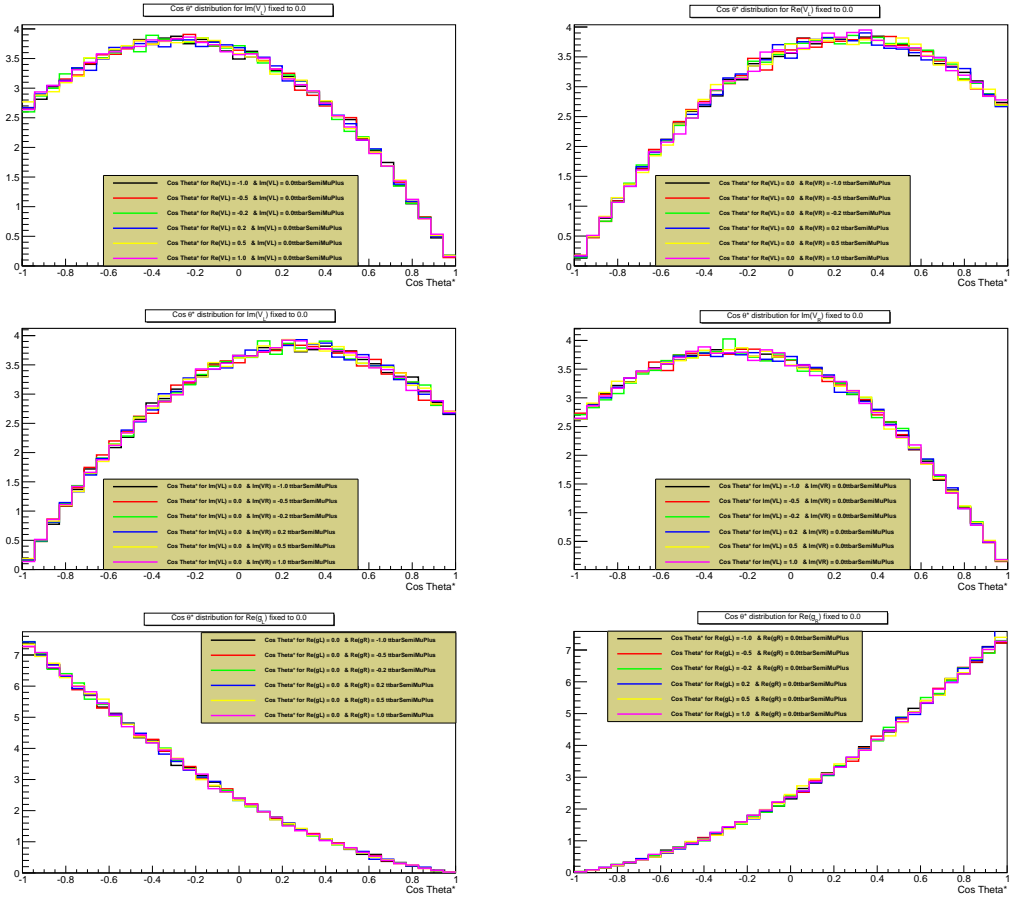


Figure 11.1: Distributions of $\cos \theta^*$ for configurations where only one of the Wtb-coupling coefficients is non-zero while the other one is varied between -1 and 1 . The two upper distributions show the case when only the real part of the two vector couplings is non-zero while the two middle ones represent the case when only their imaginary part is non-zero. Finally the two lower distributions give the $\cos \theta^*$ distribution for the real part of the tensor couplings. The same conclusion holds for all distributions shown here, namely that no shape difference occurs when only one of the couplings is non-zero as was indicated by the formulas given above.

on the other hand, have an opposite coupling-coefficient dependent part. This is again clearly visible in the studied $\cos \theta^*$ distributions, which all behave similar around $\cos \theta^* = 0$. This is shown in Figure 11.3.

11.2.3 Only 1 coupling non-zero within the massless b-limit

The equations defined when considering only 1 non-zero coupling, Equations (11.8) and (11.14), can be simplified even further when assuming the massless b-limit.

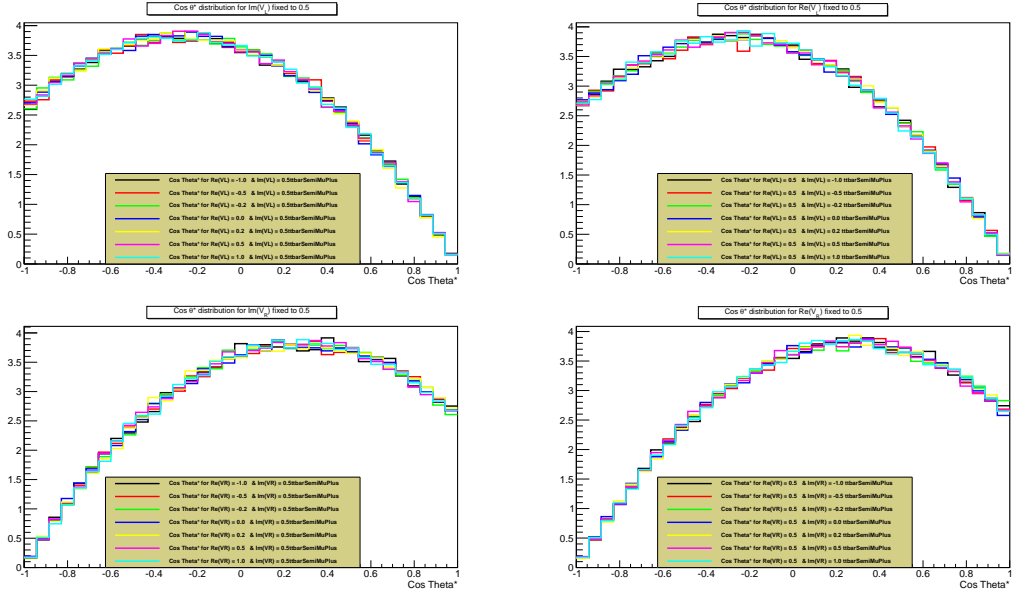


Figure 11.2

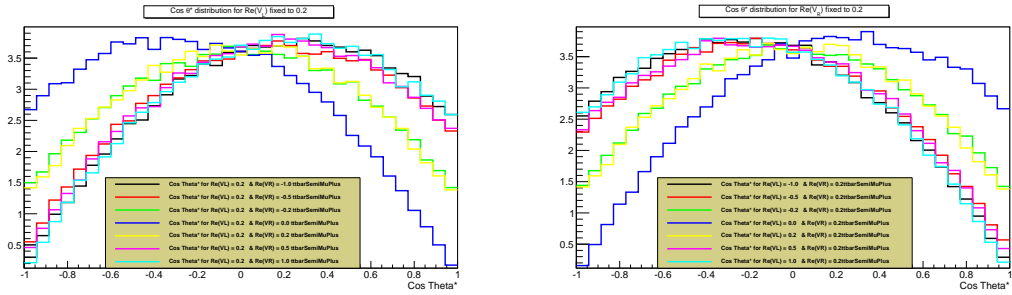


Figure 11.3: ...

$$F_0 = \frac{(1 - x_W^2 - 2x_b^2 - x_W^2 x_b^2 + x_b^4)}{(1 + x_W^2 - 2x_b^2 - 2x_W^4 + x_W^2 x_b^2)} \quad (11.13)$$

$$F_{R,L} = \frac{m_W^2}{m_t^2} \frac{(1 - x_W^2 + x_b^2)}{(1 + x_W^2 - 2x_b^2 - 2x_W^4 + x_W^2 x_b^2)} \pm \frac{m_t}{2|\vec{q}|} \frac{-x_W^2(1 - x_b^2)}{(1 + x_W^2 - 2x_b^2 - 2x_W^4 + x_W^2 x_b^2)} \quad (11.14)$$

For the simplified case where only 1 of the couplings is varied the dependency on the top quark mass can be calculated explicitly by using Equations (11.2). Applying these

definitions changes Equations (11.8) and (11.14) as follows¹:

$$\begin{aligned}
 F_0 &= \frac{1 - x_W^2 - 2x_b^2 - x_W^2 x_b^2 + x_b^4}{1 + x_W^2 - 2x_b^2 - 2x_W^4 + x_W^2 x_b^2} \\
 &= \frac{1 - \frac{m_W^2}{m_t^2} - 2\frac{m_b^2}{m_t^2} - \frac{m_W^2}{m_t^2} \frac{m_b^2}{m_t^2} + \frac{m_b^4}{m_t^4}}{1 + \frac{m_W^2}{m_t^2} - 2\frac{m_b^2}{m_t^2} - 2\frac{m_W^4}{m_t^4} + \frac{m_W^2}{m_t^2} \frac{m_b^2}{m_t^2}} \\
 &= \frac{m_t^4}{m_t^4} \frac{m_t^4 - m_W^2 m_t^2 - 2m_b^2 m_t^2 - m_W^2 m_b^2 + m_b^4}{1 + m_W^2 m_t^2 - 2m_b^2 m_t^2 - 2m_W^4 + m_W^2 m_b^2 + m_b^4} \\
 &\approx_{m_b=0} \frac{m_t^4 - m_W^2 m_t^2}{m_t^4 + m_W^2 m_t^2 - 2m_W^4}
 \end{aligned}$$

$$\begin{aligned}
 F_{R,L} &= \frac{m_W^2}{m_t^2} \frac{1 - x_W^2 + x_b^2}{1 + x_W^2 - 2x_b^2 - 2x_W^4 + x_W^2 x_b^2} \pm \frac{m_t}{2|\vec{q}|} \frac{-x_W^2 (1 - 2x_W^2 - 2x_b^2 + x_W^4 - 2x_W^2 x_b^2 + x_b^4)}{1 + x_W^2 - 2x_b^2 - 2x_W^4 + x_W^2 x_b^2} \\
 &= \frac{m_t^4}{m_t^4} \left\{ \frac{m_W^2}{m_t^2} \frac{1 - m_W^2 m_t^2 + m_b^2 m_t^2}{1 + m_W^2 m_t^2 - 2m_b^2 m_t^2 - 2m_W^4 + m_W^2 m_b^2} \right. \\
 &\quad \left. \pm \frac{m_t}{2|\vec{q}|} \frac{-m_W^2 m_t^4 - 2m_W^2 m_t^2 - 2m_b^2 m_t^2 + m_W^4 - 2m_W^2 m_b^2 + m_b^4}{m_t^4 + m_W^2 m_t^2 - 2m_b^2 m_t^2 - 2m_W^4 + m_W^2 m_b^2} \right\} \\
 &\approx \frac{m_W^2}{m_t^2} \frac{m_t^4 - m_W^2 m_t^2}{1 + m_W^2 m_t^2 - 2m_W^4} \pm \frac{m_t}{2|\vec{q}|} \frac{-m_W^2 m_t^4 - 2m_W^2 m_t^2 + m_W^4}{m_t^2 m_t^4 + m_W^2 m_t^2 - 2m_W^4} \\
 &\approx \frac{m_W^2}{m_t^2} \frac{m_t^2(m_t^2 - m_W^2)}{m_t^4 + m_W^2 m_t^2 - 2m_W^4} \pm \frac{2m_t^2}{2(m_t^2 - m_W^2)} \frac{-m_W^2}{m_t^2} \frac{(m_t^2 - m_W^2)^2}{m_t^4 + m_W^2 m_t^2 - 2m_W^4} \\
 &\approx m_W^2 \left(\frac{m_t^2 - m_W^2}{m_t^4 + m_W^2 m_t^2 - 2m_W^4} \right) \mp m_W^2 \left(\frac{m_t^2 - m_W^2}{m_t^4 + m_W^2 m_t^2 - 2m_W^4} \right) \\
 &= \begin{cases} 0 & \text{for right-handed helicity fraction} \\ 2m_W^2 \frac{m_t^2 - m_W^2}{m_t^4 + m_W^2 m_t^2 - 2m_W^4} & \text{for left-handed helicity fraction} \end{cases}
 \end{aligned}$$

Hence when creating the $\cos \theta^*$ distribution for different top-quark masses it is expected to see a clear shape difference for the left-handed helicity fraction. As postulated by the Standard Model, no right-handed contribution is expected and from the above equation is clear that this contribution does not depend on the considered top-quark mass. Again this can be seen on the $\cos \theta^*$ distributions when varying the top quark mass between 153 GeV and 193 GeV in steps of 10 GeV, as shown in Figure 11.4.

11.3 Understanding symmetric behavior

While studying all the different $\cos \theta^*$ distributions for all the considered configurations, there was one peculiar observation. Every studied $\cos \theta^*$ distribution clearly showed a symmetric relationship between the negative and positive part of each coupling coefficient. Again this can be explained using the partial top quark width definitions given above since with these equations it is possible to track down the term which depends on the sign of the coefficient.

¹This because within this massless b-limit $|\vec{q}|$ can be simplified to $\frac{m_t^2 - m_W^2}{2m_t}$.

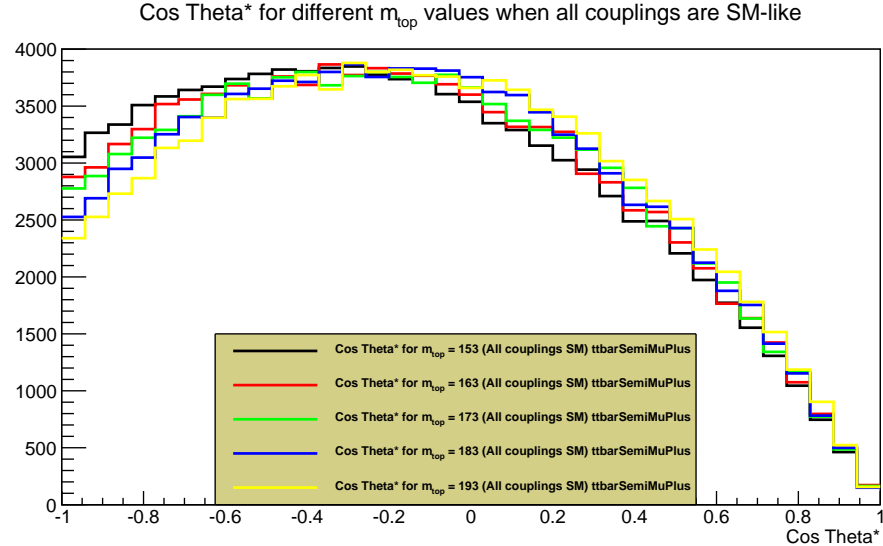


Figure 11.4: Distribution of $\cos \theta^*$ when varying the top quark mass.

The only terms which need to know the sign of the considered coefficient are the mixing terms such as $ReV_L V_R^*$ for example. However most of these mixing terms, and all of the most straightforward ones, are scaled with a factor x_b implying that they are negligible in the massless b-limit. So mixing the vector and tensor couplings should give less symmetric $\cos \theta^*$ distributions than the current studied mixings between vector and tensor couplings separately.

Figure 11.5 clearly shows that the symmetric behavior is caused by low mass of the bottom quark. Both distributions represent an identical configuration, with the only difference the bottom-quark mass.

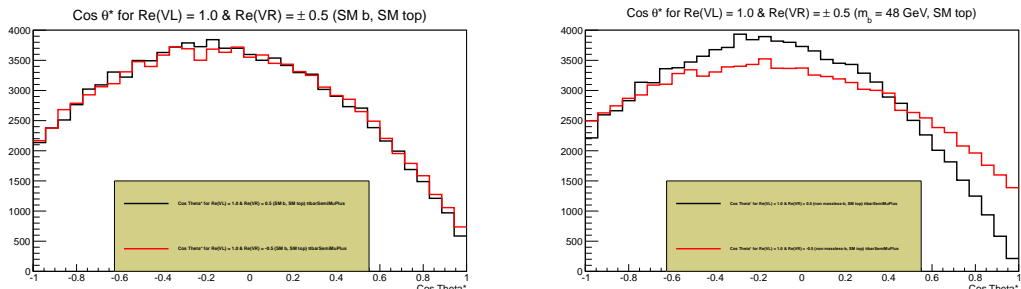


Figure 11.5: Influence of bottom-quark mass

Chapter 12

Likelihood optimization

First results of the $-\ln(\mathcal{L})$ distribution of the right-handed vector coefficient, V_R , for reco-level events indicated that the expected shape, a minimum around $V_R = 0$, is not retrieved. However this behavior is recovered for generator-level events. Therefore this can be seen as a clear influence of the event selection and further investigation of the origin of this deviation might possibly result in an improved likelihood distribution. Hence effort has been put in investigating whether a specific cut on the likelihood distribution can result in the desired distribution.

Since the reco-level events are simulated using the Standard Model constraints, namely $V_R = 0$, this value should be recovered using the MadWeight output in order to exclude any bias caused by the event selection.

12.1 Comparison between correct, wrong and un-matched jet combinations

As a first step the chosen $t\bar{t}$ jet combination has been divided in distinct categories based on the jet-parton matching output: correctly matched, wrongly matched and un-matched jet combinations. Since the wrongly-matched can be considered as a kind of background sample while the correctly matched correspond to clear signal events, their comparison can result in a possible hint for an optimal cut in order to reduce the contribution of background events. The number of events in each of these categories is given in the following table:

Table 12.1: Grouping of the different jet-matching types for 10 000 ttbar semi-muonic (+) events.

Correctly matched	Wrongly matched	Unmatched
13 608	15 345	34 176
21.56 %	24.31 %	54.14 %

The top mass distributions, leptonically and hadronically decaying top, for each of the categories can be seen in Figure 12.1.

The obtained mass distributions show mostly the expected behavior, indicating that the leptonically decaying top quark is less dependent of the correctness of the chosen jet combinations. The hadronically decaying top quark on the other hand is significantly influenced by the chosen jet combination as can be seen by the large difference in tail for

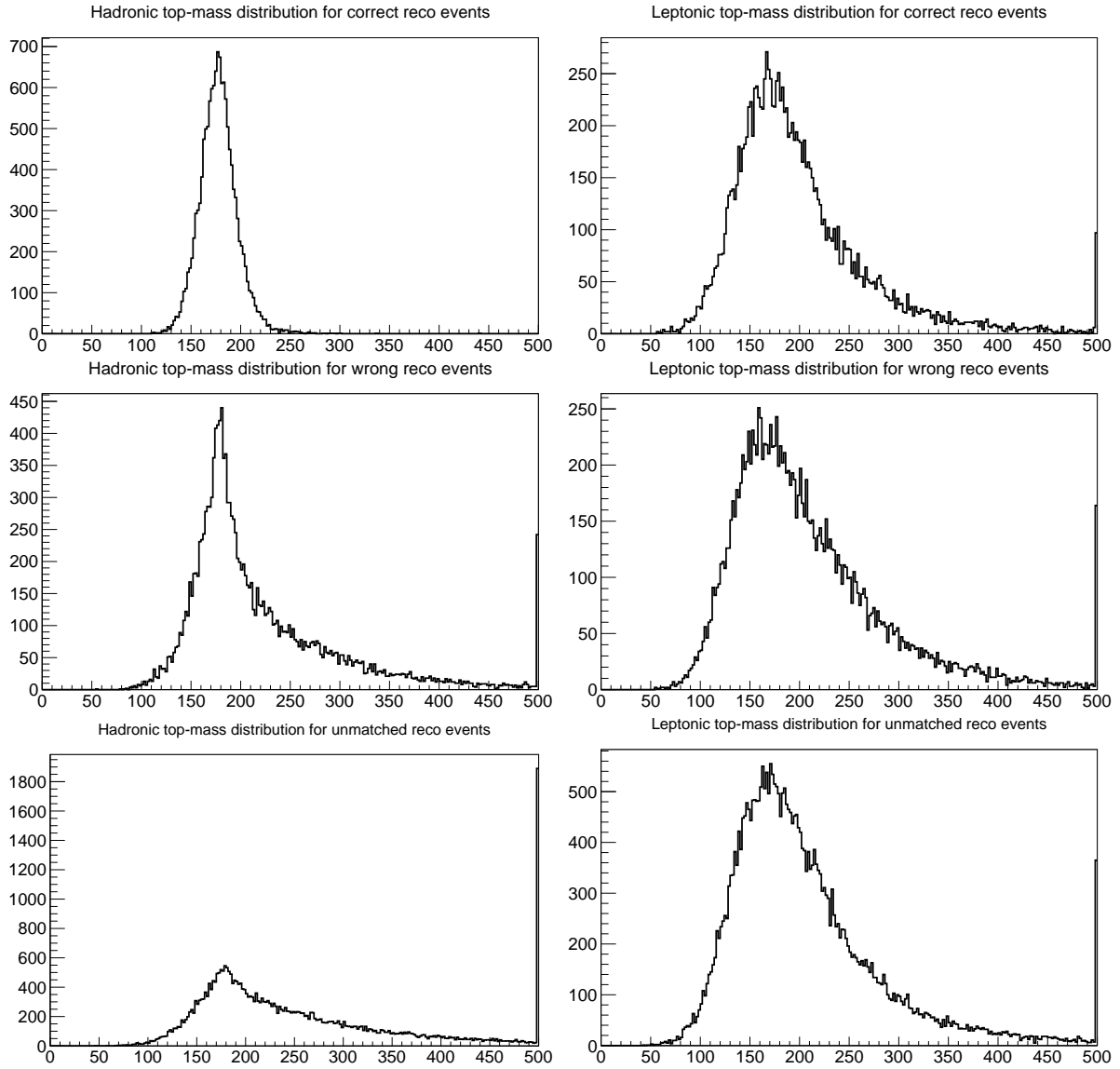


Figure 12.1: Distributions for the hadronically (left) and leptonically (right) decaying top quark mass for the correctly matched, wrongly matched and unmatched jet combinations, respectively.

the correctly and wrongly matched jet combinations.

The mass distribution of the hadronically decaying top quark for un-matched reco-level events show a rather unexpected behavior on the other hand ...

I expected that this distribution would more be like a combination of the correctly and wrongly matched ones since in quite a lot of cases the correct parton-level jet combination is not available in the list of matched jet combinations. These should then be recovered when looking at the entire list of unmatched jet combinations. Of course quite often the wrong combination will be chosen, but still it seems rather strange that the tail of the unmatched jet combinations is significantly higher and more energetic than the one corresponding to the wrongly matched jet combinations ...

12.1.1 Inefficiency of MadWeight depends on category-type

When using the different categories for Matrix Element calculations, the number of events successfully calculated depends quite heavily on the category considered. Although it is important to mention that quite often this efficiency can vary when resubmitting the same configuration which could hint towards an influence of the cluster used for running the calculations.

The number of remaining events which have been used for the measurements discussed further in this Chapter are given in Table 12.2.

Table 12.2: Number of events for each of the four considered categories successfully calculated by MadWeight. The number of failing events, for which a weight equal to 0.0 has been returned or for which one of the considered configurations is missing, is especially significant for the category of unmatched reco-level events.

Category	Generator-level events	Reco-level events		
		Correctly matched	Wrongly matched	Unmatched
Succesfull events	10000	9982	9085	7538

12.2 Measurement of top-quark mass using Matrix Element Method

In order to check the influence of the event selection, first the measurement of the top-quark mass has been performed using MadWeight. This event selection influence can then be understood by comparing the obtained measurement of the top quark mass on generator level with the one on reco-level. The results of the generator-level measurement can be found in Figure 12.2 and Table 12.3 while Figure ??

For this type of events no acceptance normalisation can be applied since no event selection is applied on these generator-level events. Hence the only normalisation which can be applied is the cross-section normalisation.

Table 12.3: Fit parameters of 2nd degree polynomial ($a_0 + a_1 * x + a_2 * x^2$) and corresponding minimum for Gen events.

	a_0	a_1	a_2	m_{top}
no normalisation	4390547.54588	-44426.0021316	127.642247948	174.199999984
XS normalisation	4357397.72421	-43885.9177784	126.428128287	173.400000012

Similar results have been calculated for the three considered categories of reco-level events, and they are summarised in the Figures and Tables given below. The order of both the figures and the tables is the same: first correctly matched jet combinations, then wrongly matched ones and finally the unmatched jet combinations.

The $-\ln(\mathcal{L})$ distribution for the correctly matched jet combinations, which correspond the most with generator-level events, is the only one which follows the distribution obtained for the generator-level events. The two other distributions show a significant deviation of the position of the minimum indicating an important bias introduced by the applied event selection.

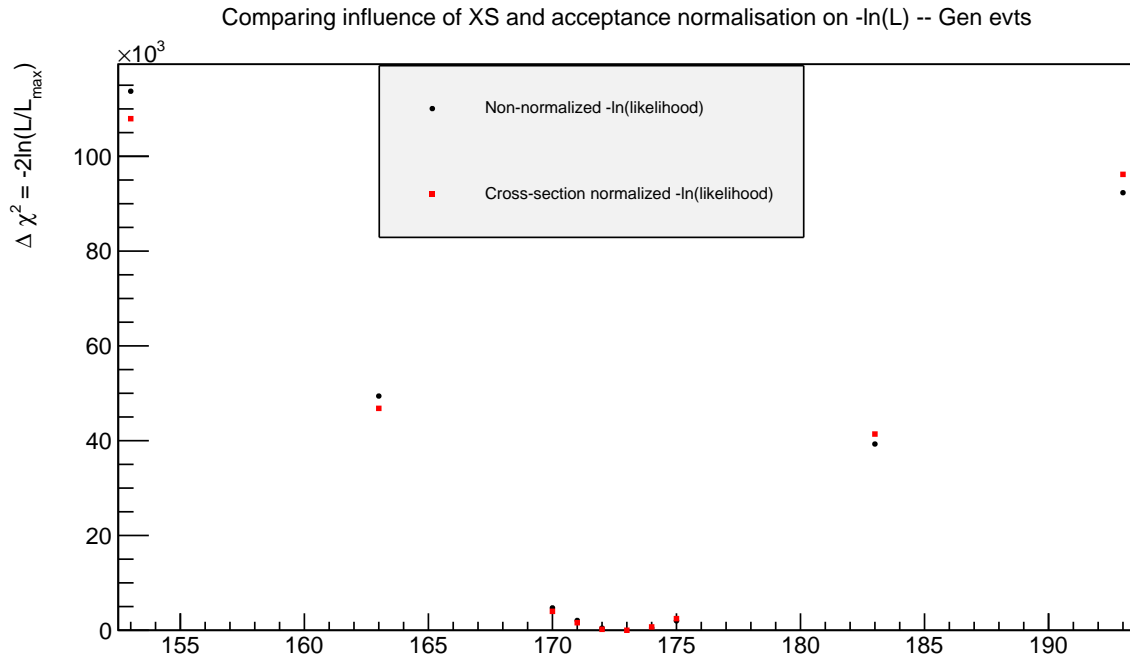


Figure 12.2: $-\ln(\mathcal{L})$ distribution for 10000 generator-level $t\bar{t}$ semi-mu (+) events. The minimum of the distribution corresponds to the correct minimum used for simulating these events, namely 172.5.

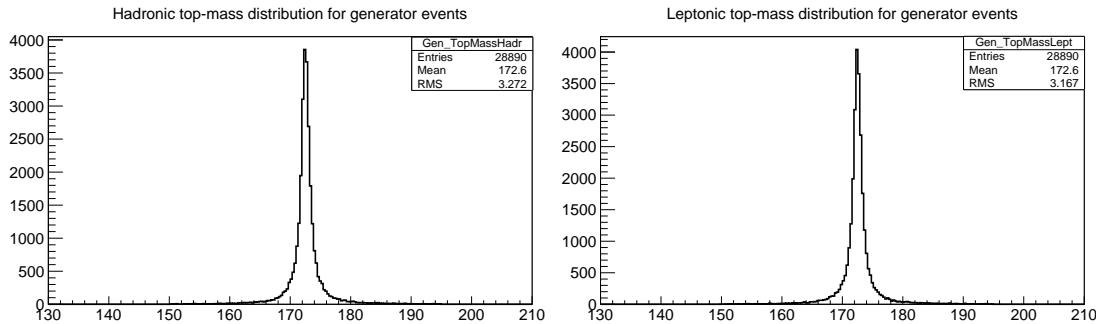


Figure 12.3: Distributions for the hadronically (left) and leptonically (right) decaying top quark for generator-level events.

Table 12.4: Fit parameters of 2nd degree polynomial ($a_0 + a_1 * x + a_2 * x^2$) and corresponding minimum for CorrectReco events.

	a_0	a_1	a_2	m_{top}
no normalisation	2231296.75883	-19063.0863774	54.4843673637	175.0999999986
XS normalisation	2198831.67235	-18531.2718603	53.2936154243	173.8399999993
Acc normalisation	2127835.59494	-18006.1769325	52.1206777931	172.5800000005

Comparing the different m_{top} measurements for each of the categories and for the different normalisations applied clearly shows that applying both the cross-section normalisation and the acceptance normalisation significantly improves the measurement of the top-quark mass and brings it closer to the expected value.

Current results are given without uncertainties.

Table 12.5: Fit parameters of 2nd degree polynomial ($a_0 + a_1 * x + a_2 * x^2$) and corresponding minimum for WrongReco events.

	a_0	a_1	a_2	m_{top}
no normalisation	1430120.89175	-9693.4402167	26.7893587541	180.9999999991
XS normalisation	1400565.78862	-9209.34336566	25.7054394299	179.0000000001
Acc normalisation	1335938.33746	-8731.32874723	24.6376683024	177.0000000004

Table 12.6: Fit parameters of 2nd degree polynomial ($a_0 + a_1 * x + a_2 * x^2$) and corresponding minimum for UnmatchedReco events.

	a_0	a_1	a_2	m_{top}
no normalisation	1246891.66214	-8364.64777064	22.579725034	185.399999984
XS normalisation	1222399.17029	-7963.32843204	21.6813673937	183.79999998
Acc normalisation	1168822.11268	-7567.24056311	20.7969519086	181.8000000013

12.2.1 Improvement of top-quark mass measurement by applying cuts on $-\ln(\mathcal{L})$

In order to reduce the influence of the event selection on the top-quark mass measurement using a Matrix Element Method, MadWeight, the effect of applying a cut on the obtained $-\ln(\mathcal{L})$ has been studied. For this only the events for which the $-\ln(\mathcal{L})$ has a negative second derivative, and hence behaves as a parabola with a minimum in the range of interest, have been used to perform the top-quark mass measurement.

The results of this study are summarized in Tables 12.7 and 12.8, first the efficiency of this cut has been given by showing the percentage of remaining events after applying this cut on the different categories. The second table shows the obtained top-quark mass measurement after requiring one or both of the second derivatives to be positive.

For the calculation of this second derivative 5 different points have been studied with the middle point the expected SM value. Hence a distinction can be made whether the second derivative of the inner three points, the second derivative of the two outer ones with the middle point or both of the two should be positive. This distinction, and their respective influence, can be retrieved in Table 12.8 where the categories have been named *Inner*, *Outer* and *Both*, respectively.

Table 12.7: Percentage of remaining events for the four considered categories and three possible second derivative requirements. The numbers given here have been found by applying the above-mentioned cut on the $-\ln(\mathcal{L})$ obtained by running MadWeight on 10000 $t\bar{t}$ semi-mu (+) events. The number of successfully calculated events by MadWeight have been given before in Table 12.2.

	Events remaining after requiring 2 nd derivative > 0		
	Inner (%)	Outer (%)	Both (%)
Generator level	89.87	94.75	88.91
Reco-level, correctly matched	84.32	75.22	71.27
Reco-level, wrongly matched	73.31	67.58	59.87
Reco-level, unmatched	70.60	66.40	57.38

Table 12.8: Measured top-quark mass for the four considered categories and the three possible second derivative requirements compared to the mass measured originally and documented in Tables 12.3 - 12.6.

	Original m_{top}	m_{top} after requiring 2 nd derivative > 0		
		Inner (GeV)	Outer (GeV)	Both (GeV)
Generator level	173.40	172.73	172.77	172.72
Reco-level, correctly matched	172.58	172.69	172.92	172.86
Reco-level, wrongly matched	177.00	173.24	173.07	173.08
Reco-level, unmatched	181.80	173.55	173.26	173.27

Table 12.8 clearly indicates the large improvement which can be gained when applying a requirement on the sign of the second derivative of the $-\ln(\mathcal{L})$. The difference between the three cut options is almost negligible, but the influence of applying a restriction on the sign of the second derivative significantly approaches the measured top-quark mass to the one used for the simulation.

However since the efficiency of the three different cut options, shown in Table 12.7, clearly differs a lot the optimal cut is on the inner second derivative. Hence using the mass-points 172, 173 and 174 GeV.

However this conclusion only holds in the case of the top-quark mass measurement and will have to be revised for the measurement of the anomalous couplings. The main message which should be kept from this study is the fact that a clear and important improvement can be obtained when applying a cut on the $-\ln(\mathcal{L})$ distribution. Using the case of the top-quark mass measurement, which was already quite decent without applying any cut, indicated that the considered method can be trusted and behaves as expected.

Only point which should still be considered (and which is probably more important for RVR measurement) is how the outer points are distributed with respect to the inner five points which are used for the fit ... This to have an idea whether the cut requirement results in weird-shaped events (and in the case of RVR now a reversed Mexican hat shape for example ...)

12.3 Measurement of right-handed vector coupling, V_R , using Matrix Element Method

Now that the method and the influence of the event selection has been, partially, understood by first studying the measurement of the top-quark mass, the Matrix Element Technique can be applied on the right-handed vector coupling.

Again the measurement has been done in a similar way and has been repeated for generator-level events and for correctly, wrongly and unmatched jet combinations of reco-level events.

12.3. MEASUREMENT OF RIGHT-HANDED VECTOR COUPLING, V_R , USING MATRIX ELEMENTS

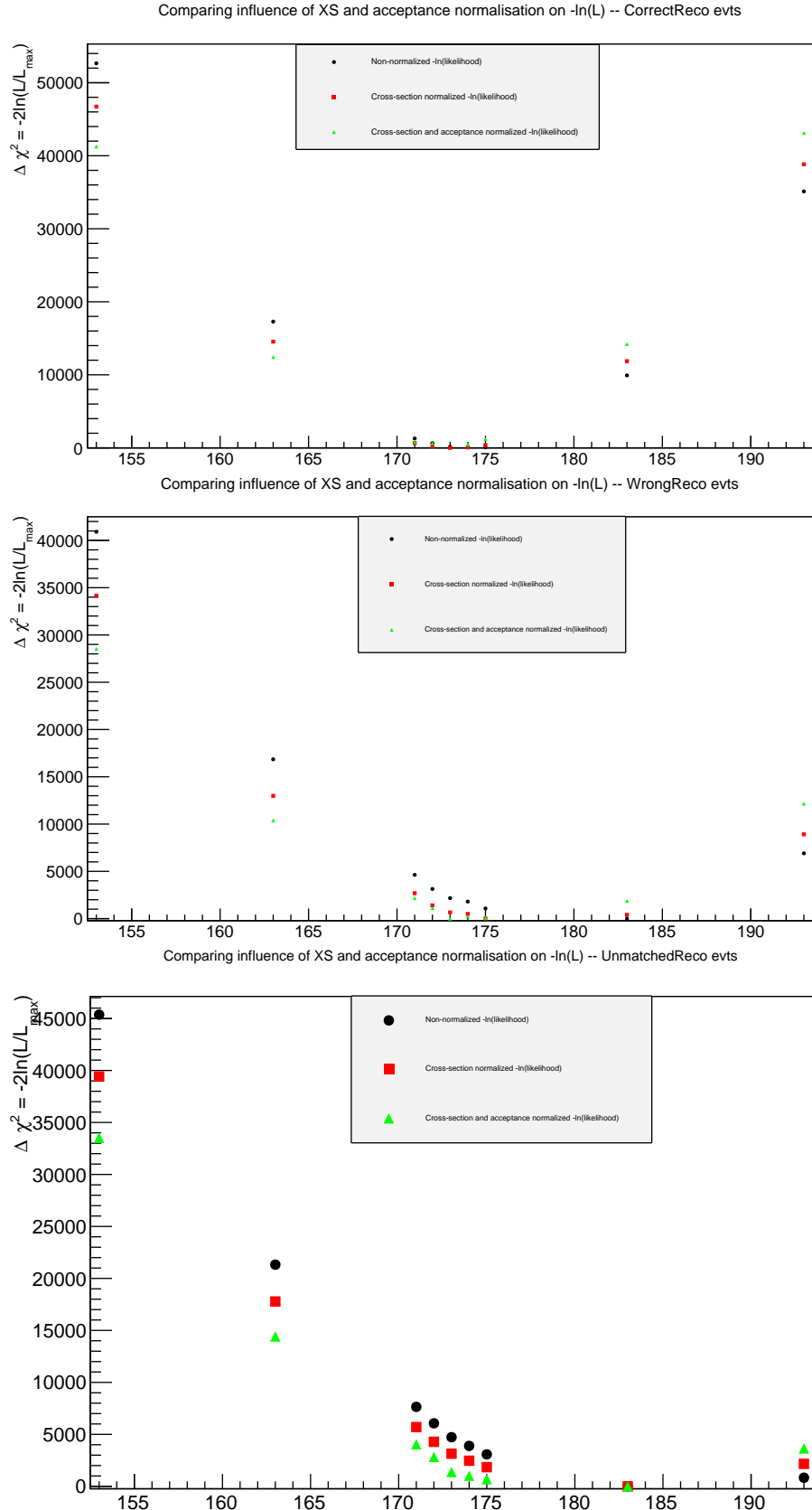


Figure 12.4: $-\ln(\mathcal{L})$ distributions for 10000 reco-level $t\bar{t}$ semi-mu (+) events, respectively correctly matched, wrongly matched and unmatched jet combinations. The position of the minimum for the correctly matched jet combinations still corresponds with the value used for simulating these events, while the wrongly matched or unmatched jet combinations significantly distort the agreement with the expected minimum position.

Chapter 13

Likelihood event selection

13.1 Issue: Change of VR not found in likelihood shape

First test configuration:

MadGraph sample created with $Re(V_R) = + 0.08$

⇒ Should result in a minimum around +0.08 when looking at summed likelihood!

But obtained result is not as expected ...

Distributions given below are the total -ln(likelihood) when no cuts are applied, when only χ^2 -cut is applied and when the χ^2 -cut is combined with requiring the slope of the polynomial fit to be positive.

For each of the cases this result is obtained by first fitting all the 21 points with a 2nd degree polynomial, removing the 7 points which are the farthest away from this fit distribution and then fitting again the remaining 14 points with another 2nd degree polynomial.

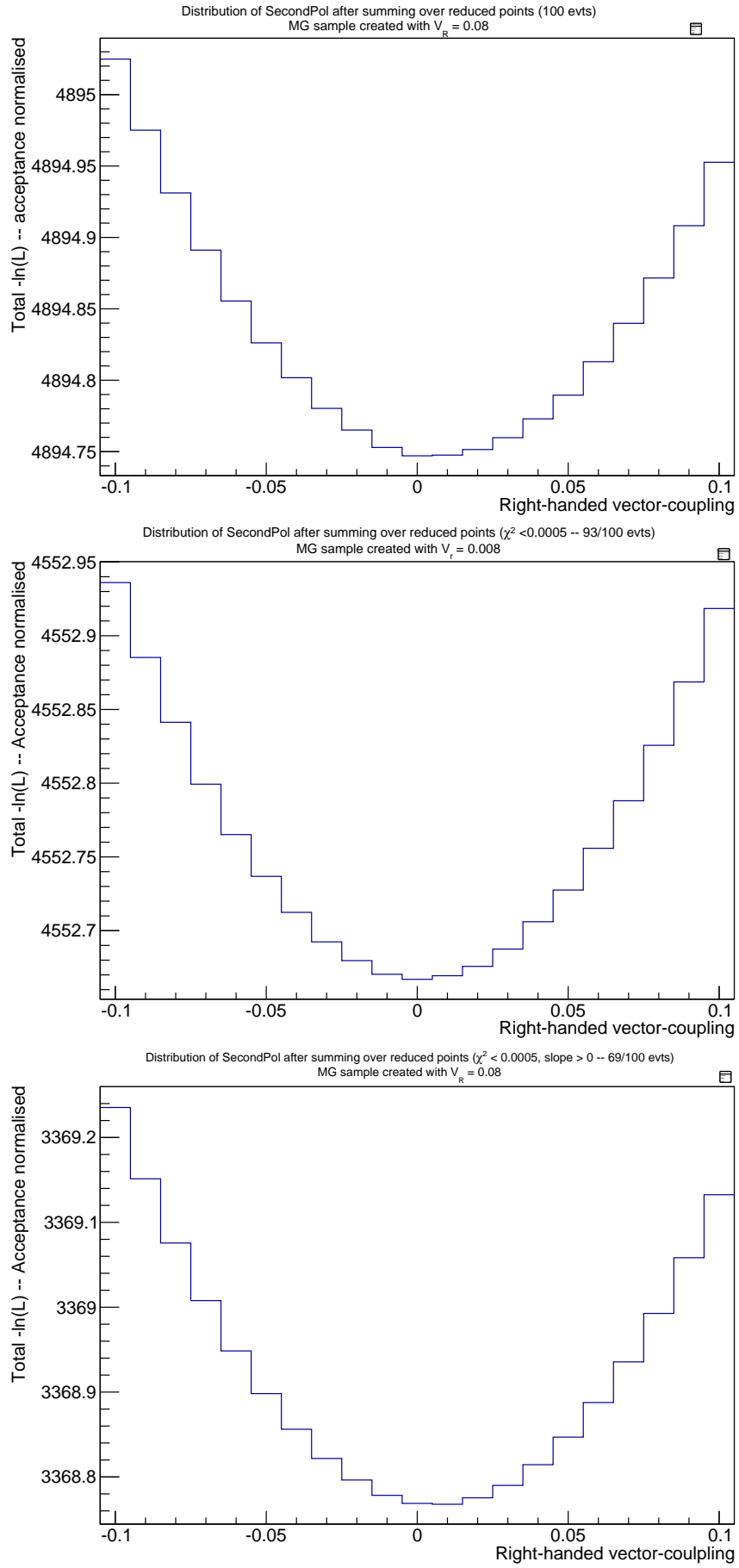
The overall -ln(likelihood) distribution is obtained by summing all the separate -ln(L) fit distributions.

The cuts which are applied always use the χ^2 or the slope of this second fit.

Remark: Low statistics ..

For the moment the statistics is still rather low, because my MadWeight calculation for the full 10000 events crashed yesterday.

They are currently still running and should be finished later today.



So in order to make sure whether this unexpected position of the minimum was caused by the created ROOT macros I decided to repeat this test also for the top mass. If the position of the minimum would correspond with the top mass used for creating the MadGraph sample, the VR-issue above is not caused by the used ROOT macros ...

As expected for the top mass all results look as expected. However since the top mass can be measured much more precisely the influence of the cuts on the $-\ln(\text{likelihood})$ are less significant. The $-\ln(L)$ distribution without any cut applied already results in the correct position of the minimum ..

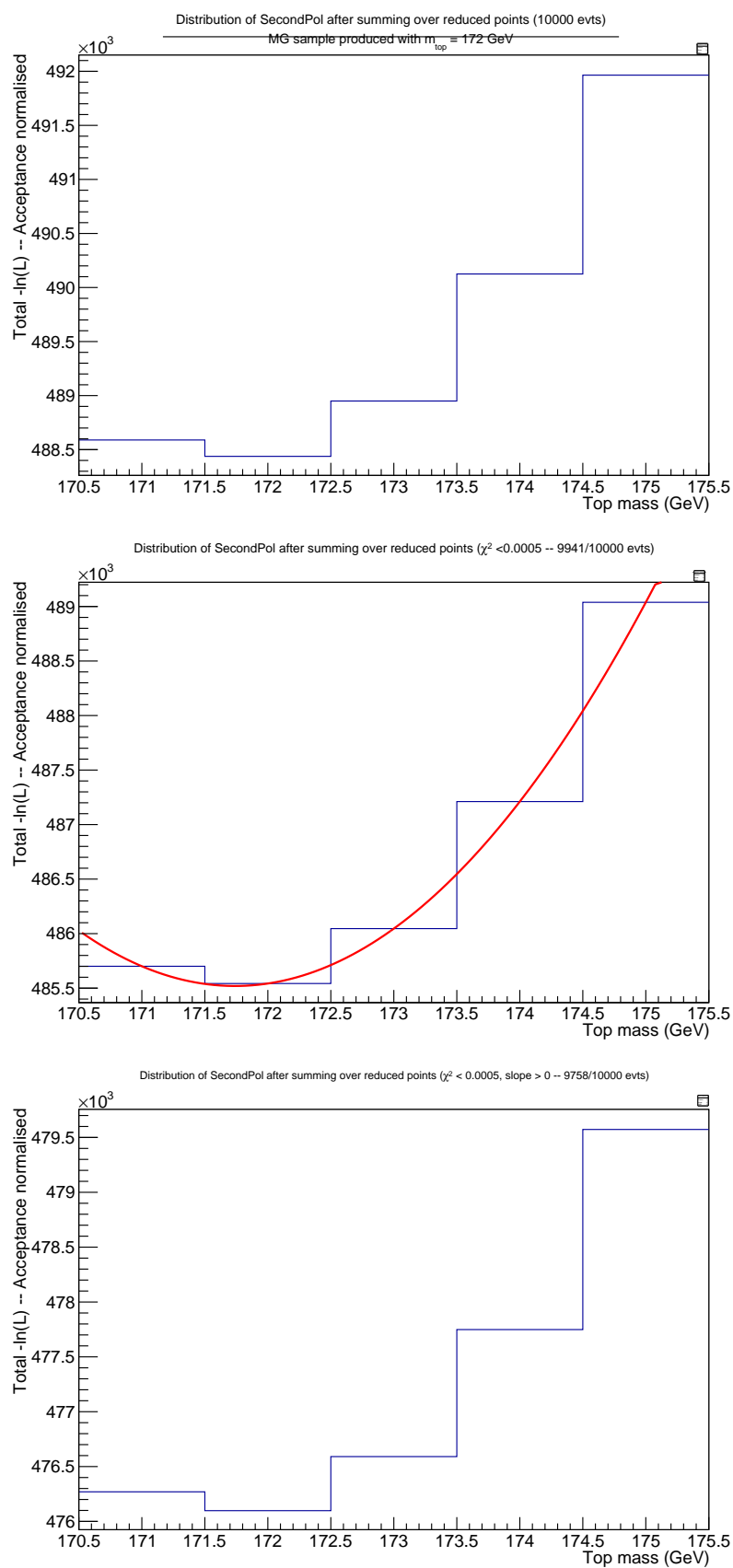
Here only 5 points have been used (mainly for speeding up MadWeight CPU time) so only 1 point is removed before the second fit is applied.

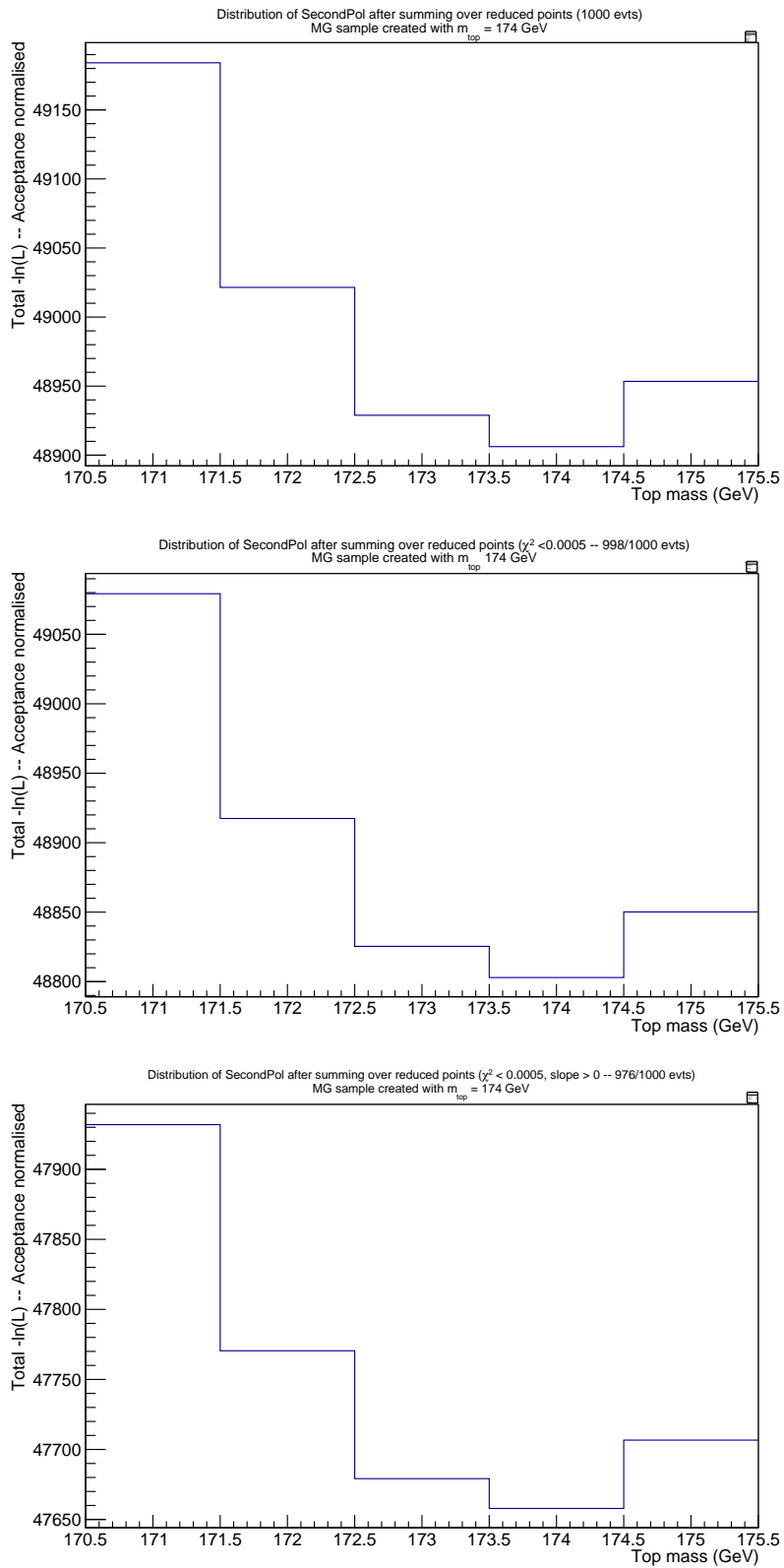
The first three distributions correspond to the MadGraph sample created with $m_{top} = 172 \text{ GeV}$ while the second one was created with $m_{top} = 174 \text{ GeV}$.

Search for VR-issue

Now that the control check using the top mass MadGraph samples indicated that the created ROOT macros and the consecutive fitting procedure does work as should be, I will continue to investigate why this is not the case for the anomalous couplings.

Maybe the use of more statistics can help but I found it rather strange that with reduced statistics the position of the minimum is nicely positioned around 0. Maybe the change of VR-component was not translated into the produced MadGraph sample, this I will check by creating some MadAnalysis plots which easily compares the kinematic information of different MadGraph samples.





Chapter 14

Obtained result after applying double fit

In order to overcome the influence of the few configuration points which destroy the shape of the likelihood distribution, it had been decided to apply a double-fit procedure in order to extract the measured anomalous coupling coefficient. This double fit procedure will be similar for both the V_R and g_R coefficient, however the symmetry in V_R^2 implies that for this coefficient a 4th order polynomial should be applied while for g_R a 2nd degree polynomial is sufficient.

The double-fit procedure is the following, defined on an event-by-event basis, and follows the following structure:

1. The first fit is applied onto all the considered configuration points which have been calculated by MadWeight.
2. For each configuration point which has been used in the first fit, the deviation between the fit distribution and the actual MadWeight measurement is calculated and compared against all other configuration points. Depending on the original number of configuration points considered, a specific number of points with the highest fit deviation is excluded as input for the following fit.
3. Once these points have been identified a second, completely identical for the rest, fit is applied onto the remaining configuration points. This second fit is then used as the final fit from which the V_R and g_R coefficients will be extracted.

The main benefit of such a double-fit approach is that the dependence with respect to a couple of deviating configuration points can easily be avoided by simply excluding them from the final fit. This will definitely help to make sure that the shape of the final fit corresponds the best with the actual likelihood shape and ensures that the distribution used for the coefficient measurement is not influenced by statistical fluctuations or erroneous MadWeight calculations. It is therefore important to exclude this type of configuration points since it is not advisable that the extracted measurements are sensitive to possible phase-space issues occurring during the MadWeight calculation step.

Another important advantage of applying a double-fit on an event-by-event basis is that the likelihood distribution for each event is replaced by a smooth 2nd or 4th order polynomial. The fact that a double-fit method is used even ensures that the χ^2 value and other

characteristics make sense because the x worst points have been removed from the fitted range. Hence it is possible, in the case of the 2nd order polynomial, to put a constraint on the slope of the likelihood shape by using the corresponding fit. Also cutting on the χ^2 value can help to select events for which a lot of events deviate from the proposed polynomial shape and not just contain two or three completely “crazy” events.

The obtained improvement of the χ^2 variable between the first and second fit is shown in Figure 14.1. This corresponds to a simulated generator-level sample created by MadGraph using a different anomalous couplings coefficient than originally included in the Standard Model. Hence as expected, even the χ^2 distribution of the first fit is rather smooth and exhibits a nice peak around very low values. Still a clear improvement is visible when applying the second fit on a limited range.

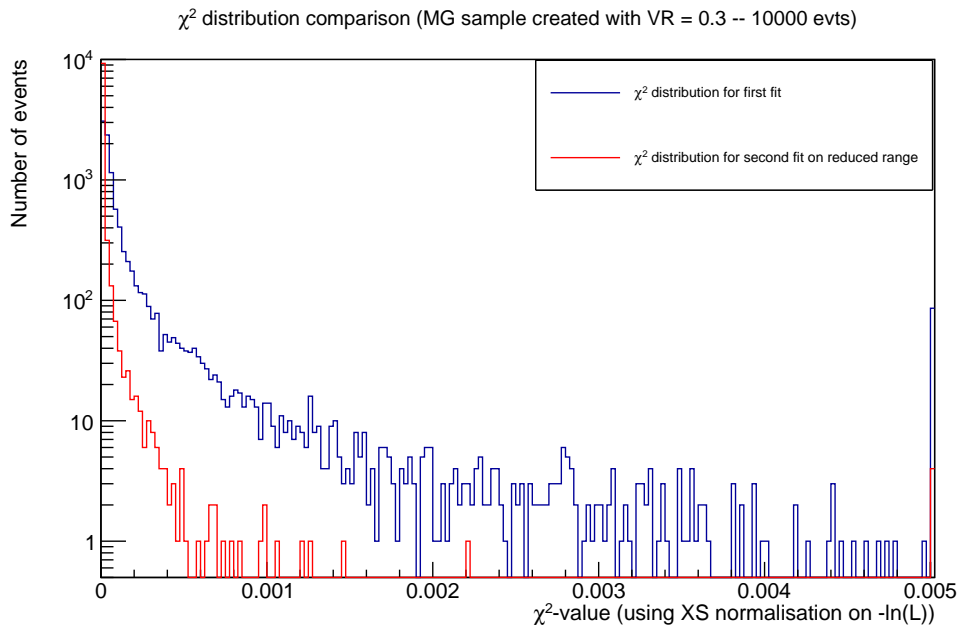


Figure 14.1: Obtained χ^2 distribution when applying the first fit (blue) and when applying the second fit on the reduced number of configuration points (red).

In order to select the optimal χ^2 constraint that should be applied a comparison of the χ^2 distribution for generator-level, signal reco and background reco events. Studying the overall $\ln(\mathcal{L})$ distribution for different χ^2 cuts indicated that cutting too tight might result in an altered shape in a rather negative way. So it seems that restricting the event selection too much actually has the opposite effect on the overall $\ln(\mathcal{L})$ distribution, probably because the power of MadWeight lies in the fact that the integrated phase space gets flattened out by considering multiple events. Comparing the individual MadWeight weight distributions on an event-by-event level clearly indicates that quite a lot of variation can be found in the shape, even in the case of the well-measured m_{top} . But again here the overall $\ln(\mathcal{L})$ shows a nice minimum almost at the expected position indicating again that MadWeight output should not be taken too serious for one single event. A couple of these type of event comparisons between the original MadWeight calculations and the second polynomial fit are given in Figure 14.2.

For the moment three different χ^2 constraints have been studied, which should possibly be good enough to be applied for both gen-level events as reco-level events. In

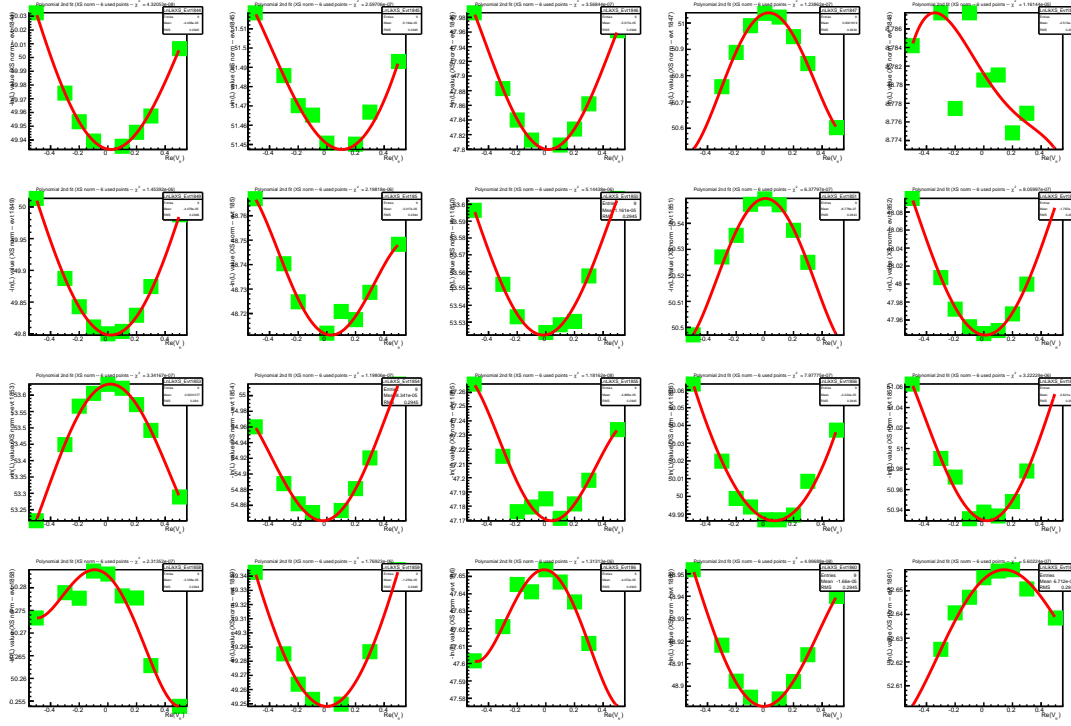


Figure 14.2: Overview of the MadWeight output for 25 different, but consecutive, events fitted with the second f^{th} order polynomial. The used sample is a MadGraph sample created with $V_R = 0.3$.

the following table, Table 14.1, the number of selected events for the different χ^2 -cuts considered are listed for as much as possible generator- and reco-level samples.

Table 14.1: Number of selected events after applying the different χ^2 -cuts considered.

Sample	$\chi^2 < 0.001$	$\chi^2 < 0.0005$	$\chi^2 < 0.0002$
MG with $V_R = 0.3$ in $[-0.5, -0.3, -0.2, \dots, 0.3, 0.5]$	99.91 %	99.78 %	99.02 %
MG with $V_R = -0.1$ in $[-0.3, -0.275, \dots, 0.3]$	94.74 %	90.30 %	80.89 %
MG with $V_R = -0.08$ in $[-0.1, -0.09, \dots, 0.1]$	96.99 %	93.85 %	87.26 %
MG SM in $[-0.5, -0.3, -0.2, \dots, 0.3, 0.5]$	99.82 %	99.62 %	98.89 %
Gen in $[-0.5, -0.3, -0.2, \dots, 0.3, 0.5]$	97.35 %	95.82 %	92.63 %
Correct reco in $[-0.5, -0.3, -0.2, \dots, 0.3, 0.5]$	93.57 %	90.58 %	85.75 %
Wrong reco in $[-0.5, -0.3, -0.2, \dots, 0.3, 0.5]$	77.91 %	72.55 %	64.95 %

The improvement obtained when applying the χ^2 cuts on the final $\ln(\mathcal{L})$ distributions can be understood from the shape comparisons given in Figure 14.3, which show the original $\ln(\mathcal{L})$ distribution and the distribution of the events remaining after applying the specific χ^2 cuts.

Strangely enough can be concluded from these distributions that applying the χ^2 cuts especially improves the bias in the case of the reco-level events. The middle-left histogram shows the influence on the $\ln(\mathcal{L})$ in the case of generator-level events and for these type of events the χ^2 cuts almost do not alter the position of the minimum. Maybe this observation can be explained by the much lower χ^2 values of the fit in the generator-level case such that requiring $\chi^2 < 0.0005$ does not have the same influence on the shape. In

order to be sure about this, maybe an additional χ^2 cut of, for example 0.00005 can be applied in order to ensure that some influence can be seen on the overall $\ln(\mathcal{L})$ shape.

Update: The middle-right histogram now contains almost the same distributions, but the χ^2 -cut of 0.0005 has been replaced by 0.00005 in order to double-check whether applying a χ^2 cut also influences or improves the generator-level distributions. The obtained result is rather positive, since the blue distribution in this case nicely corresponds to a minimum around $V_R = 0.0$ as suggested by the Standard Model! The corresponding percentages for this χ^2 cut is given in the Table 14.2.

Table 14.2: Number of selected events after applying the different χ^2 -cuts considered. Here the tighter χ^2 -cuts have been applied which are only useful for generator-level events.

Sample	$\chi^2 < 0.001$	$\chi^2 < 0.0002$	$\chi^2 < 0.00005$
Gen in $[-0.5, -0.3, -0.2, \dots, 0.3, 0.5]$	97.35 %	92.63 %	85.66 %
MG SM in $[-0.5, -0.3, -0.2, \dots, 0.3, 0.5]$	99.82 %	98.89 %	95.77 %

A second strange, and even slightly worrisome, observation concerns the two upper distributions. These contain the likelihood distributions obtained for two MadGraph samples, both created separately using the Standard Model configuration. Hence they should definitely correspond to a minimum around $V_R = 0.0$ since they are not even influenced by event selection or reconstruction effects ... In order to be completely sure that the first obtained result was created with a correct MG sample, a second one was created but as can be seen by comparing the right and left figure, they are clearly identical. Both of them correspond to a minimum at around $V_R = -0.2$. How this is possible, especially when the generator-level distribution does correspond with the predicted Standard Model value, is not really understood. Even the tighter χ^2 cut which is applied in the right distribution does not solve the issue of the positioning of the minimum.

As a sort of consistency check which will be performed is comparing these two distributions with the result obtained when looking at a MG sample created with $V_R = 0.05$.

14.1 Double-check of method using g_R coefficient

In order to compare the correctness of the method, the same results can also be studied for the g_R coefficient. In the best case looking at this anomalous couplings coefficient can give a possible explanation of the incorrect position of the minimum when looking at the Standard Model MG sample. However, then should still be understood why this issue arises for the V_R coefficient. Otherwise the obtained results and distributions all have similar properties such that the double-fit method is completely double-checked and hence reliable to be used for analysing actual data events.

One of the most important differences between measuring the V_R coefficient and the g_R coefficient is the fit function which has to be applied. As said before the g_R coefficient is not supposed to be symmetric around 0 implying that a quadratic function is sufficient for correctly measuring the anomalous coupling coefficient. Another important difference between the two coefficients is the sensitivity at low values, which is much higher in the g_R case than in the V_R case. This should normally imply that the g_R coefficient can be studied in a narrower range than the V_R one without introducing statistical fluctuations. The reason for this different sensitivity follows directly from the theoretical equations and

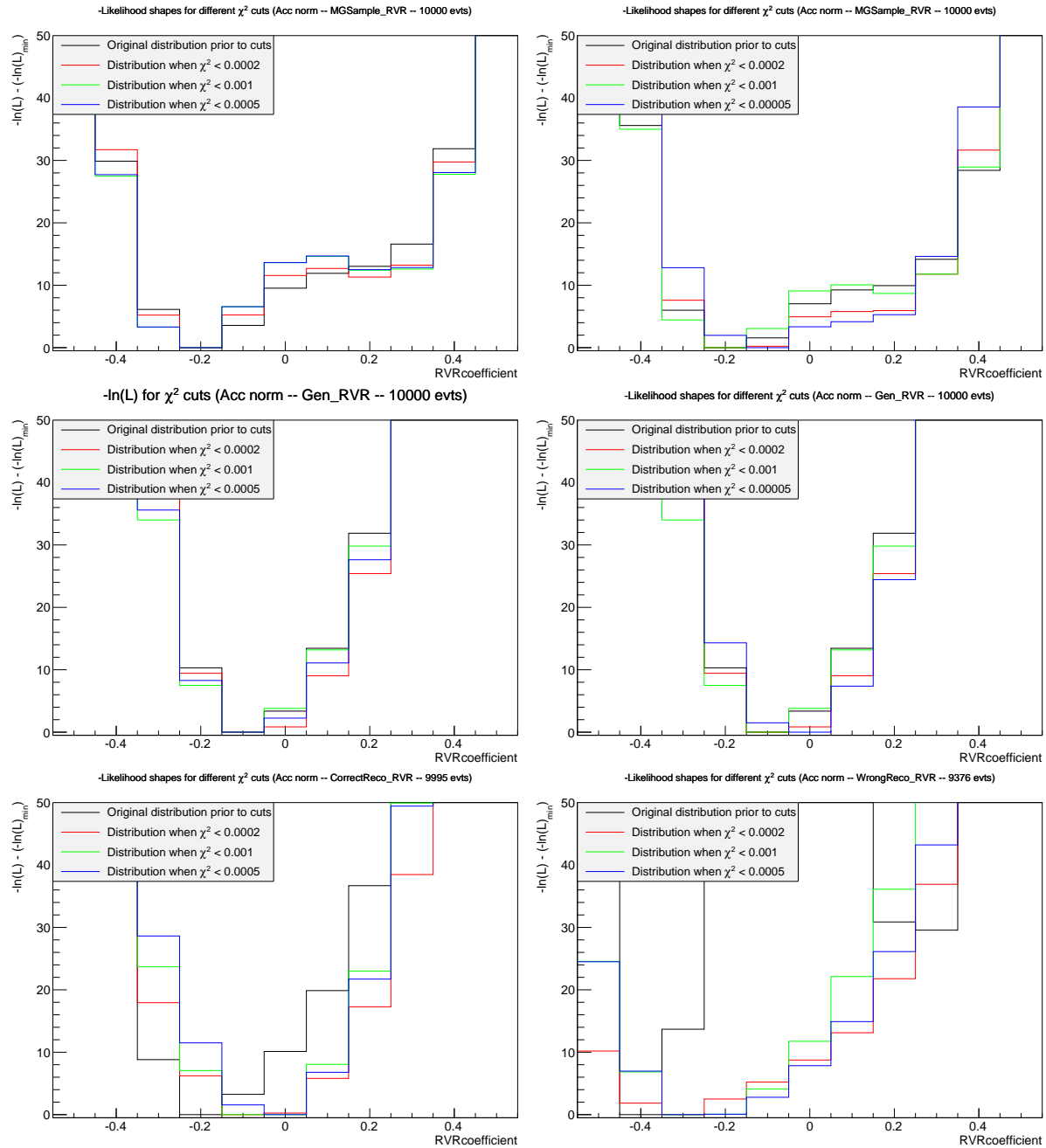


Figure 14.3: Influence of the different χ^2 cuts on the overall $\ln(\mathcal{L})$ distribution.

is depicted in Figure 14.4, which contains the shape influence on the $\cos\theta^*$ distribution when considering the same range.

The range which will be used for the two anomalous coupling coefficient can easily be motivated by looking at these distributions, see Table 14.3. However from the variation of the $\cos\theta^*$ distribution can be expected that even in the more narrow range used for the g_R coefficient, the measurements will still be more sensitive since the variations here are still larger than in the range for the V_R coefficient. But it is not wise to consider an even wider range for the V_R measurement since the uncertainty on the likelihood distribution is so small, in general less than 0.1 fluctuation on V_R is retrieved, that the 5σ interval will not be visible anymore. Hence it can be concluded that the range given in the table can be somewhat seen as the minimum range for which fluctuations of the V_R coefficient

should be detectable. Considering a smaller range will result in a shape dominated by statistical fluctuations since the kinematics cannot be differentiated between the different coefficients calculated.

Table 14.3: Range which will be used for the two anomalous coupling coefficient considered here.

coefficient	Range
V_R	[−0.5, −0.3, −0.2, −0.1, 0.0, 0.1, 0.2, 0.3, 0.5]
g_R	[−0.2, −0.15, −0.1, −0.05, 0.0, 0.05, 0.1, 0.15, 0.2]

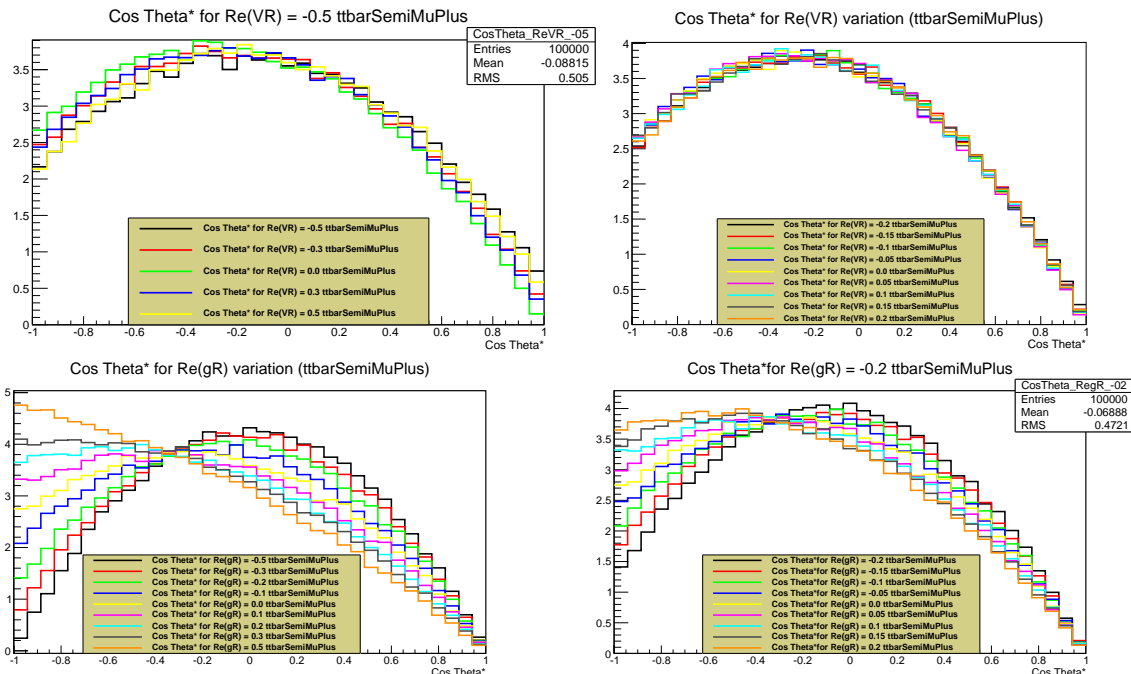


Figure 14.4: Stronger dependence of the $\cos \theta^*$ distribution on the g_R coefficient than on the V_R one. Therefore the g_R coefficient will be measured in a more narrow range than the one used for the V_R measurement.

For the moment it seems that there is an issue for the g_R measurement when the acceptance normalisation is applied. As can be seen from Figure 14.5, the χ^2 distribution is completely wrong when going from the XS-normalisation to the acceptance-normalisation distribution. Looking at the individual distributions for both normalisation cases also shows that something strange is happening. Strangely enough the overall $\ln(\mathcal{L})$ distribution obtained from the double-fit procedure still seems pretty decent when no χ^2 -cut is applied, which seems to suggest that the overall distribution should not be used without looking at the χ^2 distribution to ensure that only good fits are considered.

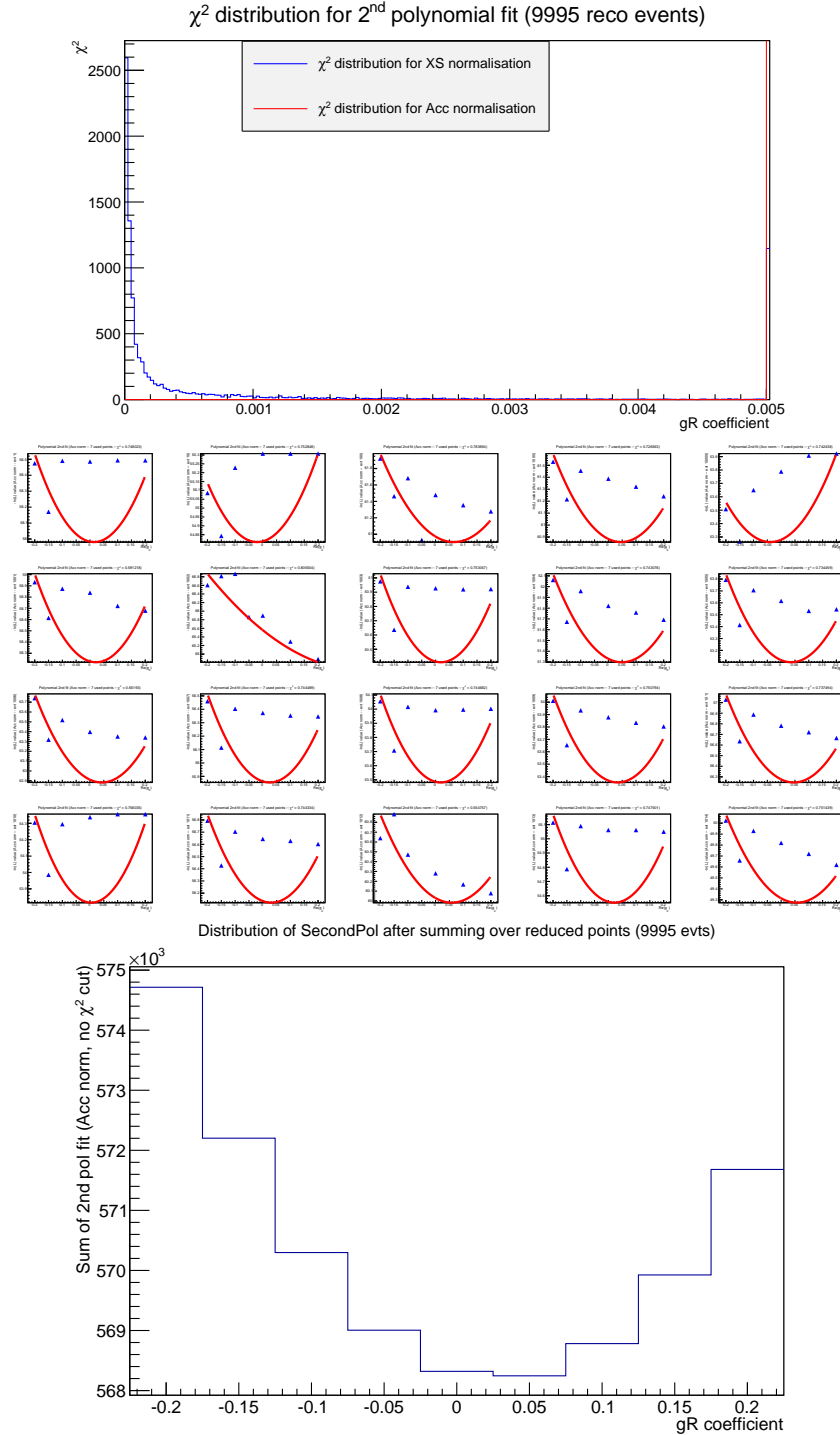


Figure 14.5: Strange behavior for χ^2 distribution when the acceptance normalisation is applied.

14.2 Bias-dependence on used V_R value MG sample

As a next check the measured V_R should be compared with the V_R coefficient used for generating the MadGraph sample. Therefore multiple MadWeight calculations should be done for each of the configurations considered in the range. It would be advisable that the bias found between the coefficient used for generating the sample and the coefficient retrieved from the measurement is independent of the value used for generating the

sample. This kind of behavior would be more difficult to understand since it implies that the bias is not perfectly linear and influenced by some other effects.

V_R coefficient	Present?	Measurement
-0.5	Yes	
-0.3	Yes	
-0.2	Yes	
-0.1	Yes	
0.0	Yes	
0.1	Yes	
0.2	No	
0.3	Yes	
0.5	No	

14.3 Influence of tighter χ^2 cuts

Chapter 15

Comparison of SM behaviour

From analyzing the result obtained after applying the double-fit procedure, it was clear that a significant discrepancy occurs between the generator-level result using the CMS Monte Carlo samples and the self-simulated MG samples. This was clearly visible in Figure 14.3 which shows the expected location of the minimum for the CMS generator-level samples but a completely wrong distribution for the MG sample created with $V_R = 0.0$. Hence from this can be concluded that the created FeynRules model does not correspond with the actual “Standard Model” of MadGraph and more investigation in the matter is necessary.

In order to be sure that the issue is caused by the created FeynRules model an additional test has been performed. For this a personal MG sample has been created using the “Standard Model” model existing in MadGraph, and also used within CMS, which was processed in the same way by MadWeight and the analysis scripts. This sample resulted in almost exactly the same distributions as was obtained using the sample created with the personally created AnomCoup model, hence a minimum differing from the expected position. The distributions for this sample are given in Figure 15.1.

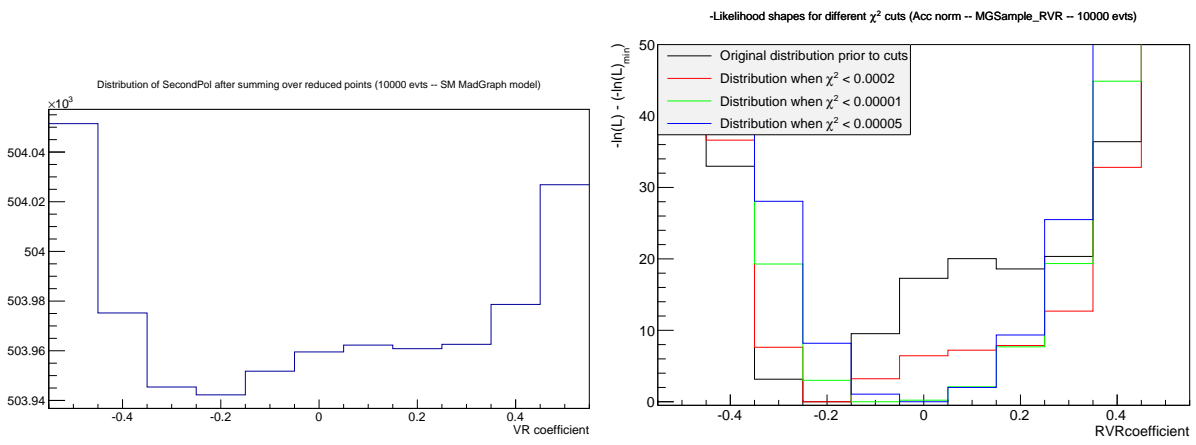


Figure 15.1: $\ln(\mathcal{L})$ distribution obtained when the MadGraph sample is created using the SM FeynRules model

However the right-handed figure shows that the application of the χ^2 cut in a very tight way, removing about 15% of the events, repositions the overall likelihood distribution to have a minimum at the correct position. This seems to suggest that in the CMS sample the few event selection cuts which have been applied probably influence the χ^2 distribution

of the fit. The percentages of event kept after applying the tighter cuts can be found in Table 15.1.

Table 15.1: Number of selected events after applying the different χ^2 -cuts considered.

Sample	$\chi^2 < 0.0002$	$\chi^2 < 0.00001$	$\chi^2 < 0.000005$
MG SM-model in $[-0.5, -0.3, -0.2, \dots, 0.3, 0.5]$	98.69 %	84.46 %	76.28 %

So as can be understood from the obtained results, there seems to be no real difference between the two different FeynRules models. This is again summarized in Figure 15.2 where some of the more important kinematic properties are shown together for the two models.

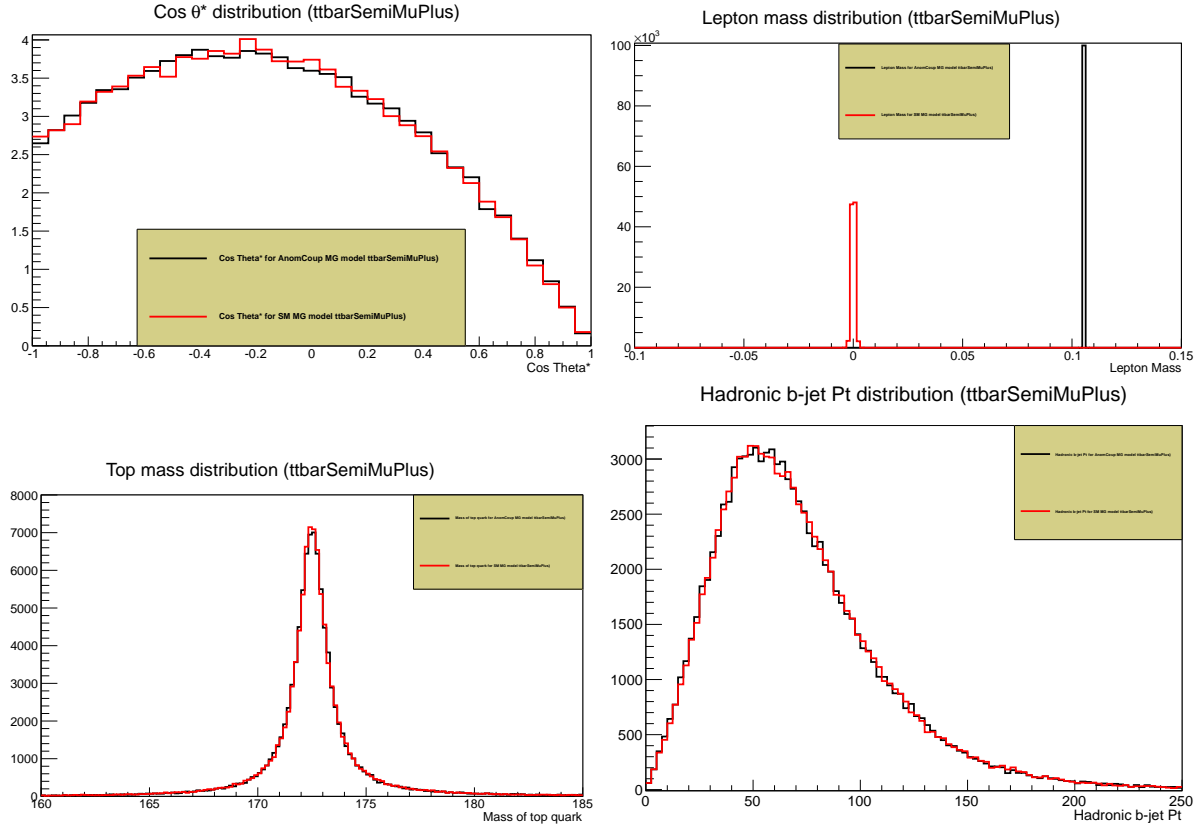


Figure 15.2: Selected distributions from the comparison between the SM FeynRules model and the AnomCoup one.

Hence it seems that the difference originates from the light pre-selection which is applied for the CMS Monte Carlo $t\bar{t}$ sample and not for the personally created MadGraph samples. Hence it should be investigated whether the influence of the event selection actually has a positive effect on the shape of the $\ln(\mathcal{L})$ distribution, and not a negative one as was thought in the beginning.

However the application of such a tight χ^2 -cut clearly improved the obtained $\ln(\mathcal{L})$ shape for the Standard Model case, it seems to worsen the result for different V_R values. The influence of the χ^2 cut on the $\ln(\mathcal{L})$ shape for two V_R values which were actually good for less tight cuts is given in Figure 15.3.

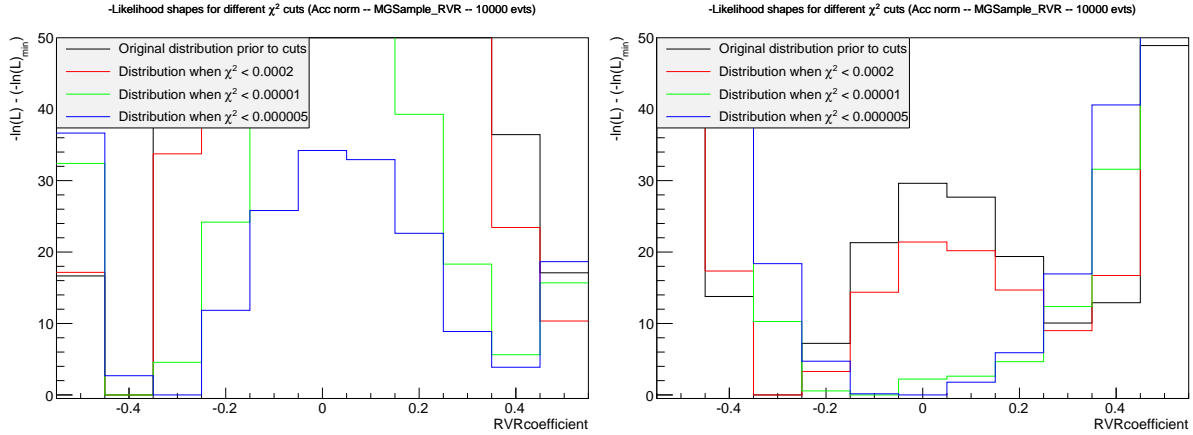


Figure 15.3: $\ln(\mathcal{L})$ distribution for two MadGraph samples which actually had a good agreement with the expected shape when looser χ^2 cuts are applied, but become completely distorted in the case of the very tight cuts. The left one corresponds to a MG sample created with $V_R = -0.5$ and the right one with $V_R = 0.3$.

So from this small study can be decided that the problem which occurs for the MadGraph generator-level events is not caused by a wrong “Standard Model” implementation but can (hopefully) be explained by the minor event selection which is applied for the CMS generator-level sample. Hence the next study will discuss the influence of the p_T -cuts on the obtained $\ln(\mathcal{L})$ distribution.

Chapter 16

Influence of generator-level event selection

A quick way to see the influence of the event selection, and avoid the submission of all samples to MadWeight, is to apply the event selection requirements after the MadWeight calculation has been performed. This implies that the event selection constraints can be applied in a similar way as the χ^2 -cut by simply using the kinematic information stored in the *.lhco* file for each individual event. The main difference with the χ^2 -cut is that the event selection should be applied prior to the double-fit procedure since this takes place in an event-by-event basis. So during this step the event selection constraints should give as additional information a “keep” or “hold” flag such that the fitting procedure is only done for the good events. The constraints which will be applied should contain the general p_T ones but also the ΔR ones should be added for example.

However at first a simplified check will be performed where only a requirement on the p_T of the different particles present in the event will be applied.

The influence of the event selection (limited to p_T -cut and χ^2 requirement) is summarised in Figures 16.1 - 16.9. These figures each contain three different $\ln(\mathcal{L})$ distributions where the left one is the result when no p_T -cut is applied, the middle when $p_T > 15$ GeV is asked and the right one requires $p_T > 30$ GeV.

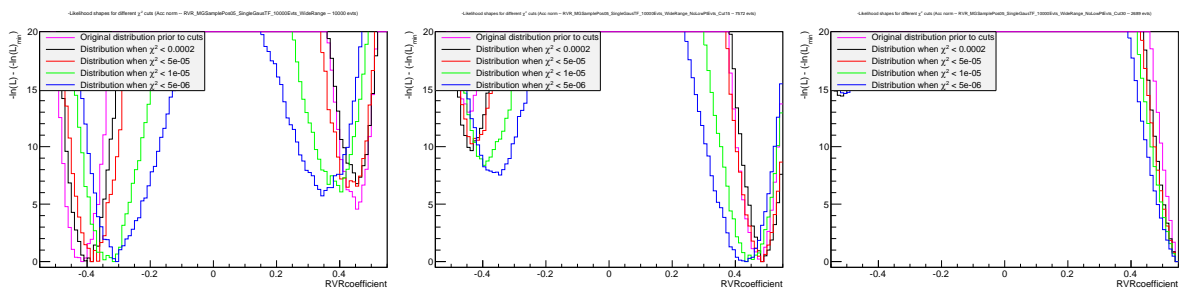


Figure 16.1: Influence of the p_T -cut on the $\ln(\mathcal{L})$ distribution for increasing p_T -cut value (0 GeV, 15 GeV and 30 GeV) for a MG sample created with $V_R = 0.5$.

From the $\ln(\mathcal{L})$ distributions given for each of the V_R configurations can easily be concluded that requiring the p_T value of the particles in the event (excluding the neutrino) does not have the desired effect. On the contrary it seems that only looking at events with high p_T broadens the 4th-order polynomial and actually converts the overall distribution into one with a maximum shape. Since the considered sample concerns generator-level

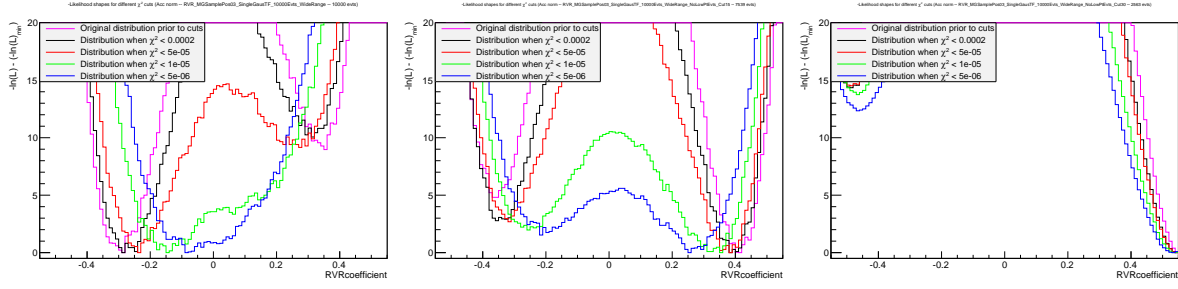


Figure 16.2: Influence of the p_T -cut on the $\ln(\mathcal{L})$ distribution for increasing p_T -cut value (0 GeV, 15 GeV and 30 GeV) for a MG sample created with $V_R = 0.3$.

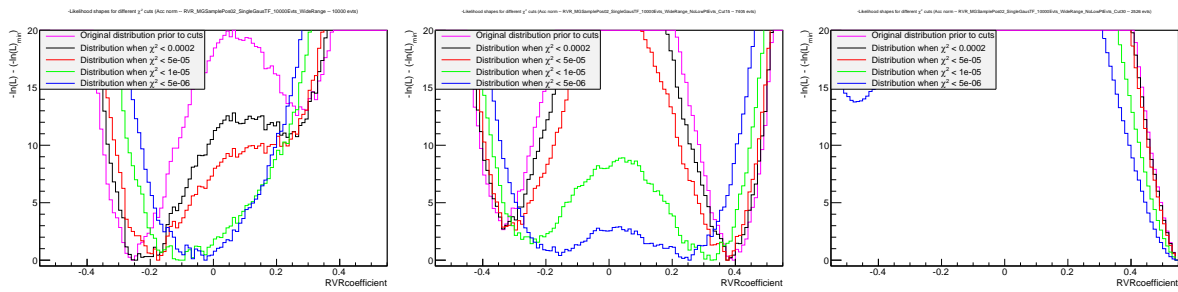


Figure 16.3: Influence of the p_T -cut on the $\ln(\mathcal{L})$ distribution for increasing p_T -cut value (0 GeV, 15 GeV and 30 GeV) for a MG sample created with $V_R = 0.2$.

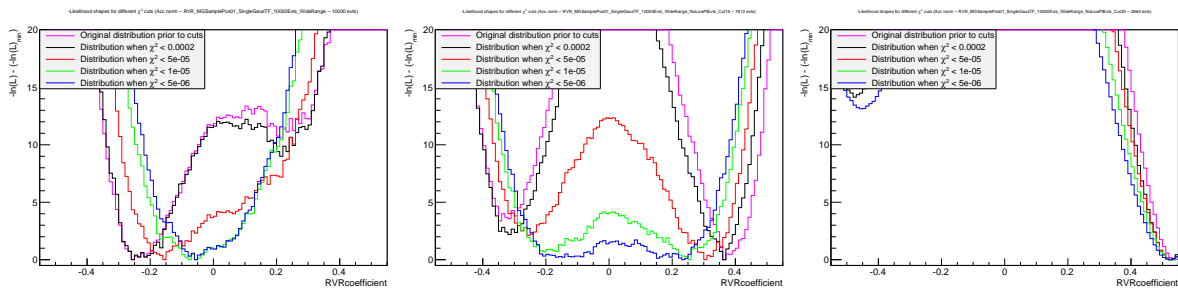


Figure 16.4: Influence of the p_T -cut on the $\ln(\mathcal{L})$ distribution for increasing p_T -cut value (0 GeV, 15 GeV and 30 GeV) for a MG sample created with $V_R = 0.1$.

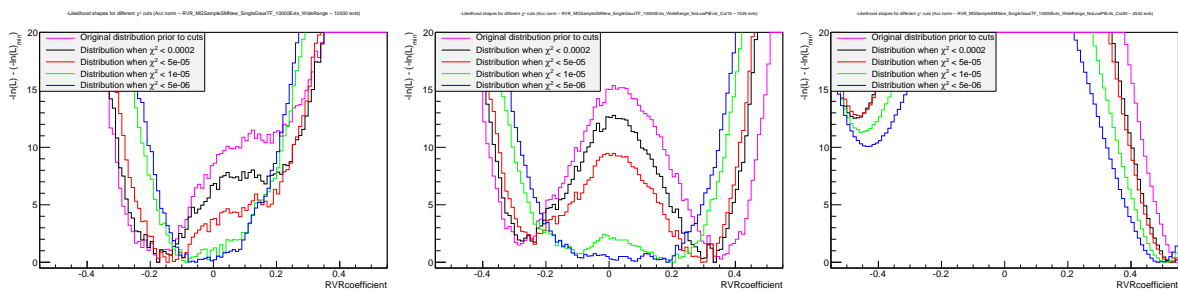


Figure 16.5: Influence of the p_T -cut on the $\ln(\mathcal{L})$ distribution for increasing p_T -cut value (0 GeV, 15 GeV and 30 GeV) for a MG sample created with $V_R = 0.0$.

event, it should be understood how the correct minimum-position can be recovered. This different options considered will be discussed in detail in the following sections.

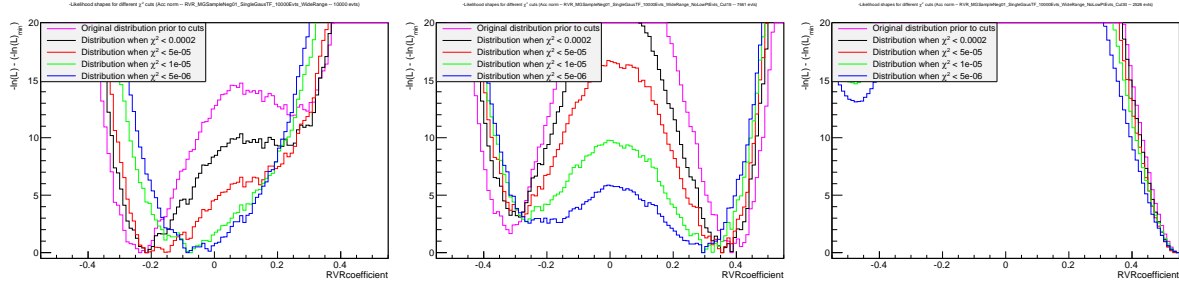


Figure 16.6: Influence of the p_T -cut on the $\ln(\mathcal{L})$ distribution for increasing p_T -cut value (0 GeV, 15 GeV and 30 GeV) for a MG sample created with $V_R = -0.1$.

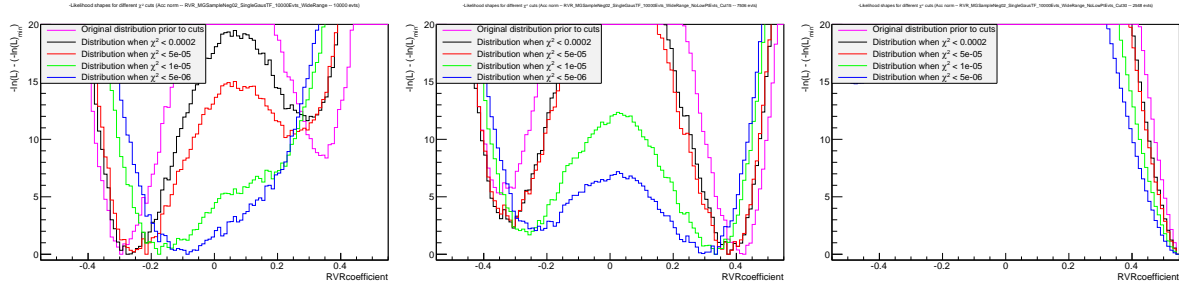


Figure 16.7: Influence of the p_T -cut on the $\ln(\mathcal{L})$ distribution for increasing p_T -cut value (0 GeV, 15 GeV and 30 GeV) for a MG sample created with $V_R = -0.2$.

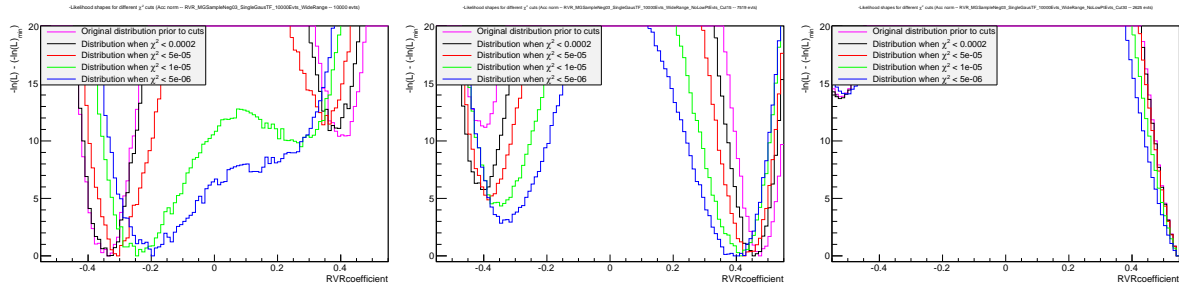


Figure 16.8: Influence of the p_T -cut on the $\ln(\mathcal{L})$ distribution for increasing p_T -cut value (0 GeV, 15 GeV and 30 GeV) for a MG sample created with $V_R = -0.3$.

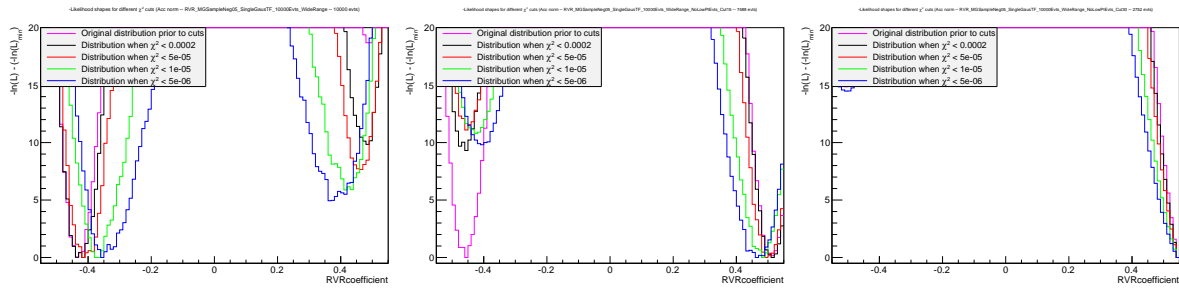


Figure 16.9: Influence of the p_T -cut on the $\ln(\mathcal{L})$ distribution for increasing p_T -cut value (0 GeV, 15 GeV and 30 GeV) for a MG sample created with $V_R = -0.5$.

16.1 Reweighting MadWeight probability using $\cos \theta^*$

As a first possible solution to the $\ln(\mathcal{L})$ distortion caused by the event selection, it was studied how the $\cos \theta^*$ normalisation could fix the issue. To apply this reweighting the

$\cos \theta^*$ distribution is calculated for each of the different V_R configurations considered in the studied range and for each of the p_T -cuts which could be applied. Then for each of the 35 bins considered in the $\cos \theta^*$ distribution the bin content of the distribution prior to the cut is divided by the one after the cut.

$$weight_i = f(\cos \theta^*) = \frac{g_{i,All}}{g_{i,Cut}} \quad (16.1)$$

where i runs over all bins of the distribution.

Hence this results in a weight for each event which is then multiplied with the MadWeight probability corresponding to this event (for each of the considered V_R configurations). The effect of this normalisation or reweighting on the $\ln(\mathcal{L})$ distributions is shown in Figure 16.10 for some V_R configurations.

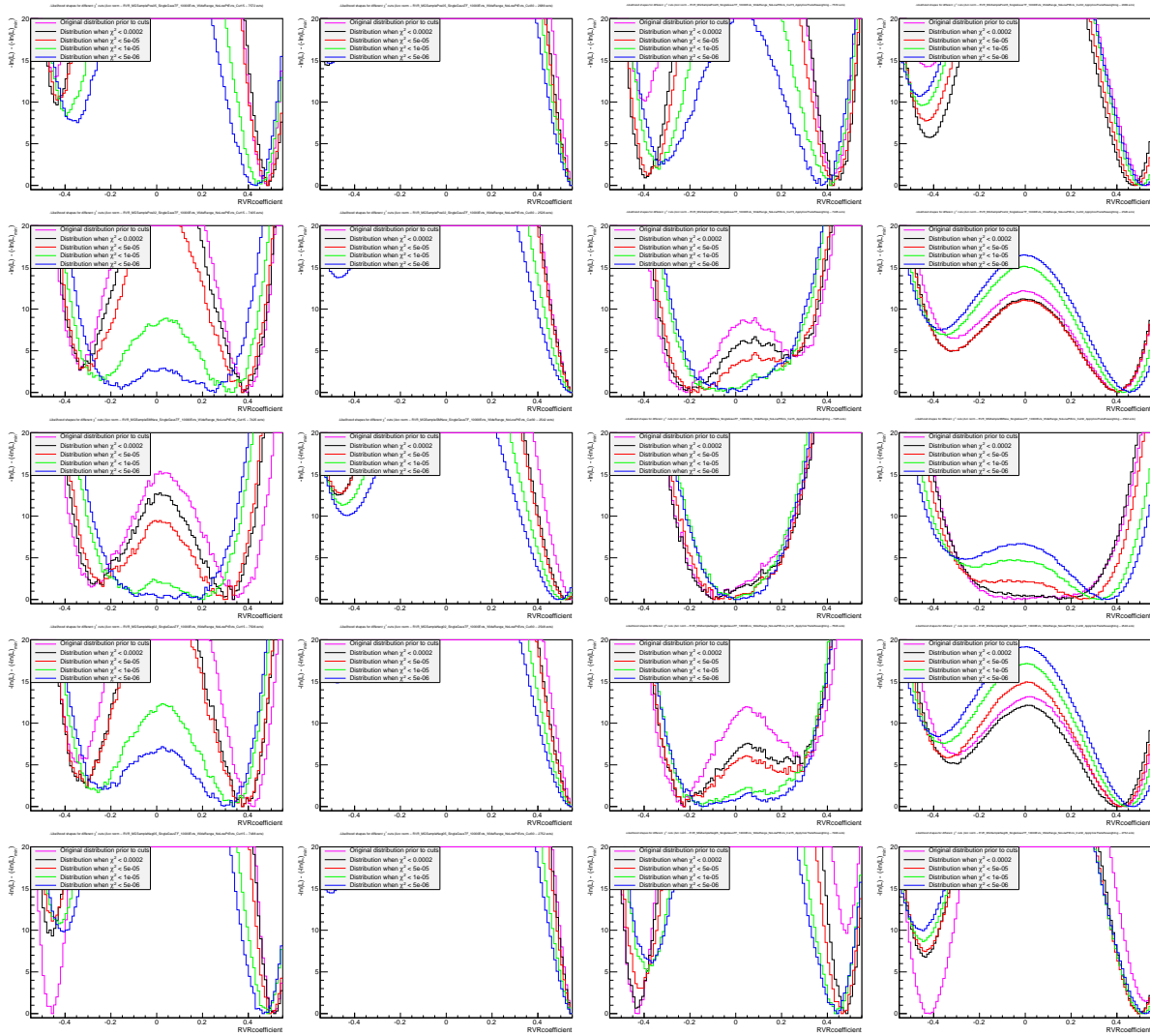


Figure 16.10: Influence of combining the $\cos \theta^*$ reweighting with the MadWeight probability on an event-by-event basis. From left to right the different plots always show the same distributions: first the 15 GeV case and 30 GeV case without this normalisation and then both with the reweighting. From top to bottom the different V_R configurations which have been shown are $-0.5, -0.2, 0.0, 0.2$ and 0.5 .

Figure 16.10 is useful for comparing the influence of this $\cos \theta^*$ reweighting in a direct

way since the original distributions can be found next, but in order to have some more detail and larger size they are also all listed in Figures 16.11 - 16.19.

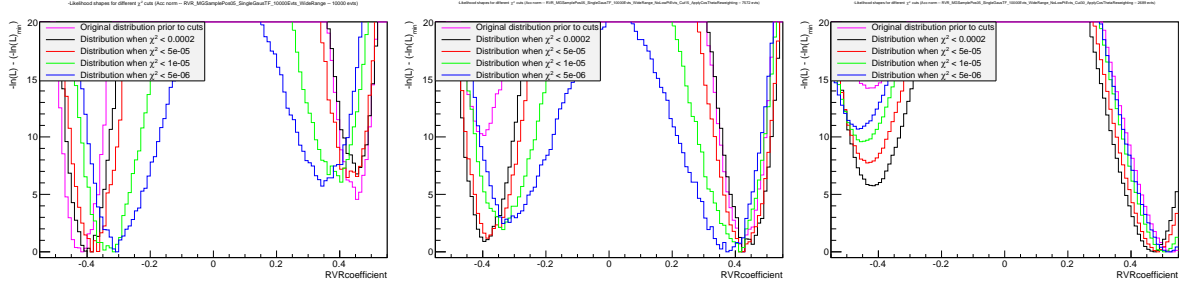


Figure 16.11: Influence of the p_T -cut on the $\ln(\mathcal{L})$ distribution for increasing p_T -cut value (0 GeV, 15 GeV and 30 GeV) for a MG sample created with $V_R = 0.5$ with $\cos \theta^*$ reweighting applied.

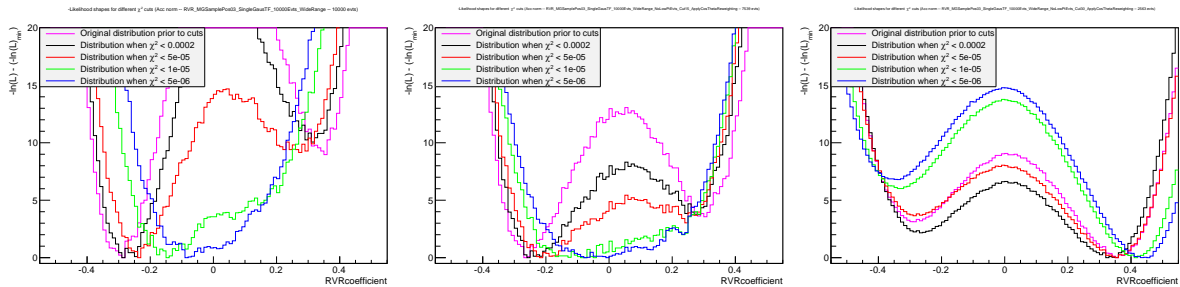


Figure 16.12: Influence of the p_T -cut on the $\ln(\mathcal{L})$ distribution for increasing p_T -cut value (0 GeV, 15 GeV and 30 GeV) for a MG sample created with $V_R = 0.3$ with $\cos \theta^*$ reweighting applied.

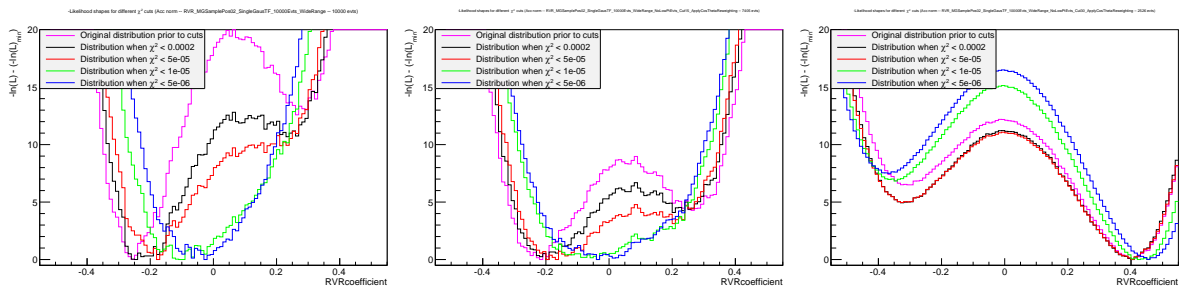


Figure 16.13: Influence of the p_T -cut on the $\ln(\mathcal{L})$ distribution for increasing p_T -cut value (0 GeV, 15 GeV and 30 GeV) for a MG sample created with $V_R = 0.2$ with $\cos \theta^*$ reweighting applied.

The $\ln(\mathcal{L})$ distributions obtained when the $\cos \theta^*$ reweighting is applied shows a significant improvement compared to the original distributions. In most of the cases the desired minimum position can almost be retrieved, however this is somewhat undone by the high p_T -cut of 30 GeV. It seems that the best agreement is found for lower p_T cuts such as 15 GeV, which is probably also closer to the preselection cleaning applied in the CMS generator-level sample. The possible bias introduced by the more realistic event selection constraints is also visible for the reco-level $t\bar{t}$ sample which was already studied.

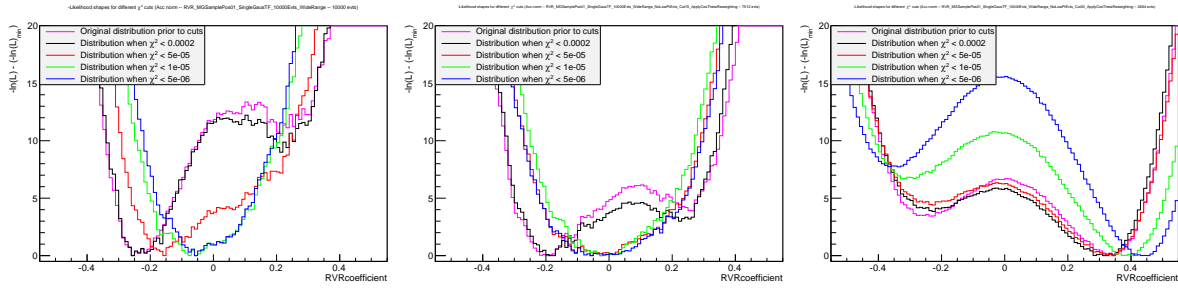


Figure 16.14: Influence of the p_T -cut on the $\ln(\mathcal{L})$ distribution for increasing p_T -cut value (0 GeV, 15 GeV and 30 GeV) for a MG sample created with $V_R = 0.1$ with $\cos \theta^*$ reweighting applied.

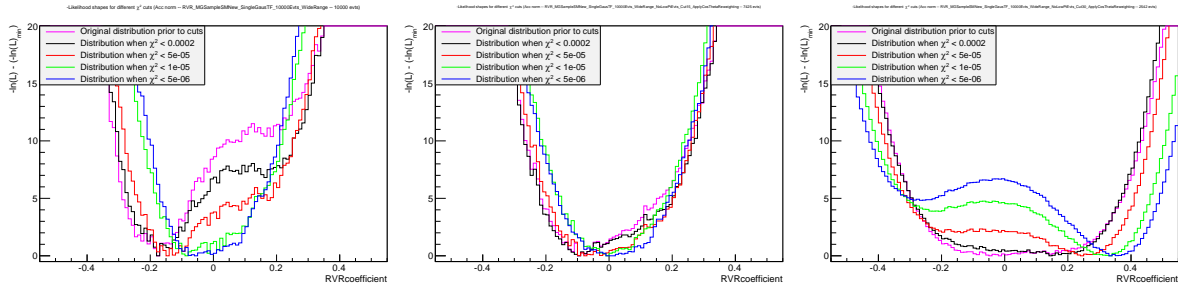


Figure 16.15: Influence of the p_T -cut on the $\ln(\mathcal{L})$ distribution for increasing p_T -cut value (0 GeV, 15 GeV and 30 GeV) for a MG sample created with $V_R = 0.0$ with $\cos \theta^*$ reweighting applied.

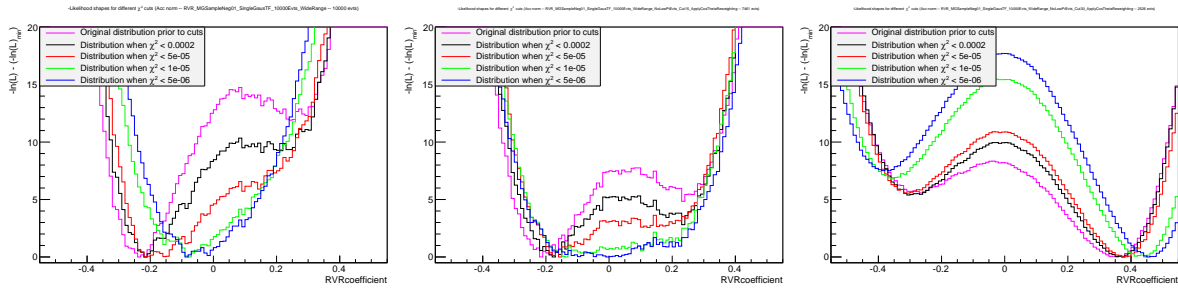


Figure 16.16: Influence of the p_T -cut on the $\ln(\mathcal{L})$ distribution for increasing p_T -cut value (0 GeV, 15 GeV and 30 GeV) for a MG sample created with $V_R = -0.1$ with $\cos \theta^*$ reweighting applied.

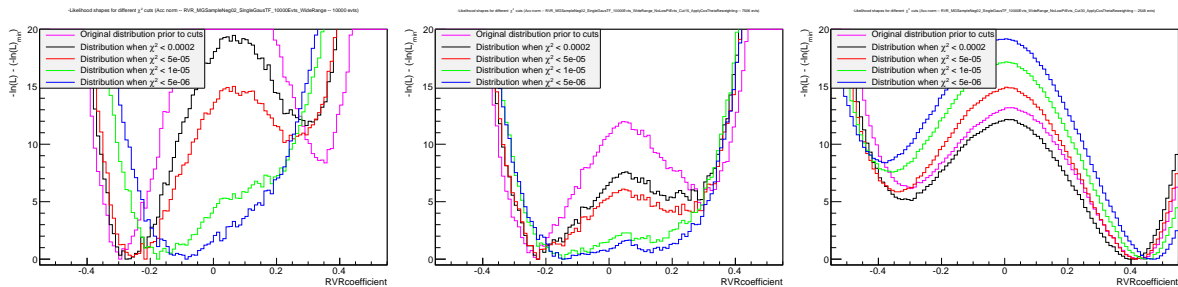


Figure 16.17: Influence of the p_T -cut on the $\ln(\mathcal{L})$ distribution for increasing p_T -cut value (0 GeV, 15 GeV and 30 GeV) for a MG sample created with $V_R = -0.2$ with $\cos \theta^*$ reweighting applied.

16.2. DIFFERENCE BETWEEN $\cos \theta^*$ REWEIGHTING AND ACCEPTANCE NORMALISATION

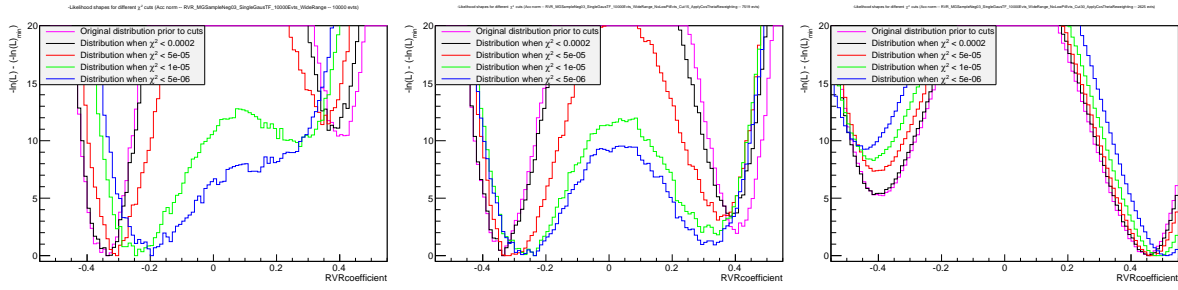


Figure 16.18: Influence of the p_T -cut on the $\ln(\mathcal{L})$ distribution for increasing p_T -cut value (0 GeV, 15 GeV and 30 GeV) for a MG sample created with $V_R = -0.3$ with $\cos \theta^*$ reweighting applied.

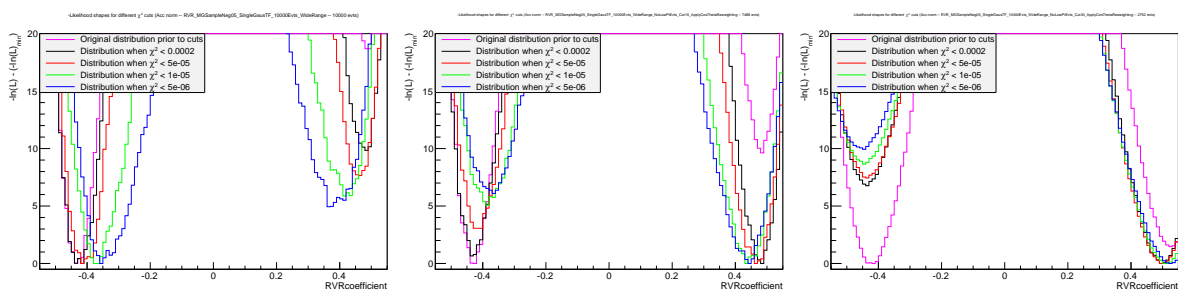


Figure 16.19: Influence of the p_T -cut on the $\ln(\mathcal{L})$ distribution for increasing p_T -cut value (0 GeV, 15 GeV and 30 GeV) for a MG sample created with $V_R = -0.5$ with $\cos \theta^*$ reweighting applied.

16.2 Difference between $\cos \theta^*$ reweighting and acceptance normalisation

However after that this $\cos \theta^*$ reweighting has been applied it was clear that it plays almost the role of the acceptance normalisation since it gives a higher weight to events which have a higher probability to be cut away by the applied event selection based on their $\cos \theta^*$ value. Therefore in order to know whether the issue shown in the beginning cannot just be resolved by the acceptance normalisation, which actually should be applied since not all V_R values react the same on the applied p_T constraints.

Just as was the case for visualizing the influence of the $\cos \theta^*$ reweighting discussed in the previous section, first a selection of $\ln(\mathcal{L})$ distributions will be showed allowing a comparison between the $\cos \theta^*$ reweighting (Fig 16.20) and the acceptance normalisation and afterwards the full list of distributions will be given for each V_R configuration (Figs 16.21 - 16.29).

The full list of $\ln(\mathcal{L})$ distributions is given with the original distribution on the left as was the case in the previous Figures.

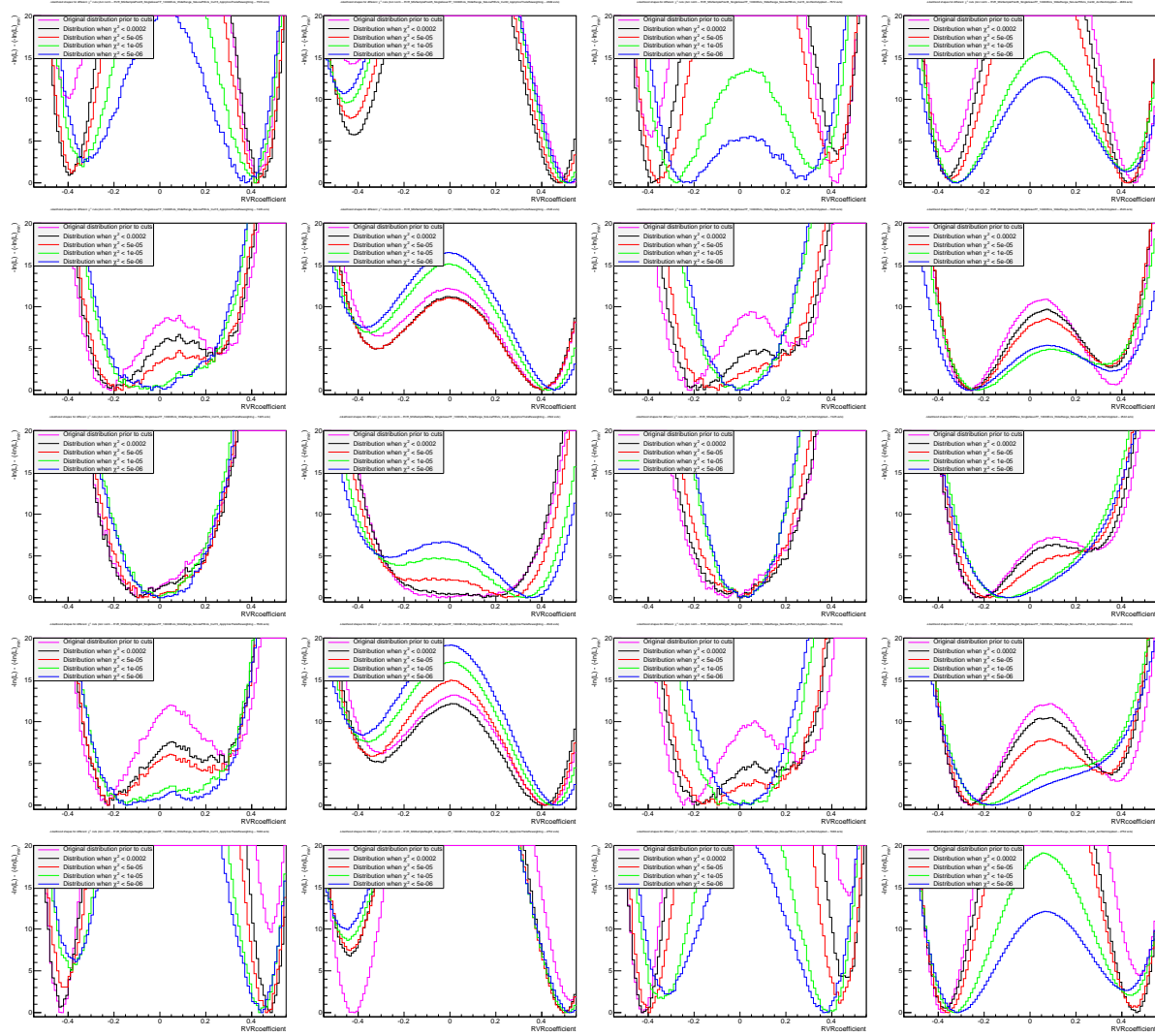


Figure 16.20: Influence of combining the acceptance normalisation with the MadWeight probability on an event-by-event basis. From left to right the different plots always show the same distributions: first the 15 GeV case and 30 GeV case with the $\cos \theta^*$ reweighting and then both with the acceptance normalisation. From top to bottom the different V_R configurations which have been shown are $-0.5, -0.2, 0.0, 0.2$ and 0.5 .

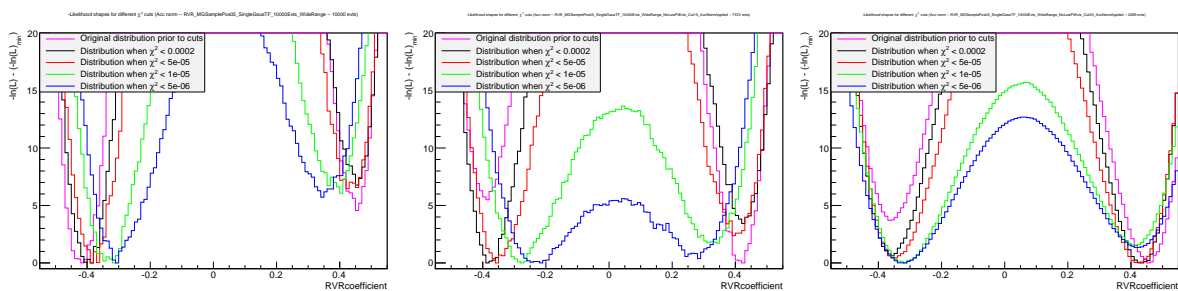


Figure 16.21: Influence of the p_T -cut on the $\ln(\mathcal{L})$ distribution for increasing p_T -cut value (0 GeV, 15 GeV and 30 GeV) for a MG sample created with $V_R = 0.5$ with acceptance normalisation applied.

16.2. DIFFERENCE BETWEEN $\cos \theta^*$ REWEIGHTING AND ACCEPTANCE NORMALISATION

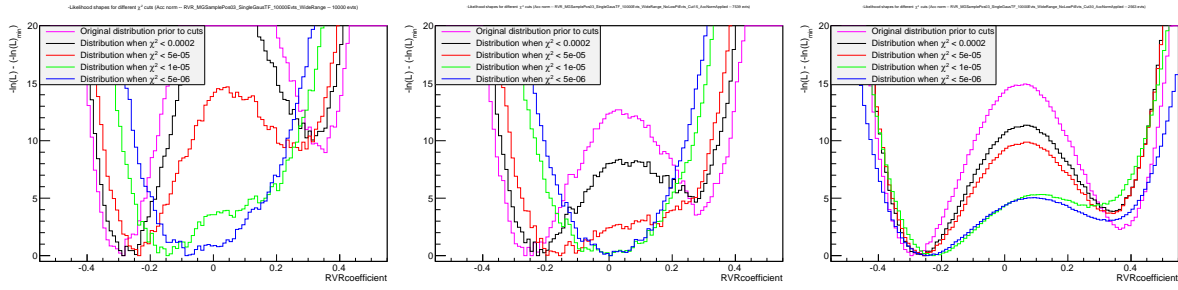


Figure 16.22: Influence of the p_T -cut on the $\ln(\mathcal{L})$ distribution for increasing p_T -cut value (0 GeV, 15 GeV and 30 GeV) for a MG sample created with $V_R = 0.3$ with acceptance normalisation applied.

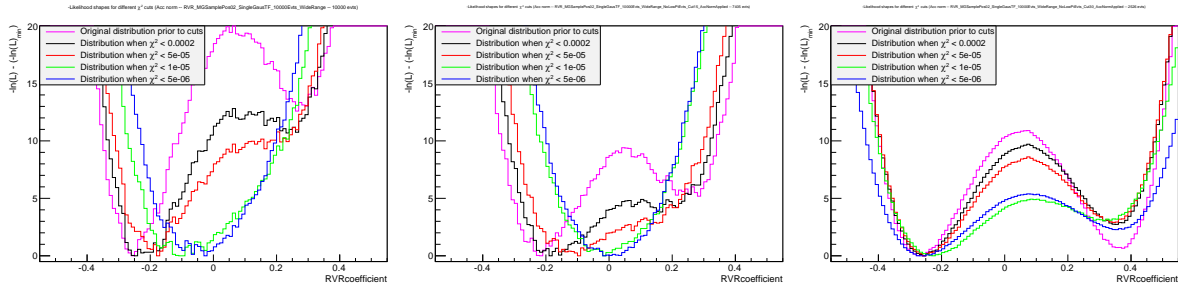


Figure 16.23: Influence of the p_T -cut on the $\ln(\mathcal{L})$ distribution for increasing p_T -cut value (0 GeV, 15 GeV and 30 GeV) for a MG sample created with $V_R = 0.2$ with acceptance normalisation applied.

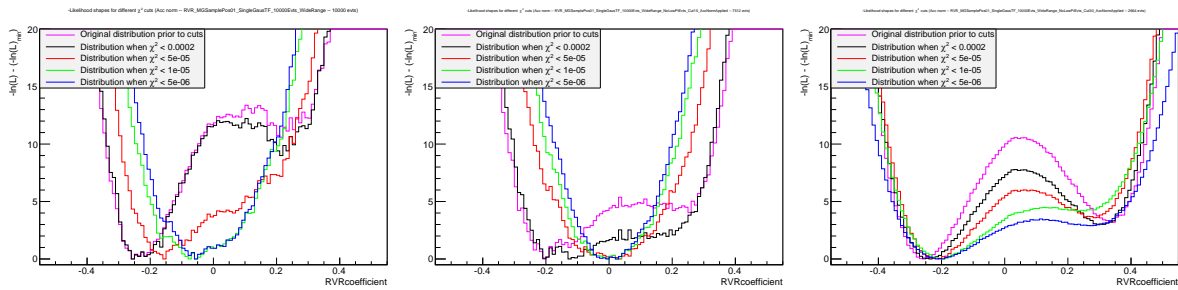


Figure 16.24: Influence of the p_T -cut on the $\ln(\mathcal{L})$ distribution for increasing p_T -cut value (0 GeV, 15 GeV and 30 GeV) for a MG sample created with $V_R = 0.1$ with acceptance normalisation applied.

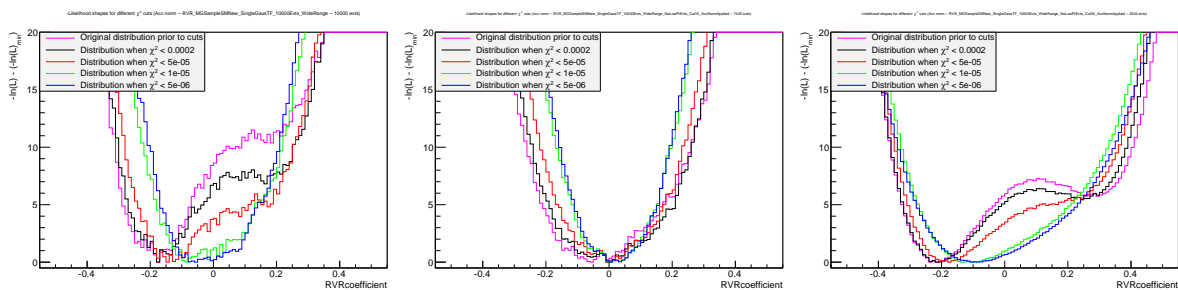


Figure 16.25: Influence of the p_T -cut on the $\ln(\mathcal{L})$ distribution for increasing p_T -cut value (0 GeV, 15 GeV and 30 GeV) for a MG sample created with $V_R = 0.0$ with acceptance normalisation applied.

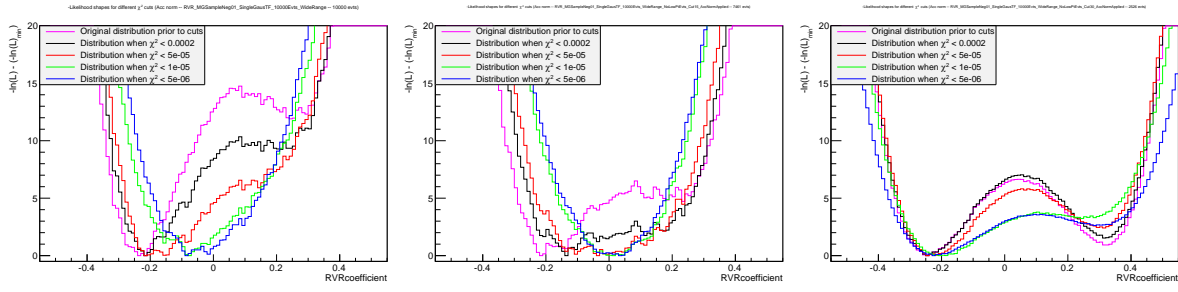


Figure 16.26: Influence of the p_T -cut on the $\ln(\mathcal{L})$ distribution for increasing p_T -cut value (0 GeV, 15 GeV and 30 GeV) for a MG sample created with $V_R = -0.1$ with acceptance normalisation applied.

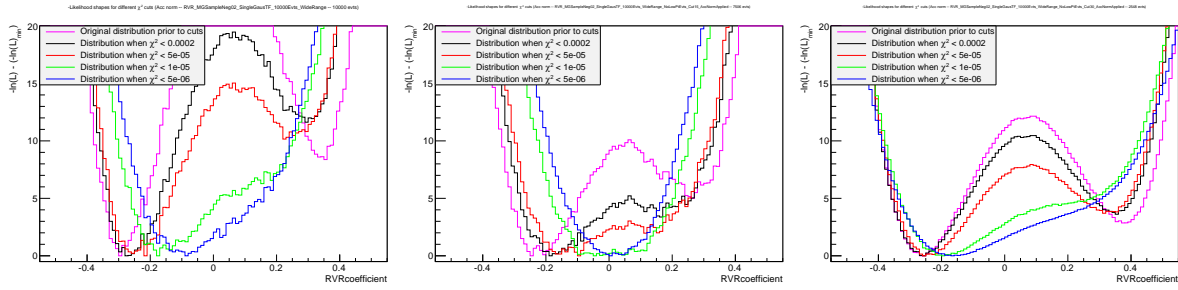


Figure 16.27: Influence of the p_T -cut on the $\ln(\mathcal{L})$ distribution for increasing p_T -cut value (0 GeV, 15 GeV and 30 GeV) for a MG sample created with $V_R = -0.2$ with acceptance normalisation applied.

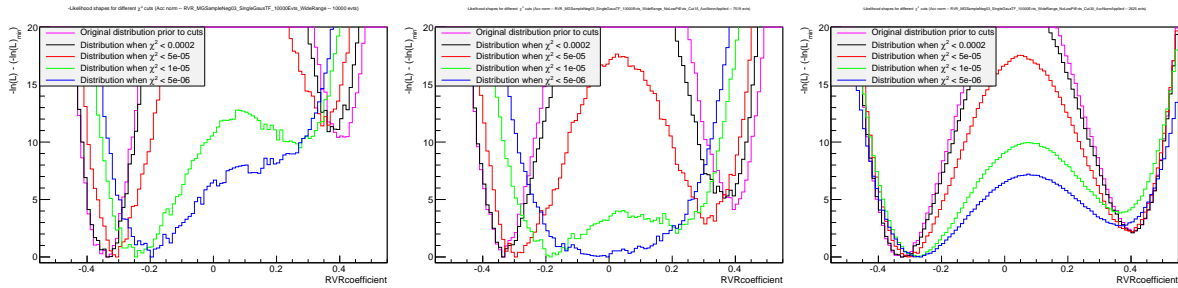


Figure 16.28: Influence of the p_T -cut on the $\ln(\mathcal{L})$ distribution for increasing p_T -cut value (0 GeV, 15 GeV and 30 GeV) for a MG sample created with $V_R = -0.3$ with acceptance normalisation applied.

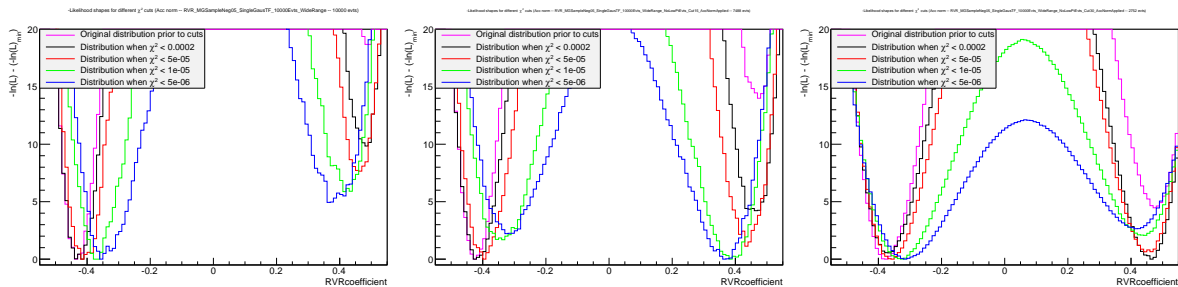


Figure 16.29: Influence of the p_T -cut on the $\ln(\mathcal{L})$ distribution for increasing p_T -cut value (0 GeV, 15 GeV and 30 GeV) for a MG sample created with $V_R = -0.5$ with acceptance normalisation applied.

16.3 Applying both $\cos \theta^*$ and acceptance normalisation?

As a final test, motivated by the fact that the results obtained from the $\cos \theta^*$ reweighting and the acceptance normalisation show some differences, is to see whether both corrections can be applied together.

However on first sight it seems that this would actually result in overcorrecting the type of events which are more likely to be affected by the applied event selection constraints. But not very certain whether there exists a control check which can be performed in order to make sure that it is actually doing the right thing ...

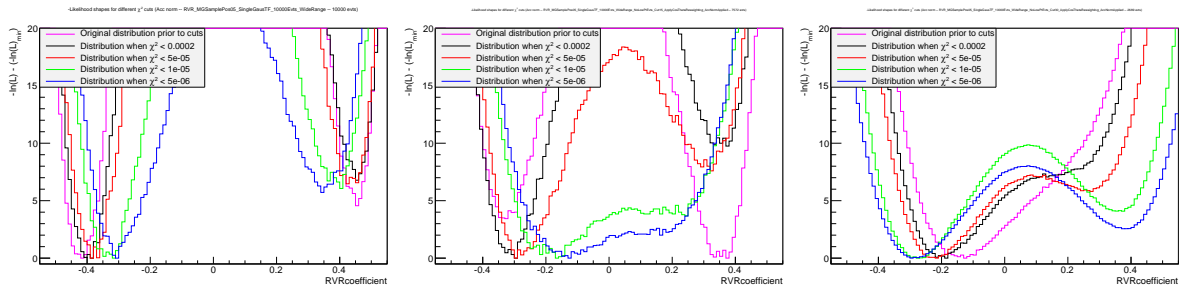


Figure 16.30: Influence of the p_T -cut on the $\ln(\mathcal{L})$ distribution for increasing p_T -cut value (0 GeV, 15 GeV and 30 GeV) for a MG sample created with $V_R = 0.5$ with acceptance normalisation and $\cos \theta^*$ reweighting applied.

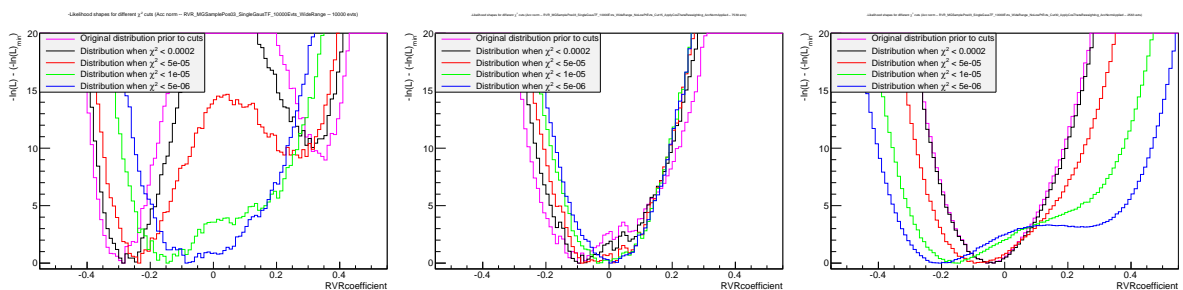


Figure 16.31: Influence of the p_T -cut on the $\ln(\mathcal{L})$ distribution for increasing p_T -cut value (0 GeV, 15 GeV and 30 GeV) for a MG sample created with $V_R = 0.3$ with acceptance normalisation and $\cos \theta^*$ reweighting applied.

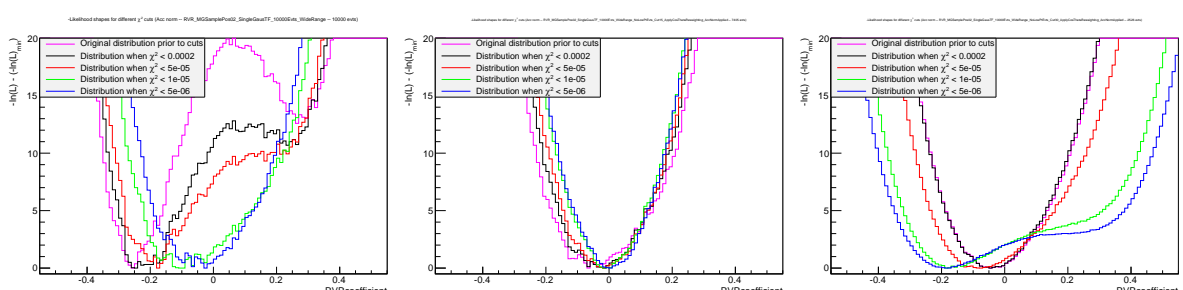


Figure 16.32: Influence of the p_T -cut on the $\ln(\mathcal{L})$ distribution for increasing p_T -cut value (0 GeV, 15 GeV and 30 GeV) for a MG sample created with $V_R = 0.2$ with acceptance normalisation and $\cos \theta^*$ reweighting applied.

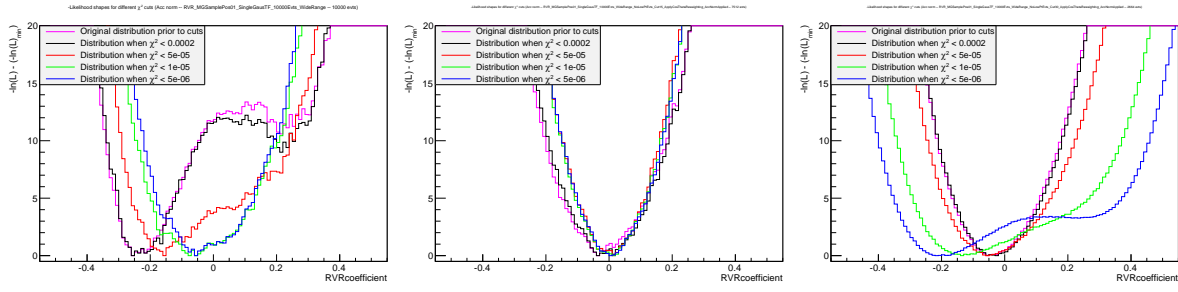


Figure 16.33: Influence of the p_T -cut on the $\ln(\mathcal{L})$ distribution for increasing p_T -cut value (0 GeV, 15 GeV and 30 GeV) for a MG sample created with $V_R = 0.1$ with acceptance normalisation and $\cos\theta^*$ reweighting applied.

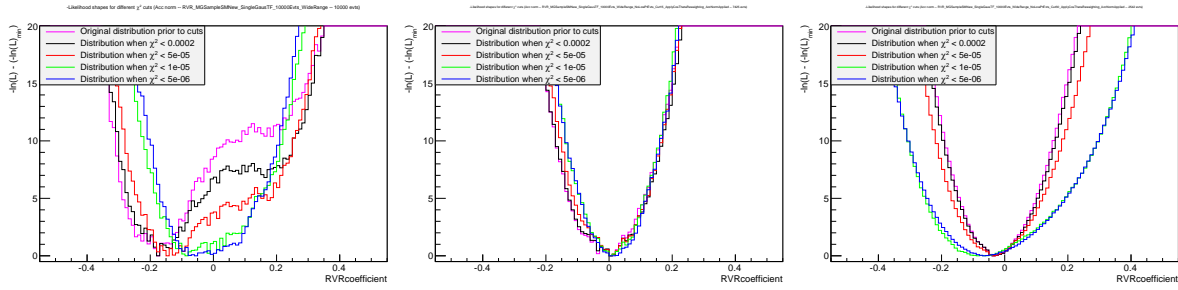


Figure 16.34: Influence of the p_T -cut on the $\ln(\mathcal{L})$ distribution for increasing p_T -cut value (0 GeV, 15 GeV and 30 GeV) for a MG sample created with $V_R = 0.0$ with acceptance normalisation and $\cos\theta^*$ reweighting applied.

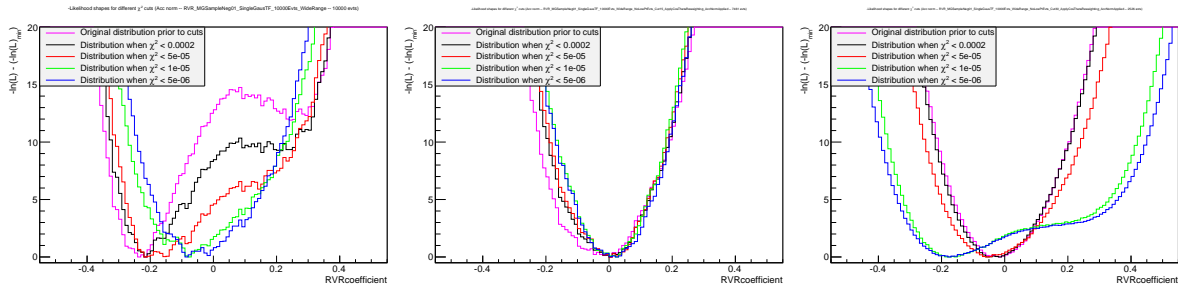


Figure 16.35: Influence of the p_T -cut on the $\ln(\mathcal{L})$ distribution for increasing p_T -cut value (0 GeV, 15 GeV and 30 GeV) for a MG sample created with $V_R = -0.1$ with acceptance normalisation and $\cos\theta^*$ reweighting applied.

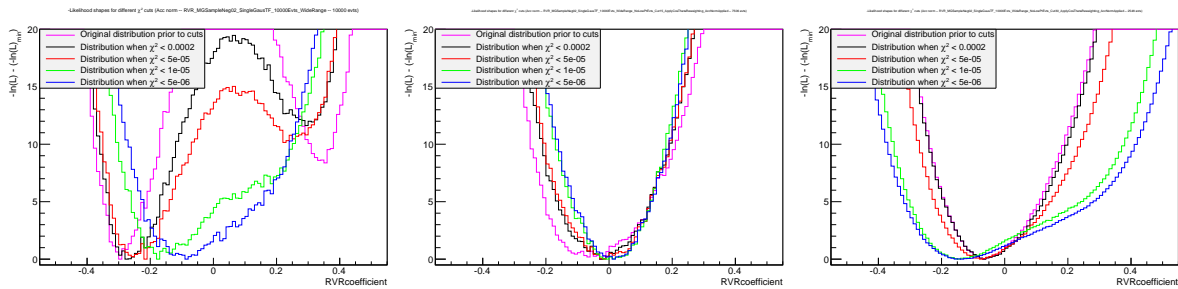


Figure 16.36: Influence of the p_T -cut on the $\ln(\mathcal{L})$ distribution for increasing p_T -cut value (0 GeV, 15 GeV and 30 GeV) for a MG sample created with $V_R = -0.2$ with acceptance normalisation and $\cos\theta^*$ reweighting applied.

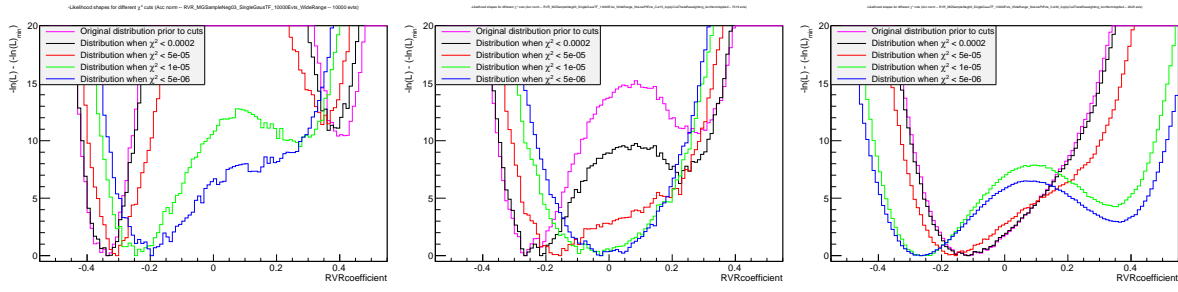


Figure 16.37: Influence of the p_T -cut on the $\ln(\mathcal{L})$ distribution for increasing p_T -cut value (0 GeV, 15 GeV and 30 GeV) for a MG sample created with $V_R = -0.3$ with acceptance normalisation and $\cos \theta^*$ reweighting applied.

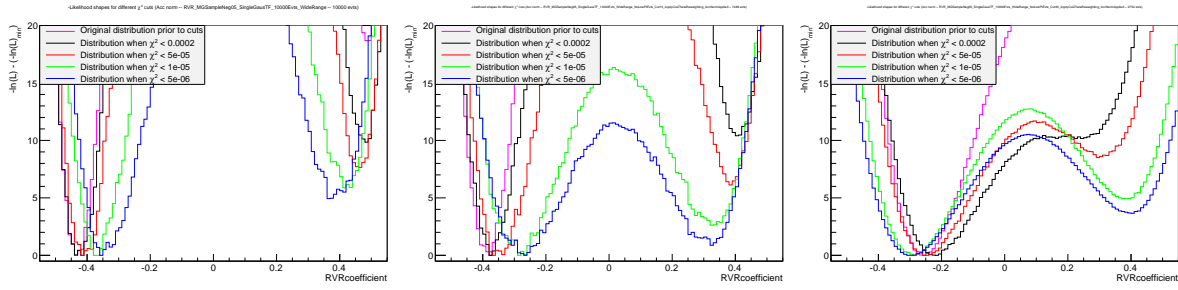


Figure 16.38: Influence of the p_T -cut on the $\ln(\mathcal{L})$ distribution for increasing p_T -cut value (0 GeV, 15 GeV and 30 GeV) for a MG sample created with $V_R = -0.5$ with acceptance normalisation and $\cos \theta^*$ reweighting applied.

16.4 Adapting the implementation used

In the previous sections the $\cos \theta^*$ reweighting has not been applied in a correct way. For these distributions the calculated weight was only multiplied with the MadWeight probability and the cross-section normalisation was not taken into account. Since this weight has to be applied on an event-by-event basis it should be multiplied with the term $\frac{P_{MW}}{\sigma}$ before the logarithm is taken. Hence the way the reweighting is currently implemented is the following:

$$-\ln \mathcal{L} = -\ln P_{MW} * w_{i,\cos \theta^*} + \ln \sigma_{XS/Acc} * w_{i,\cos \theta^*} \quad (16.2)$$

And this is updated to:

$$-\ln \mathcal{L} = -\ln(P_{MW} * w_{i,\cos \theta^*}) + \ln \sigma_{XS/Acc} \quad (16.3)$$

The only results which differ with this altered definition are the one in the following cases:

- $\cos \theta^*$ reweighting applied but no acceptance normalisation applied
- Both $\cos \theta^*$ reweighting and acceptance normalisation applied

For these two the corresponding histograms will be listed again and should be compared with the previously obtained ones:

A direct comparison between the two definitions used can be found in Figure 16.48.

Now the same will be shown when both the $\cos \theta^*$ reweighting and the acceptance normalisation have been applied. This is given in Figures 16.49 to 16.57. Afterwards the

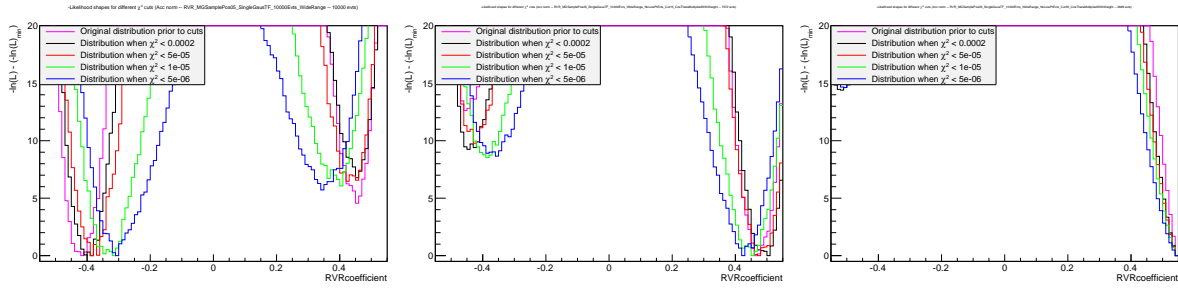


Figure 16.39: Influence of the p_T -cut on the $\ln(\mathcal{L})$ distribution for increasing p_T -cut value (0 GeV, 15 GeV and 30 GeV) for a MG sample created with $V_R = 0.5$ with $\cos \theta^*$ reweighting applied (updated implementation).

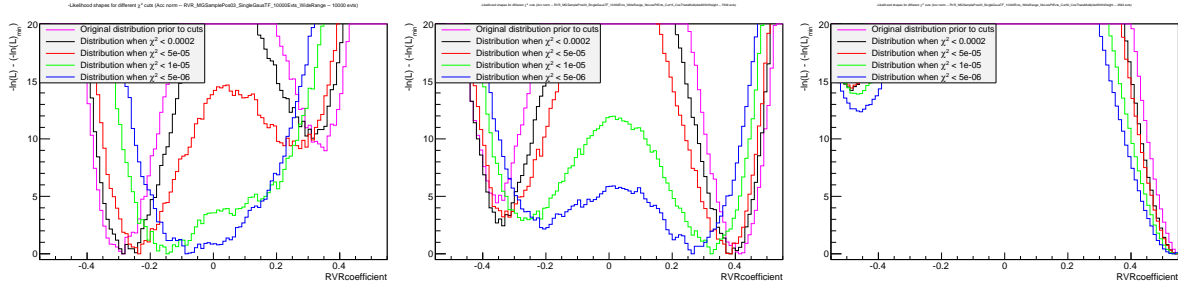


Figure 16.40: Influence of the p_T -cut on the $\ln(\mathcal{L})$ distribution for increasing p_T -cut value (0 GeV, 15 GeV and 30 GeV) for a MG sample created with $V_R = 0.3$ with $\cos \theta^*$ reweighting applied (updated implementation).

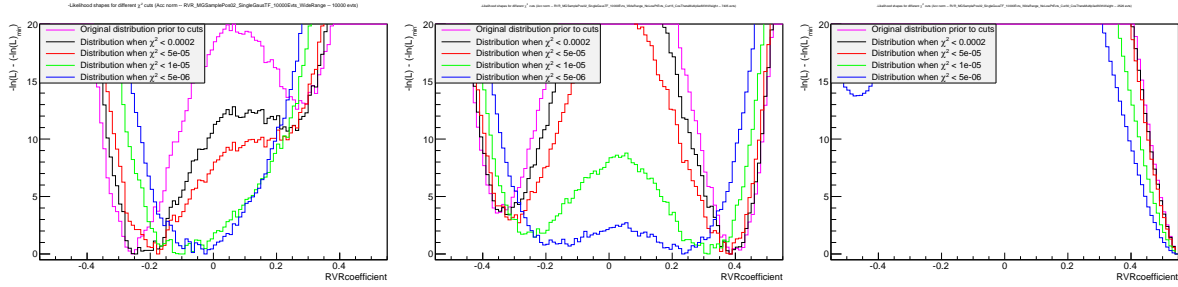


Figure 16.41: Influence of the p_T -cut on the $\ln(\mathcal{L})$ distribution for increasing p_T -cut value (0 GeV, 15 GeV and 30 GeV) for a MG sample created with $V_R = 0.2$ with $\cos \theta^*$ reweighting applied (updated implementation).

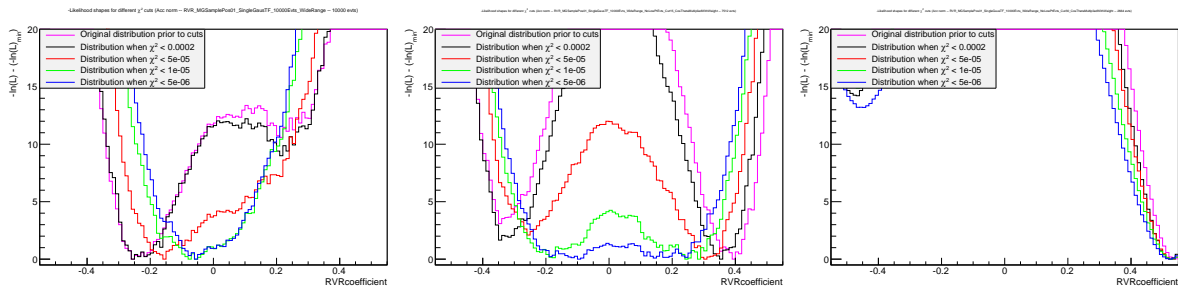


Figure 16.42: Influence of the p_T -cut on the $\ln(\mathcal{L})$ distribution for increasing p_T -cut value (0 GeV, 15 GeV and 30 GeV) for a MG sample created with $V_R = 0.1$ with $\cos \theta^*$ reweighting applied (updated implementation).

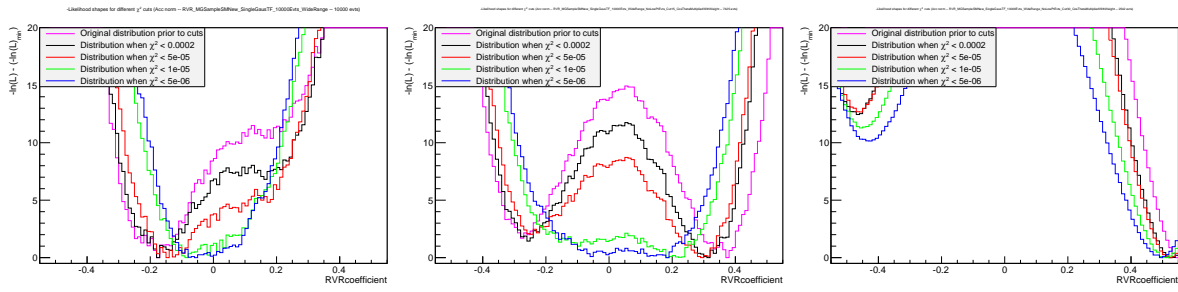


Figure 16.43: Influence of the p_T -cut on the $\ln(\mathcal{L})$ distribution for increasing p_T -cut value (0 GeV, 15 GeV and 30 GeV) for a MG sample created with $V_R = 0.0$ with $\cos \theta^*$ reweighting applied (updated implementation).

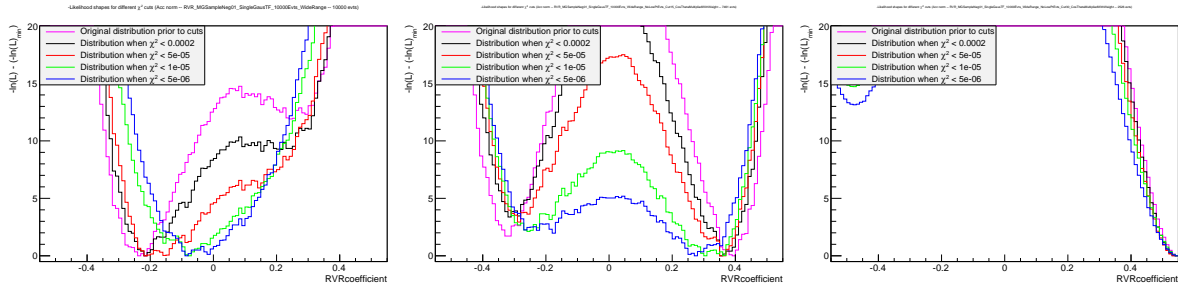


Figure 16.44: Influence of the p_T -cut on the $\ln(\mathcal{L})$ distribution for increasing p_T -cut value (0 GeV, 15 GeV and 30 GeV) for a MG sample created with $V_R = -0.1$ with $\cos \theta^*$ reweighting applied (updated implementation).

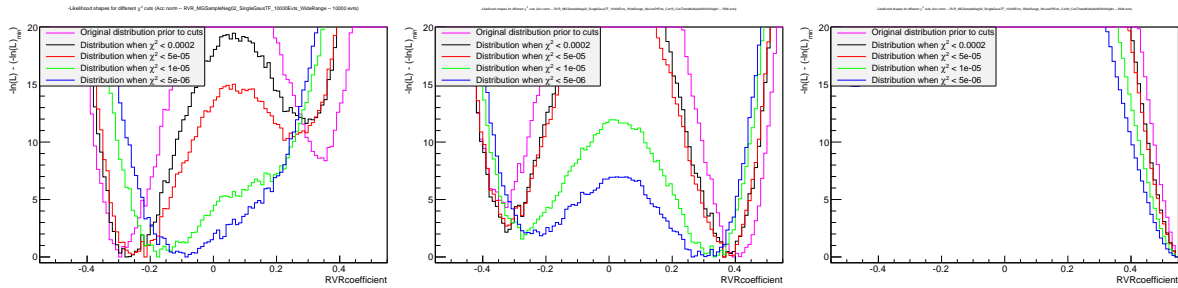


Figure 16.45: Influence of the p_T -cut on the $\ln(\mathcal{L})$ distribution for increasing p_T -cut value (0 GeV, 15 GeV and 30 GeV) for a MG sample created with $V_R = -0.2$ with $\cos \theta^*$ reweighting applied (updated implementation).

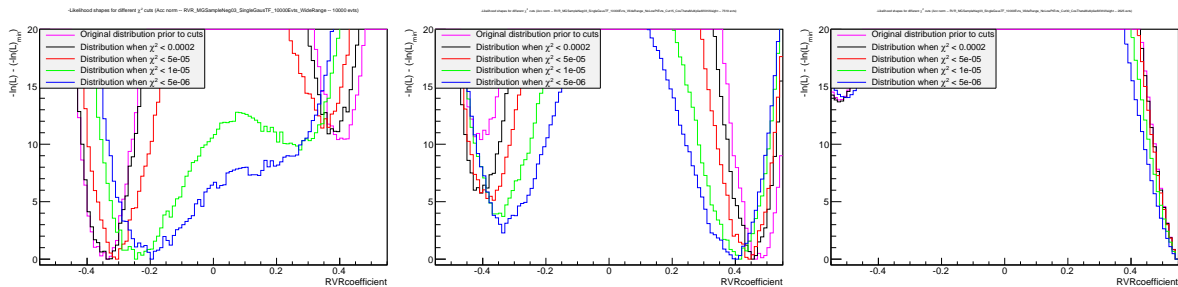


Figure 16.46: Influence of the p_T -cut on the $\ln(\mathcal{L})$ distribution for increasing p_T -cut value (0 GeV, 15 GeV and 30 GeV) for a MG sample created with $V_R = -0.3$ with $\cos \theta^*$ reweighting applied (updated implementation).

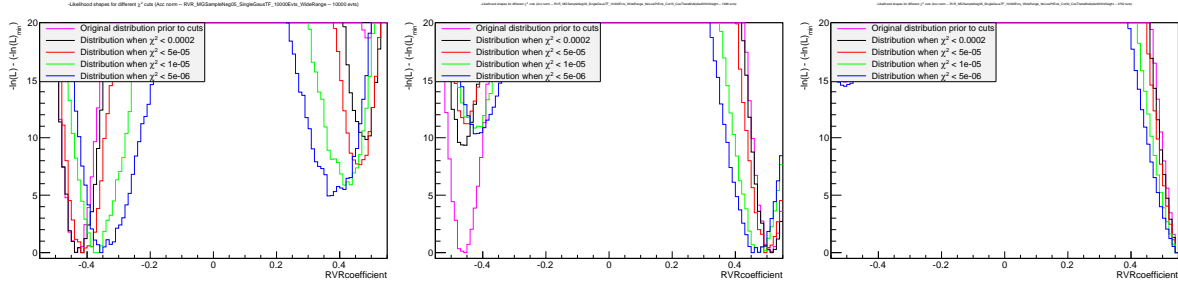


Figure 16.47: Influence of the p_T -cut on the $\ln(\mathcal{L})$ distribution for increasing p_T -cut value (0 GeV, 15 GeV and 30 GeV) for a MG sample created with $V_R = -0.5$ with $\cos \theta^*$ reweighting applied (updated implementation).

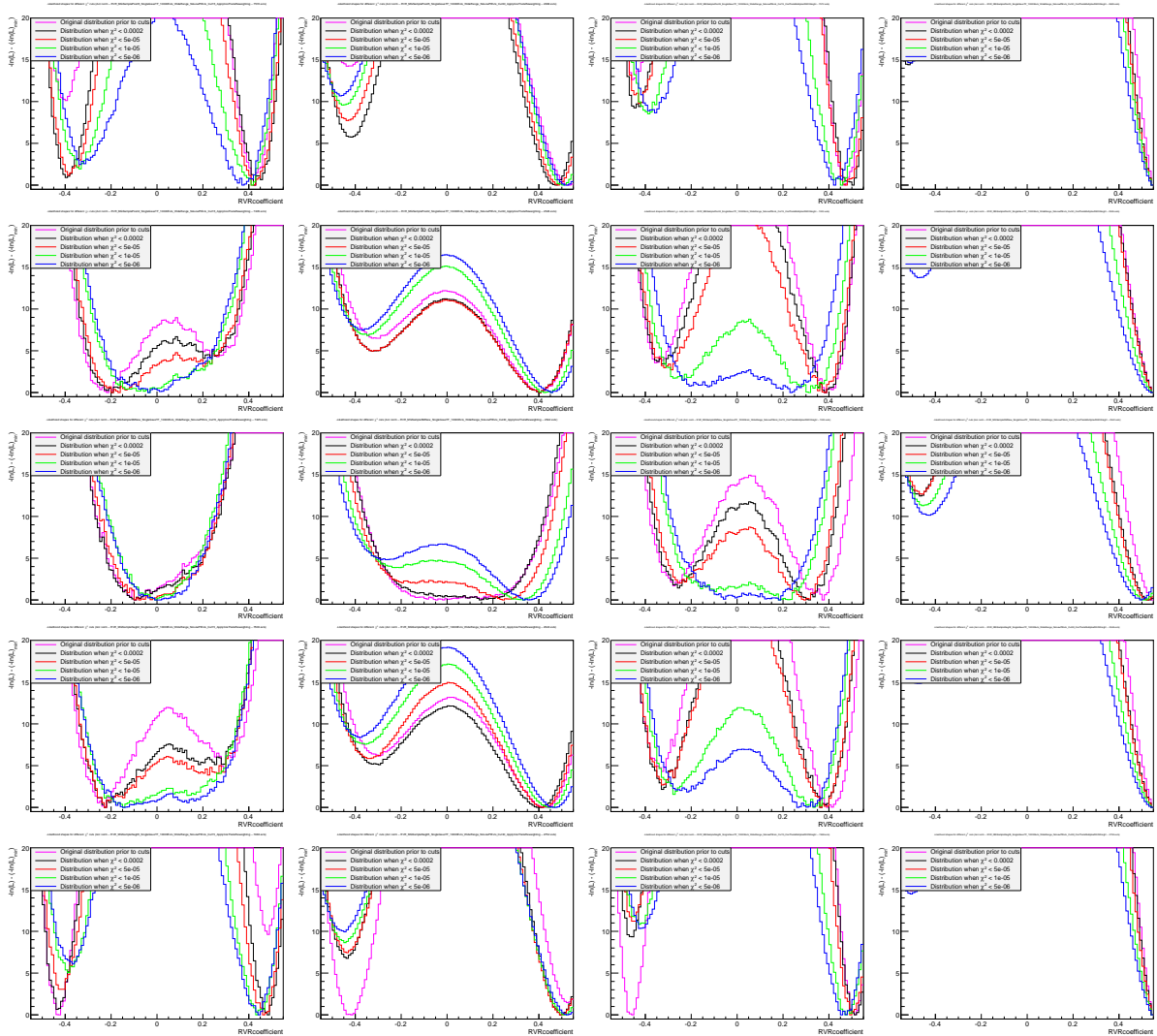


Figure 16.48: Influence of combining the $\cos \theta^*$ reweighting with the MadWeight probability on an event-by-event basis. From left to right the different plots always show the same distributions: first the 15 GeV case and 30 GeV case with the first $\cos \theta^*$ reweighting implemented and then with the updated definition. From top to bottom the different V_R configurations which have been shown are $-0.5, -0.2, 0.0, 0.2$ and 0.5 .

comparison between the two considered $\cos \theta^*$ reweighting implementations is given in

Figure 16.58.

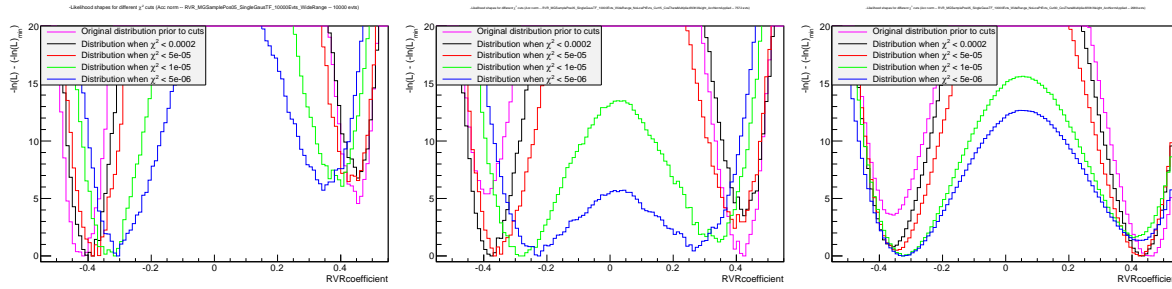


Figure 16.49: Influence of the p_T -cut on the $\ln(\mathcal{L})$ distribution for increasing p_T -cut value (0 GeV, 15 GeV and 30 GeV) for a MG sample created with $V_R = 0.5$ with $\cos \theta^*$ reweighting and acceptance normalisation applied (updated implementation).

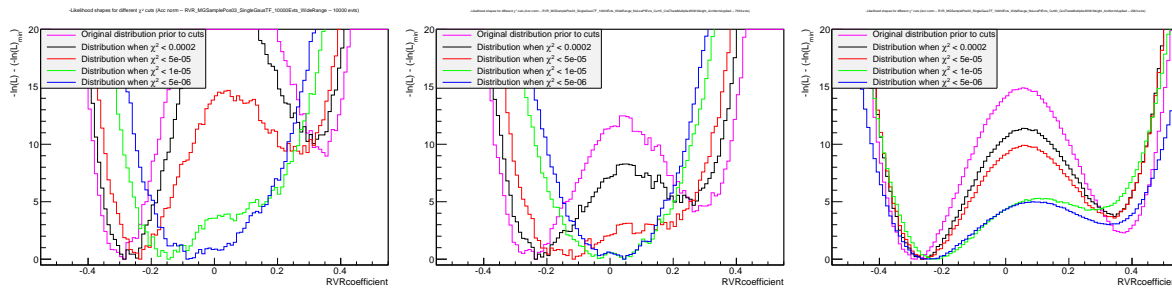


Figure 16.50: Influence of the p_T -cut on the $\ln(\mathcal{L})$ distribution for increasing p_T -cut value (0 GeV, 15 GeV and 30 GeV) for a MG sample created with $V_R = 0.3$ with $\cos \theta^*$ reweighting and acceptance normalisation applied (updated implementation).

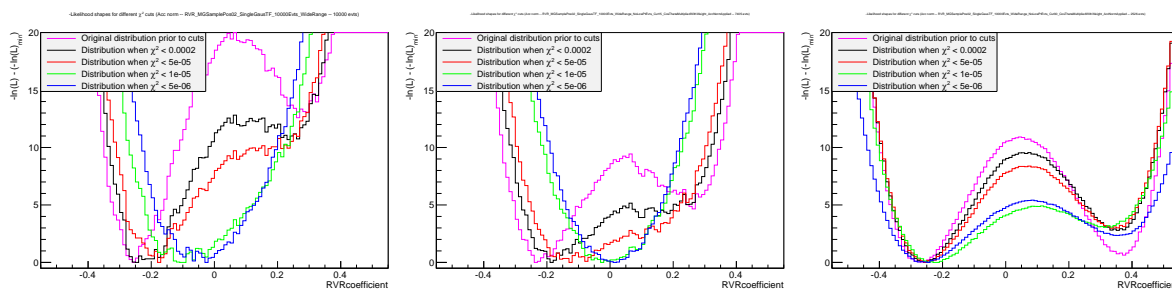


Figure 16.51: Influence of the p_T -cut on the $\ln(\mathcal{L})$ distribution for increasing p_T -cut value (0 GeV, 15 GeV and 30 GeV) for a MG sample created with $V_R = 0.2$ with $\cos \theta^*$ reweighting and acceptance normalisation applied (updated implementation).

It seems that this new implementation of the $\cos \theta^*$ reweighting actually has no influence at all on the $\ln(\mathcal{L})$ shape ...

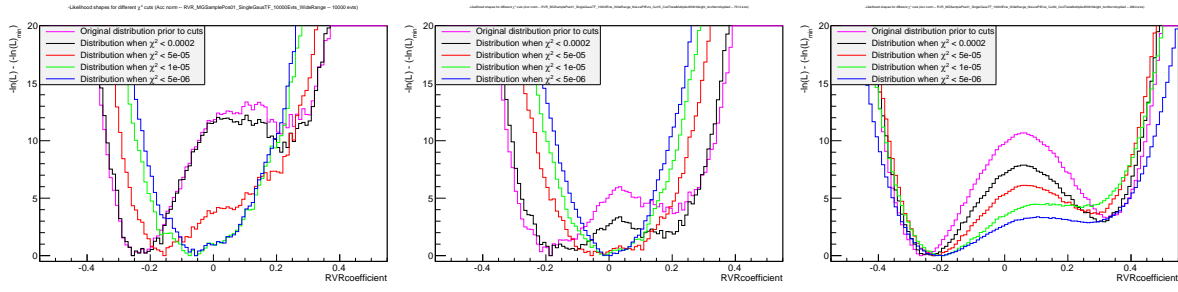


Figure 16.52: Influence of the p_T -cut on the $\ln(\mathcal{L})$ distribution for increasing p_T -cut value (0 GeV, 15 GeV and 30 GeV) for a MG sample created with $V_R = 0.1$ with $\cos \theta^*$ reweighting and acceptance normalisation applied (updated implementation).

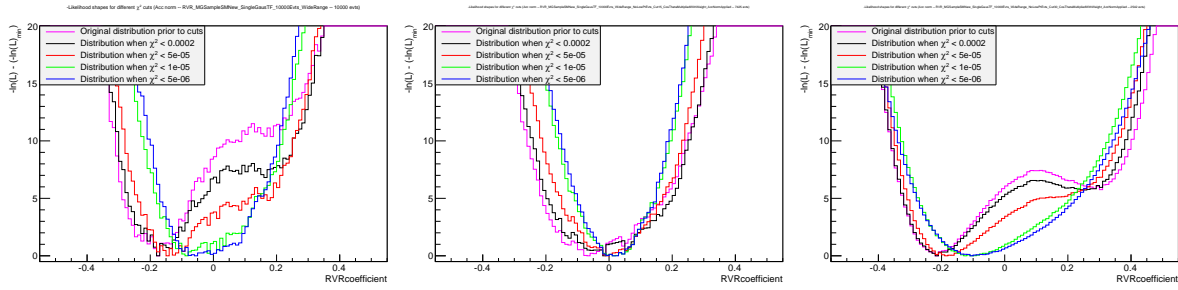


Figure 16.53: Influence of the p_T -cut on the $\ln(\mathcal{L})$ distribution for increasing p_T -cut value (0 GeV, 15 GeV and 30 GeV) for a MG sample created with $V_R = 0.0$ with $\cos \theta^*$ reweighting and acceptance normalisation applied (updated implementation).

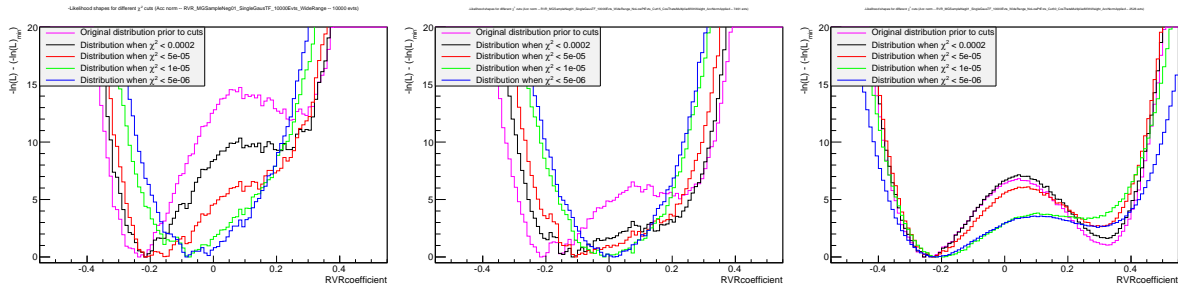


Figure 16.54: Influence of the p_T -cut on the $\ln(\mathcal{L})$ distribution for increasing p_T -cut value (0 GeV, 15 GeV and 30 GeV) for a MG sample created with $V_R = -0.1$ with $\cos \theta^*$ reweighting and acceptance normalisation applied (updated implementation).

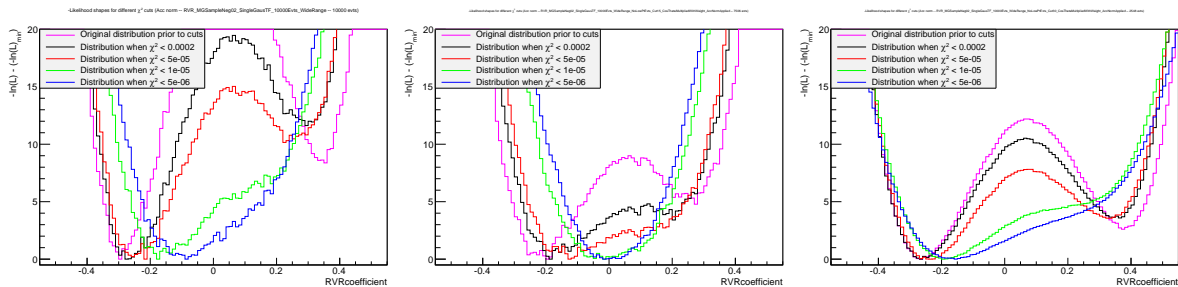


Figure 16.55: Influence of the p_T -cut on the $\ln(\mathcal{L})$ distribution for increasing p_T -cut value (0 GeV, 15 GeV and 30 GeV) for a MG sample created with $V_R = -0.2$ with $\cos \theta^*$ reweighting and acceptance normalisation applied (updated implementation).

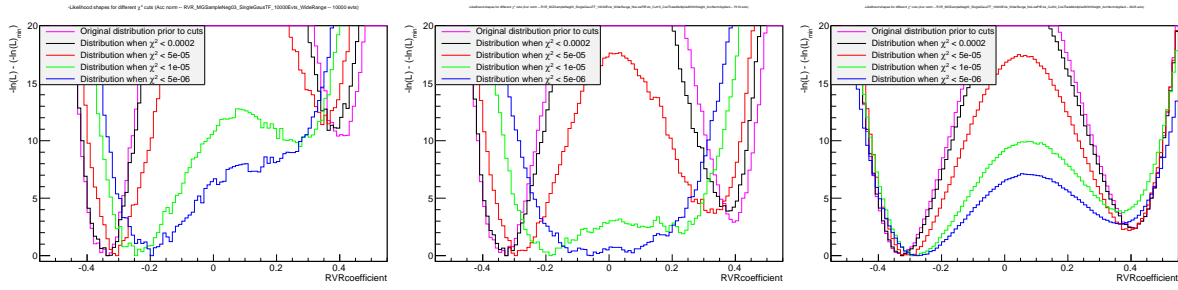


Figure 16.56: Influence of the p_T -cut on the $\ln(\mathcal{L})$ distribution for increasing p_T -cut value (0 GeV, 15 GeV and 30 GeV) for a MG sample created with $V_R = -0.3$ with $\cos \theta^*$ reweighting and acceptance normalisation applied (updated implementation).

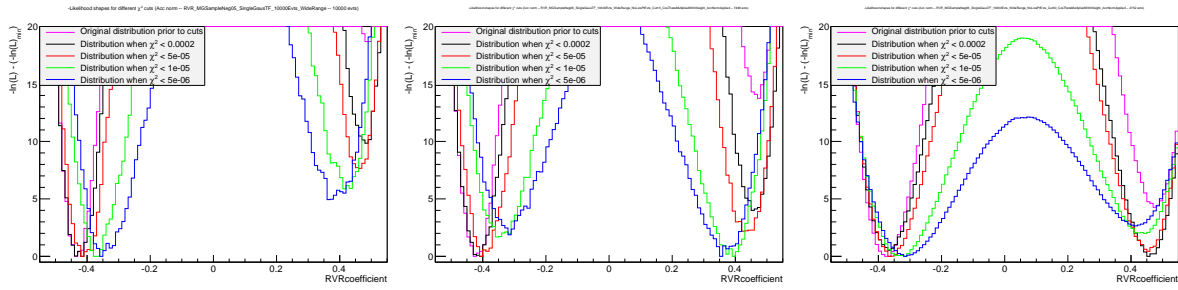


Figure 16.57: Influence of the p_T -cut on the $\ln(\mathcal{L})$ distribution for increasing p_T -cut value (0 GeV, 15 GeV and 30 GeV) for a MG sample created with $V_R = -0.5$ with $\cos \theta^*$ reweighting and acceptance normalisation applied (updated implementation).

16.5 Ensuring $\cos \theta^*$ normalisation

In order to apply this $\cos \theta^*$ reweighting it has to be checked in detail whether the applied correction does not break the normalisation of the MadWeight probability¹.

¹This normalisation was checked by calculating which likelihood value is obtained when the cross-section normalisation is not applied. This value should correspond to the MadWeight cross-section which is then proven to be the necessary normalisation factor needed to ensure a probability density.

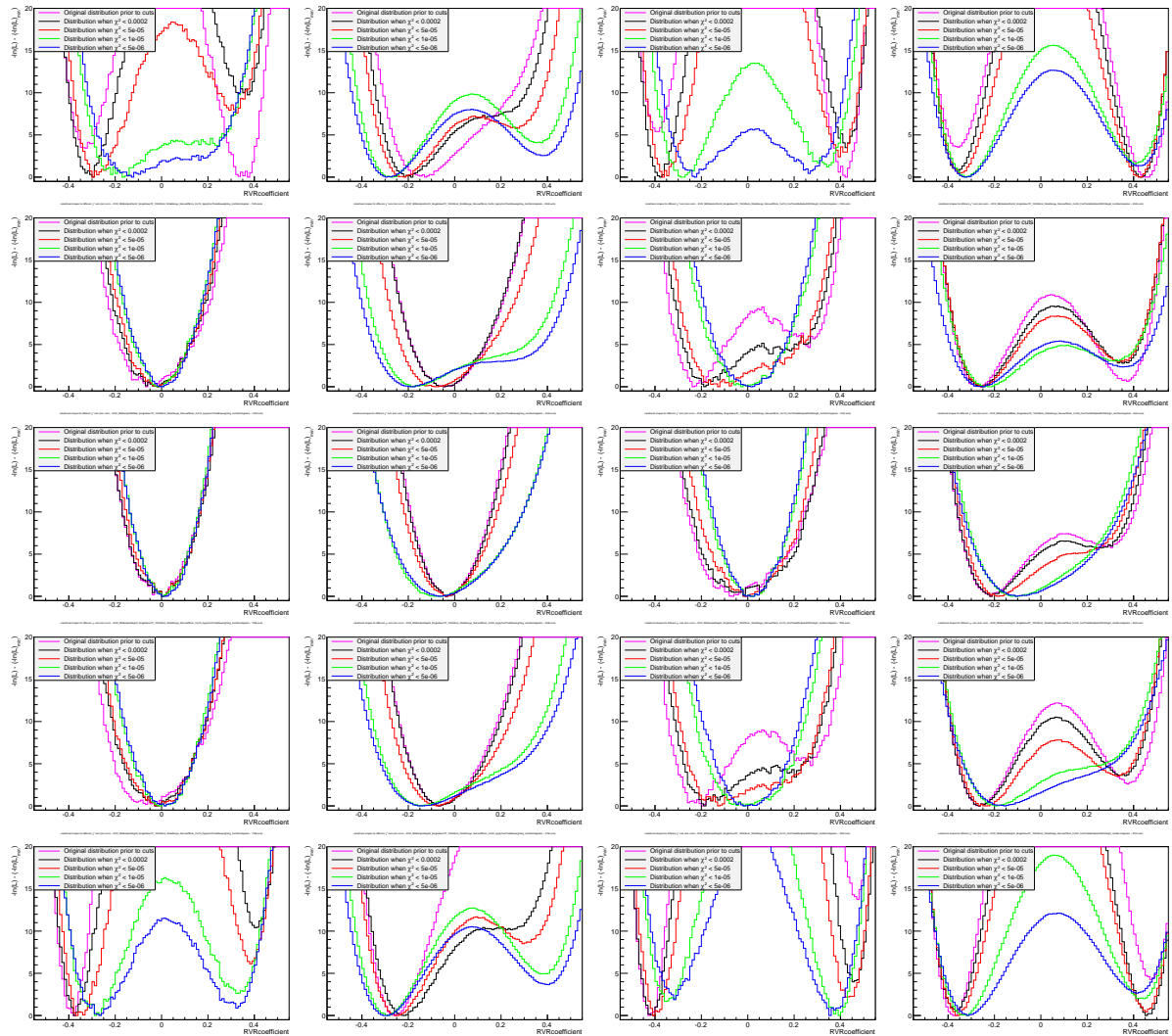


Figure 16.58: Influence of combining the $\cos \theta^*$ reweighting with the MadWeight probability on an event-by-event basis. From left to right the different plots always show the same distributions: first the 15 GeV case and 30 GeV case with the first $\cos \theta^*$ reweighting implemented and then with the updated definition (acceptance normalisation is applied each time). From top to bottom the different V_R configurations which have been shown are $-0.5, -0.2, 0.0, 0.2$ and 0.5 .

Chapter 17

Effect of applying cut on FitDeviation in stead of on χ^2

The problem of applying a cut on the χ^2 of the 4th order polynomial through the number of reduced points is that it is likely to not have the complete physical meaning due to the lack of uncertainties on the MadWeight probabilities. Hence the χ^2 calculation will need to choose an arbitrary value to use as uncertainty when calculating the χ^2 of the fitted function. A possible solution can lie in using the “FitDeviation” variable which represents the total deviation of the measured points from the value suggested by the fit, relative to the value of the measured point.

$$\text{FitDeviation} = \sum_{\text{bin } i} \frac{|x_i - f(x_i)|}{x_i} \quad (17.1)$$

This distribution should also be considered for ensuring that the number of excluded points is sufficient. This is the case when this distribution does not have a tail property anymore.

Chapter 18

Comparision between first and second polynomial fit

Since the considered range is rather limited for the moment and the number of studied points is not much less than the number of degrees of freedom necessary to fit a decent polynomial of order 4, it should be ensured that a clear benefit is gained from applying this double-fit procedure. Since for the second fit in this double-fit procedure 3 out of 9 points are rejected, only 6 points remain to fit a 4th order polynomial which requires 5 points hence leaving only 1 single degree of freedom. This could possibly lead to problems, mainly because it is rather likely that good points are rejected and it is very difficult to check this from the individual $\ln(\mathcal{L})$ distributions.

Therefore it should be checked whether the first fit could not be sufficient to obtain a smooth overall $\ln(\mathcal{L})$ distribution and whether the badly behaving events cannot be removed using the χ^2 or FitDeviation rejection as before. As a first step the distributions without any influence of the p_T cut will be considered, as given in Figure 18.1 to 18.9. Here the sum of the first fit on the full range is given on the left while the second fit on the reduced number of events is given on the right.

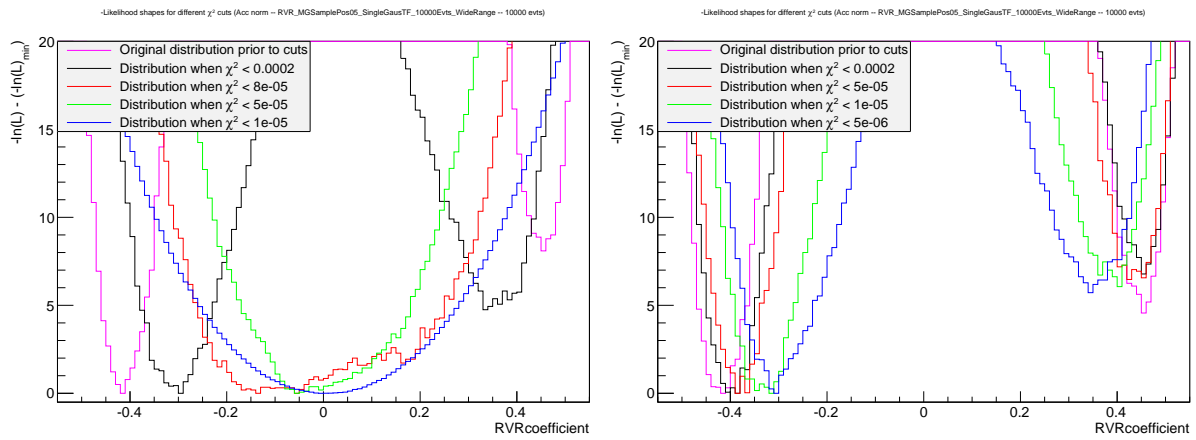


Figure 18.1: Overall $\ln(\mathcal{L})$ distribution for MG samples created with $V_R = 0.5$ obtained from the first fit (left) and the second fit (right) prior to any p_T -cut requirement. The different χ^2 cuts applied correspond to percentages of about!!

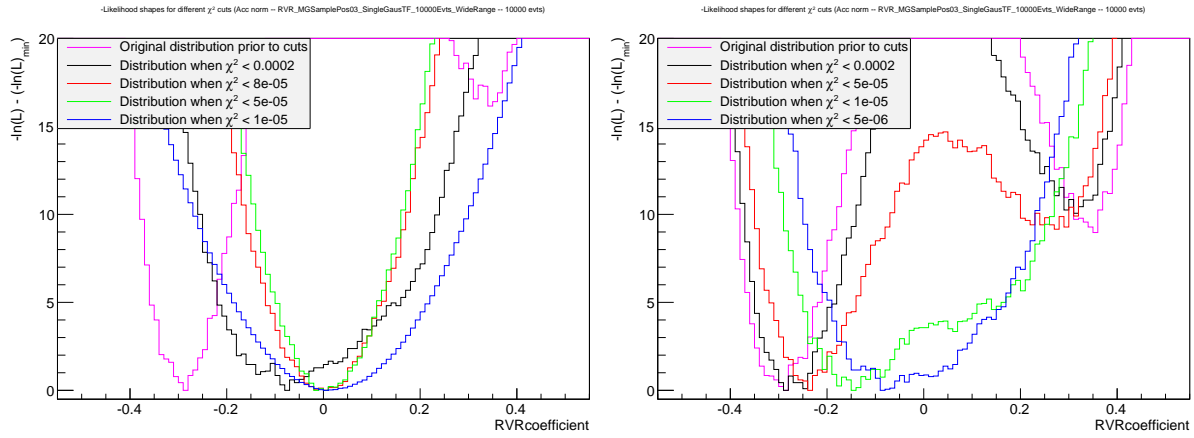


Figure 18.2: Overall $\ln(\mathcal{L})$ distribution for MG samples created with $V_R = 0.3$ obtained from the first fit (left) and the second fit (right) prior to any p_T -cut requirement. The different χ^2 cuts applied correspond to percentages of about!!

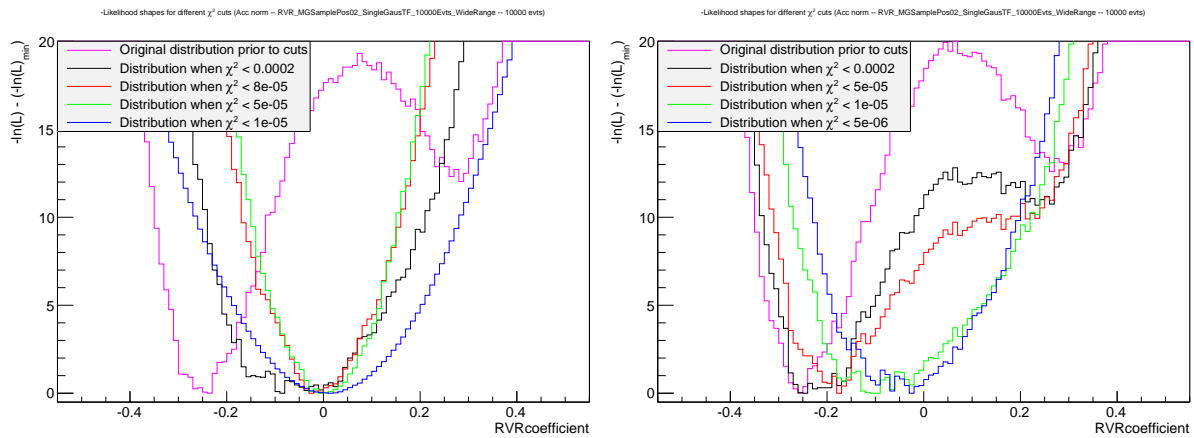


Figure 18.3: Overall $\ln(\mathcal{L})$ distribution for MG samples created with $V_R = 0.2$ obtained from the first fit (left) and the second fit (right) prior to any p_T -cut requirement. The different χ^2 cuts applied correspond to percentages of about!!

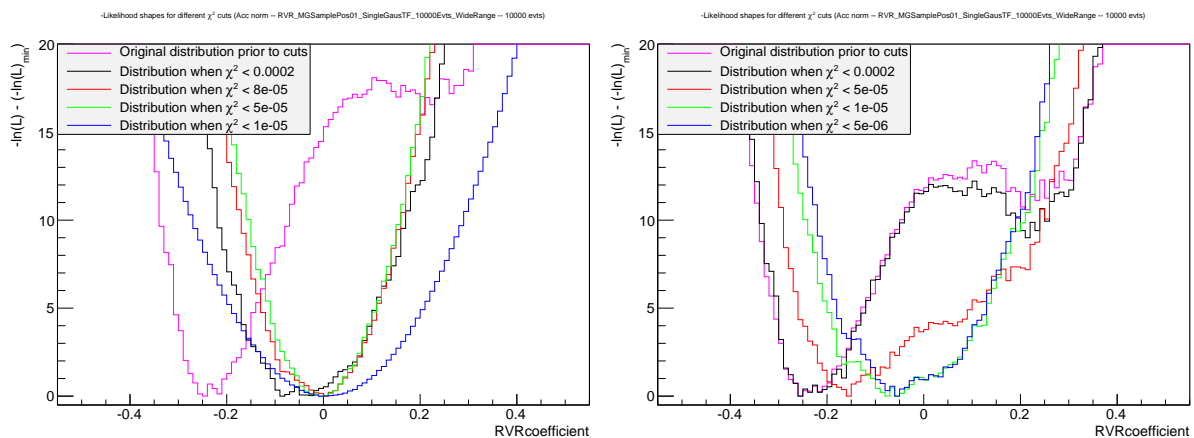


Figure 18.4: Overall $\ln(\mathcal{L})$ distribution for MG samples created with $V_R = 0.1$ obtained from the first fit (left) and the second fit (right) prior to any p_T -cut requirement. The different χ^2 cuts applied correspond to percentages of about!!

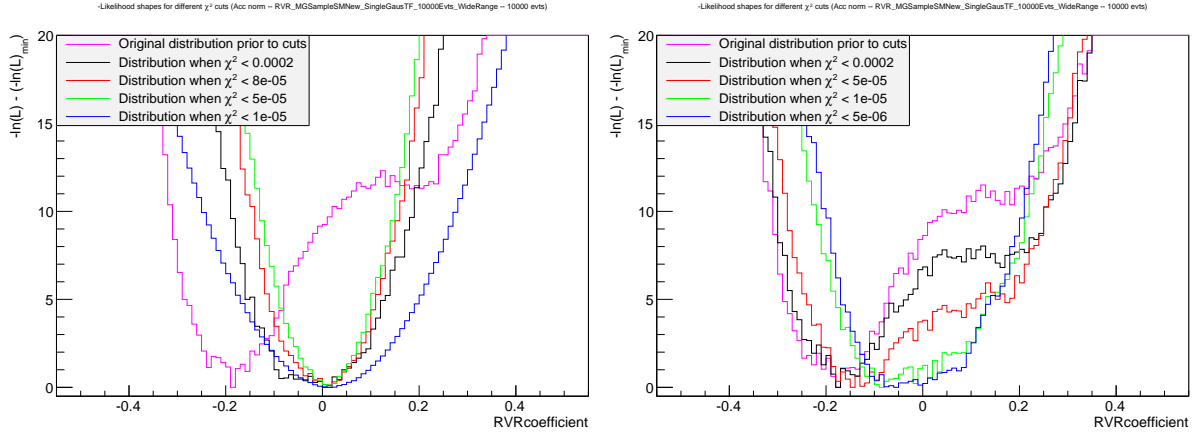


Figure 18.5: Overall $\ln(\mathcal{L})$ distribution for MG samples created with $V_R = 0.0$ obtained from the first fit (left) and the second fit (right) prior to any p_T -cut requirement. The different χ^2 cuts applied correspond to percentages of about!!

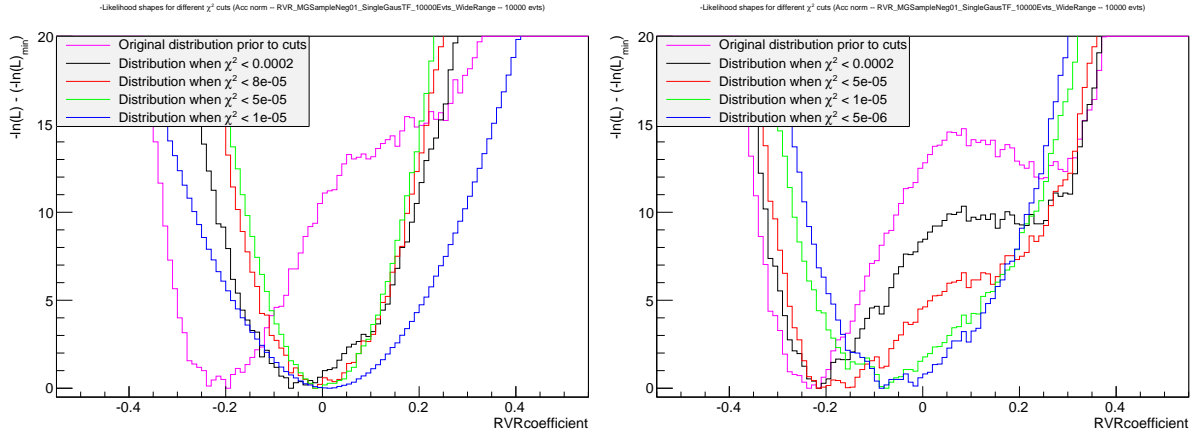


Figure 18.6: Overall $\ln(\mathcal{L})$ distribution for MG samples created with $V_R = -0.1$ obtained from the first fit (left) and the second fit (right) prior to any p_T -cut requirement. The different χ^2 cuts applied correspond to percentages of about!!

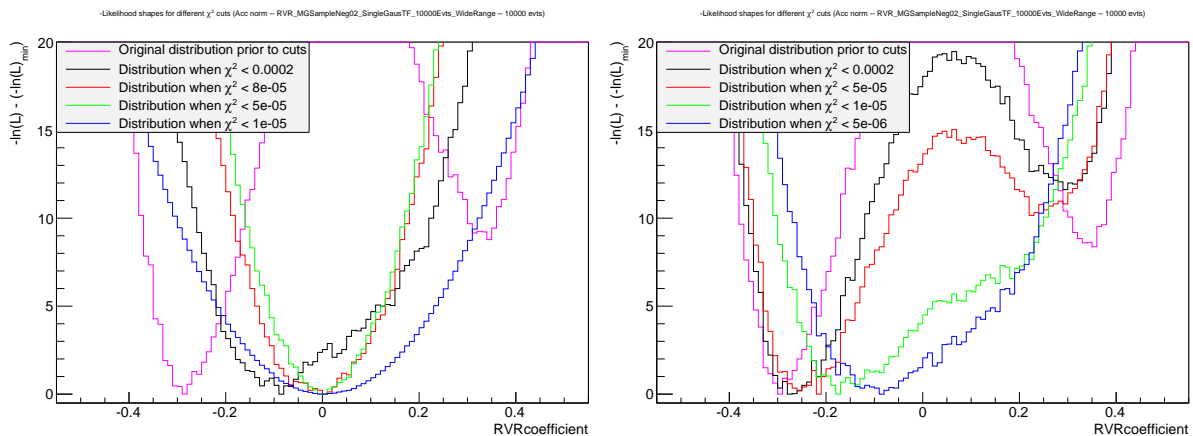


Figure 18.7: Overall $\ln(\mathcal{L})$ distribution for MG samples created with $V_R = -0.2$ obtained from the first fit (left) and the second fit (right) prior to any p_T -cut requirement. The different χ^2 cuts applied correspond to percentages of about!!

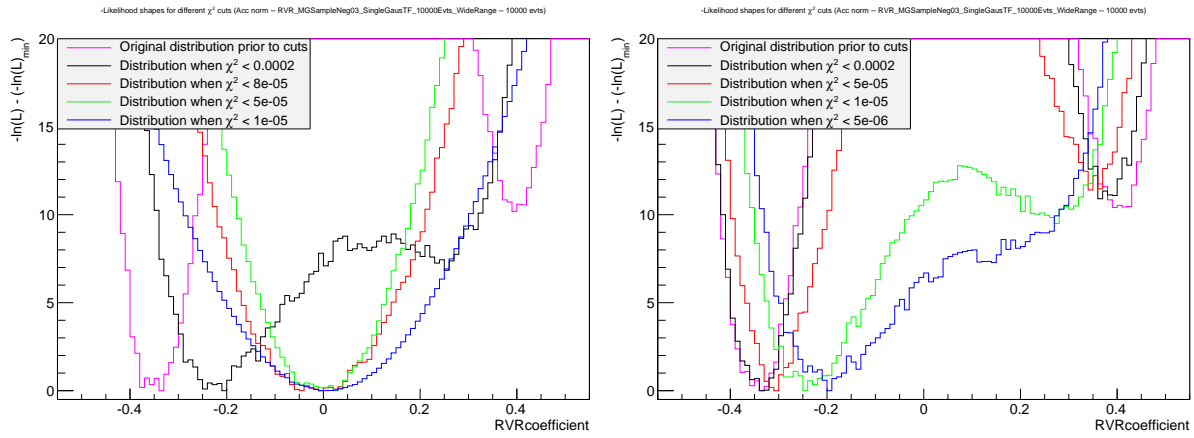


Figure 18.8: Overall $\ln(\mathcal{L})$ distribution for MG samples created with $V_R = -0.3$ obtained from the first fit (left) and the second fit (right) prior to any p_T -cut requirement. The different χ^2 cuts applied correspond to percentages of about!!

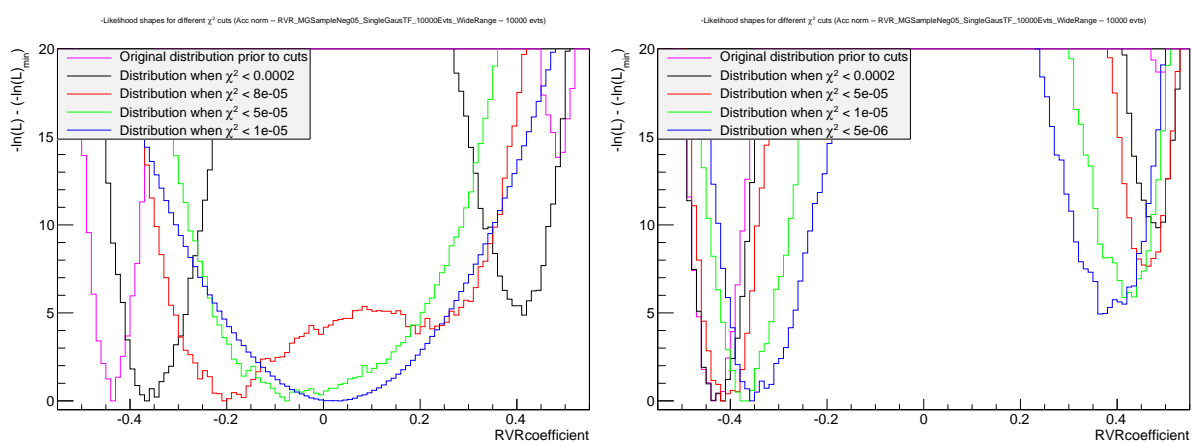


Figure 18.9: Overall $\ln(\mathcal{L})$ distribution for MG samples created with $V_R = -0.5$ obtained from the first fit (left) and the second fit (right) prior to any p_T -cut requirement. The different χ^2 cuts applied correspond to percentages of about!!

Chapter 19

Results from g_R coefficient

The benefit of looking also at the g_R coefficient, and not only focussing on the V_R one is that the relative changes in kinematics for this right-handed tensor coupling are expected to be much larger. This is explained by the way the coefficient enters the width formulas and the mixing which occurs with the V_R coefficient.

This different sensitivity is clearly visible in Figure 19.1. An additional bonus for the g_R coefficient is that the distributions are not symmetrical compared to 0.0 allowing the use of a simple second-order polynomial instead of a more complex 4th order one which is needed for the V_R case.

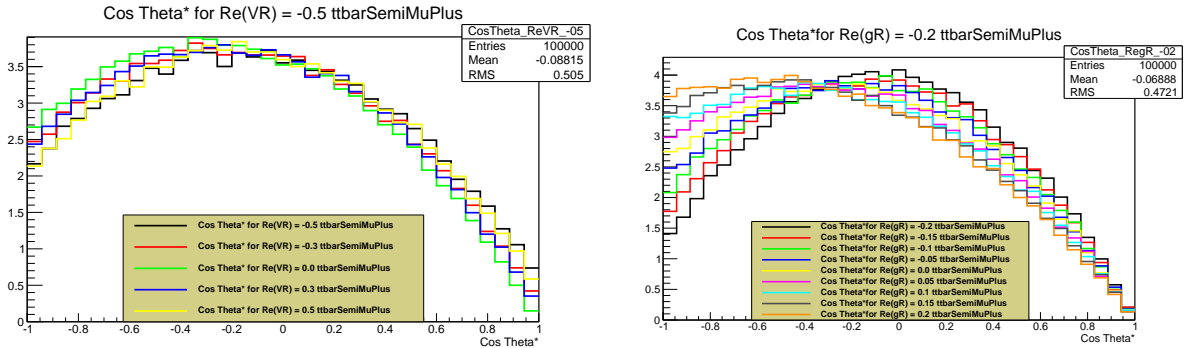


Figure 19.1: Stronger dependence of the $\cos\theta^*$ distribution on the g_R coefficient than on the V_R one. Therefore the g_R coefficient will be measured in a more narrow range than the one used for the V_R measurement.

19.1 Results prior to any pT-cuts

The first results for this g_R coefficient are given in Figure 19.2 which shows the obtained likelihood distribution for most of the g_R values in the studied range:

$$g_R \in [-0.2, -0.15, -0.1, -0.05, 0.0, 0.05, 0.1, 0.15, 0.2] \quad (19.1)$$

Currently the result for $g_R = 0.1$ is still missing together with the values at the outer edges of the considered range. These last two are missing since the results for $g_R \pm 0.15$ seem to suggest that values further away from the expected Standard Model configuration value do not agree anymore with the simulated value. For all the smaller g_R

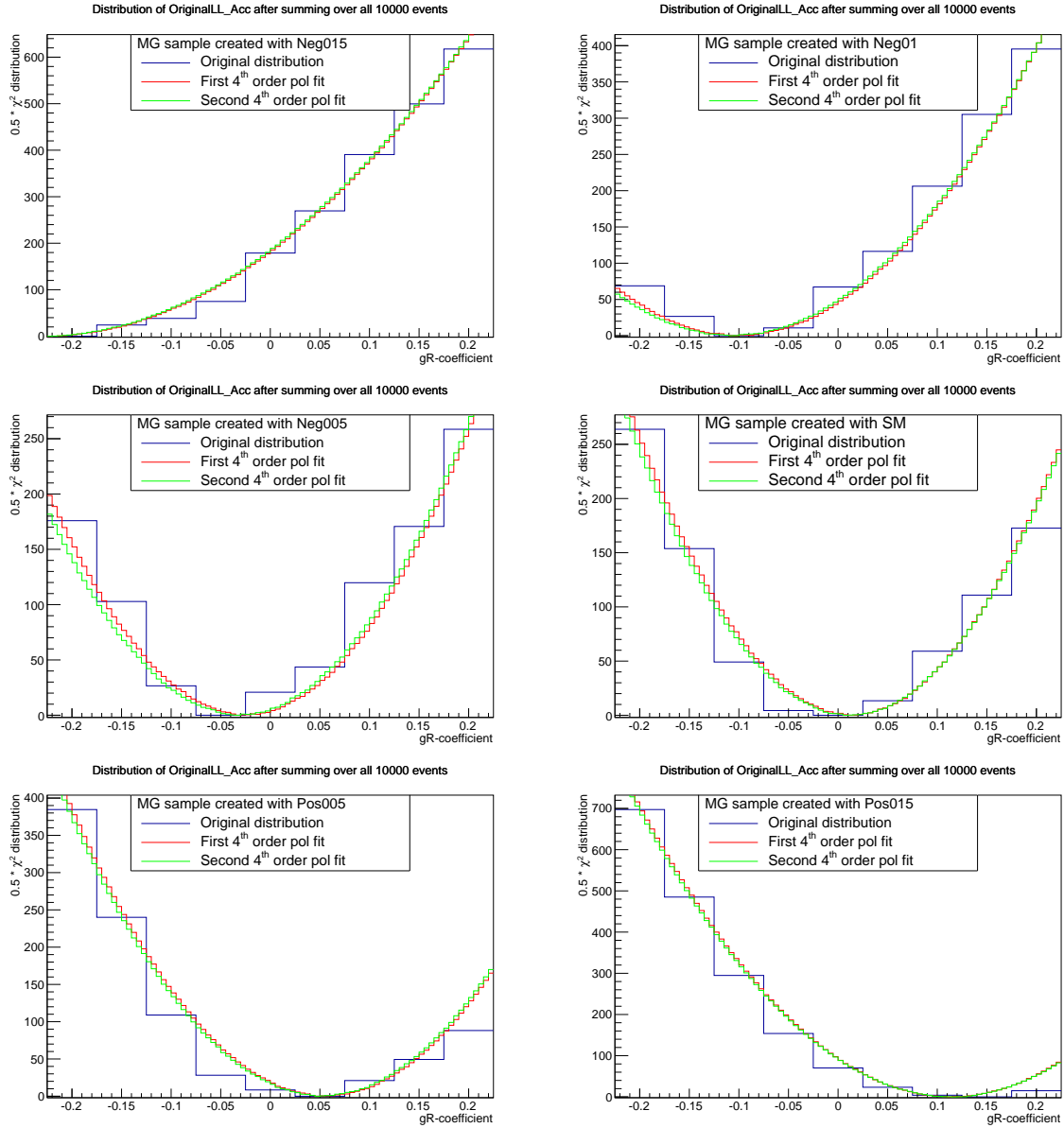


Figure 19.2: Obtained $\ln(\mathcal{L})$ distribution for MadGraph samples created with different g_R values. From top left to bottom right the values used are -0.15, -0.01, -0.05, 0.0, 0.05 and 0.15 respectively.

values a nice agreement is found with the value used for generating the MadGraph sample.

From these $\ln(\mathcal{L})$ distributions can be concluded that the correct g_R coefficient is recovered for most of the considered MadGraph samples. However the deviation from the outer edges of the range are clearly visible and should be investigated further by looking at the result for a MadGraph sample created with $g_R = 0.1$.

Also the presence of large deviations in the kinematics, even for low changes in g_R , opens the possibility to add the $g_R = 0.025$ parameter to improve the accuracy close to the Standard Model expectation value.

19.2 Results afer applying the event selection cuts

Since it is possible that MadWeight and MadGraph have different event cleaning procedures for low-momentum events, it is interesting to study the likelihood distributions with a full event selection applied. The one which is currently used is the following:

Table 19.1: Event selection constraints applied for the MadGraph samples created.

	pT-cut	η	ΔR
jet	30 GeV	2.5	0.3
lepton	26 GeV	2.5	0.3
neutrino	25 GeV	2.5	0.3

Another important difference with respect to the $\ln(\mathcal{L})$ distributions shown before is the adapted range which is made significantly wider in order to capture the possible minima that might occur further away from the expected Standard Model value. The considered range is given below but for the moment only the $\ln(\mathcal{L})$ distributions for the cases -0.15 , 0.0 and 0.05 have been calculated.

$$[-0.5, -0.3, -0.2, -0.15, -0.1, -0.05, -0.025, 0, 0.025, 0.05, 0.1, 0.15, 0.2, 0.3, 0.5] \quad (19.2)$$

The result for these three g_R configurations is given in the Figure 19.3.

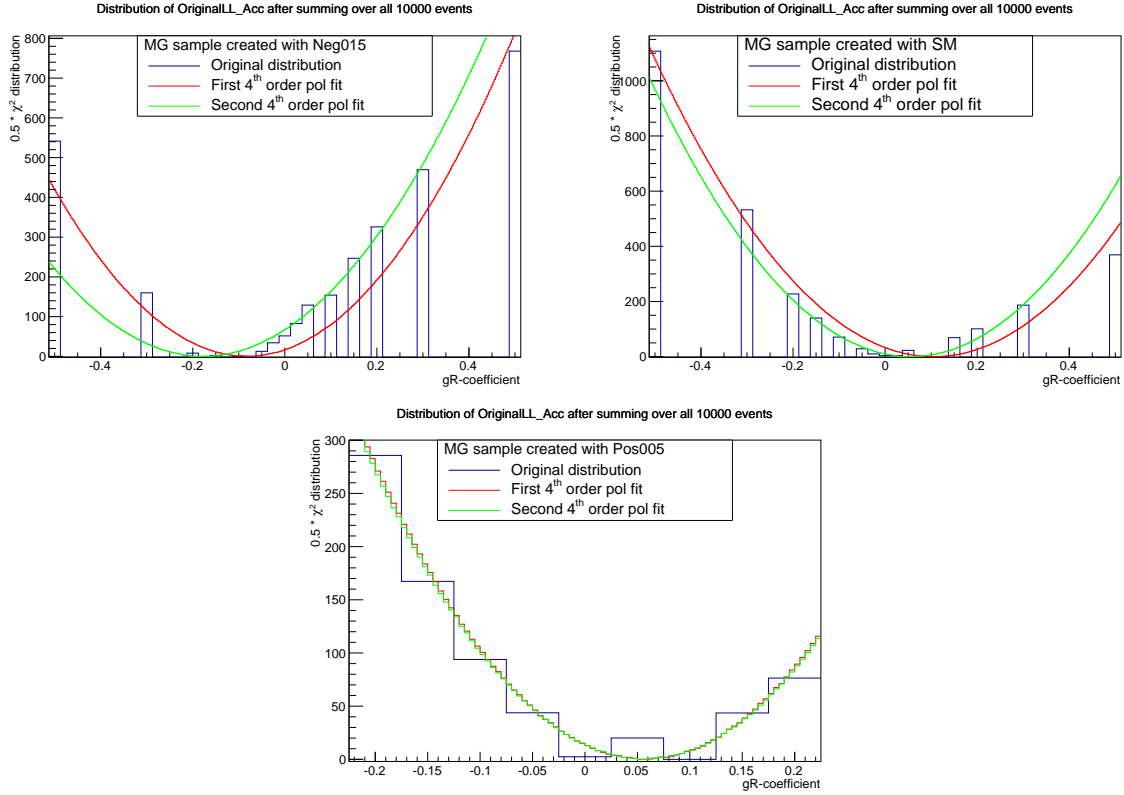


Figure 19.3: Obtained $\ln(\mathcal{L})$ distributions from three configurations when the above-mentioned event selection constraints have been applied (Table 19.1). The final distribution is still lacking additional information from the extended range.

The biggest improvement is obtained for the configuration where $g_R = -0.15$ since the applied event selection also ensures that the “almost” the correct minimum is retrieved.

However it seems that also the enlarged range plays an important role.

The Standard Model configuration does not correspond that well with the expected minimum but this is maybe caused by an issue with the cross-section calculated for $g_R = 0.05$ which is for both the *SM* as the *Pos005* case larger than the surrounding configurations.
TO CHECK!

Also mention something about the chi-sq distributions!

19.2.1 Including $\cos \theta^*$ reweighting

A next step in the event-selection calculations is applying the $\cos \theta^*$ reweighting which corrects the $\cos \theta^*$ distribution for the applied event selection constraints. As before this weight is determined for each event by comparing the $\cos \theta^*$ value prior to the applied cuts with the value obtained after these event selection is applied.

$$weight = \frac{\cos \theta_{All}^*}{\cos \theta_{Cut}^*} \quad (19.3)$$

This results in a weight for each event but in order to apply the reweighting correctly to the MadWeight output this weight should be equal for each of the g_R configurations. If this would not be the case the $\cos \theta^*$ reweighting should be determined individually for each of the considered g_R configurations considered in the studied range. This would definitely complexify the application of this reweighting procedure.

Hence the obtained $\cos \theta^*$ fraction for each of the g_R configurations has been plotted together in Figure 19.4, which shows a nice agreement between the different g_R configurations although a clear discrepancy is visible for the so-called *Neg05* case.

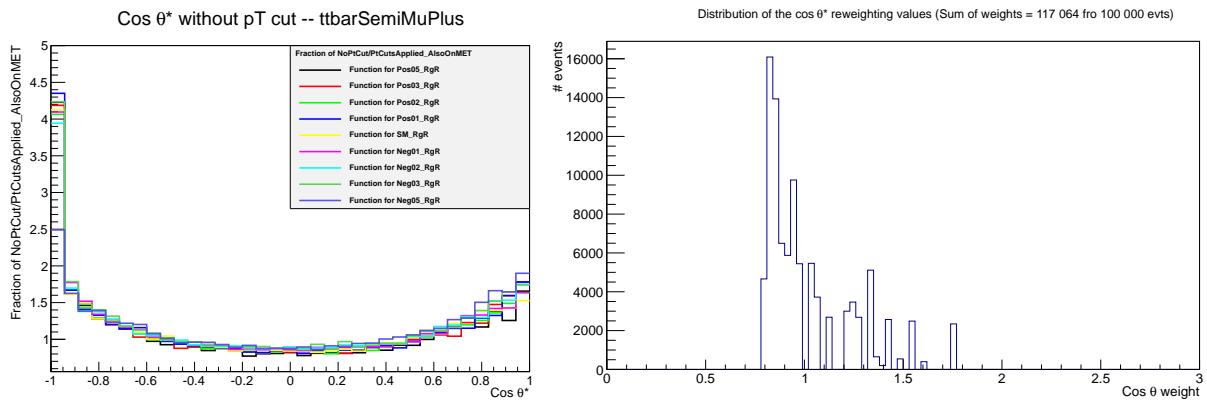


Figure 19.4: Fraction of $\cos \theta^*$ distribution before and after event selection cuts have been applied for all the different g_R configurations considered. They all have a similar distribution with the exception of the *Neg05* case. (left) Distribution of the obtained $\cos \theta^*$ weight for all the events in the *Pos015* case. (right)

The weights obtained for the g_R configuration are not yet normalised as can be seen from the title of the right-handed distribution in Figure 19.4. This makes the application of this $\cos \theta^*$ reweighting a bit more challenging since it implies that an additional normalisation factor should be introduced in order to ensure correct implementation of this reweighting procedure.

Remark: Maybe interesting to check whether the weight remains similar (maybe also

for the V_R case) when only a reduced number of events is considered! This because the $\cos \theta^*$ weights are determined using 100 000 events but only 10 000 events or less are considered during the MadWeight calculations which might distort the normalisation of this reweighting procedure ...

For the moment the $\cos \theta^*$ reweighting is applied without altering the normalisation and the obtained distributions are given in Figure 19.5, again for the same limited number of g_R configurations which is currently calculated by MadWeight. The calculations of the other g_R parameters will be done as soon as possible in order to ensure a similar behaviour for configurations further away from the Standard Model.

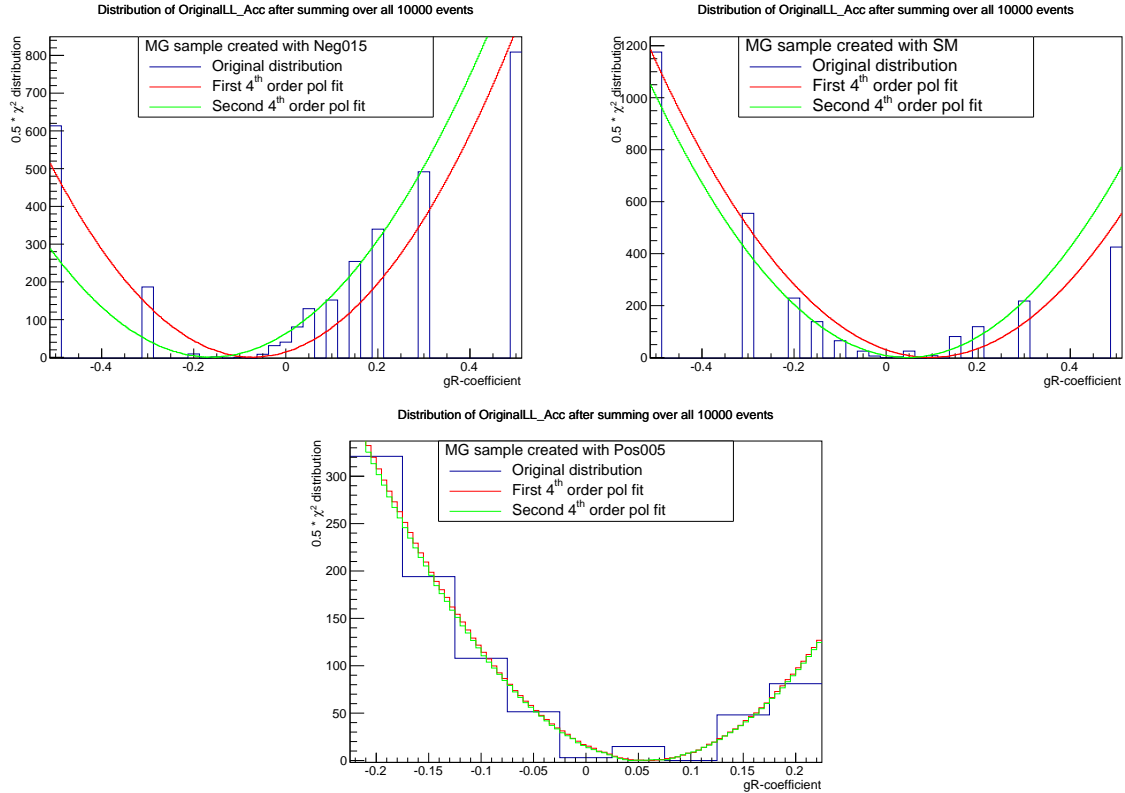


Figure 19.5: Obtained $\ln(\mathcal{L})$ distributions from three configurations when the above-mentioned event selection constraints have been applied together with the $\cos \theta^*$ reweighting (Table 19.1). The final distribution is still lacking additional information from the extended range.

The influence of this $\cos \theta^*$ reweighting procedure is extremely small and is almost only visible by the different range of the y-axis in the distributions in Figure 19.3 and 19.5. The current implementation of this reweighting is given in Equation (19.4) and has an effect on both the MadWeight probability and the cross-section normalisation. The detailed influence of this $\cos \theta^*$ reweighting procedure is summarised in Figure 19.6, which contains the $\ln(\mathcal{L})$ distribution for the first polynomial fit before and after this reweighting is applied.

$$\mathcal{L}^{\cos \theta^*} = \sum (-\ln P_{evt}^{MW} + \ln \sigma) * weight_{\cos \theta^*, evt} \quad (19.4)$$

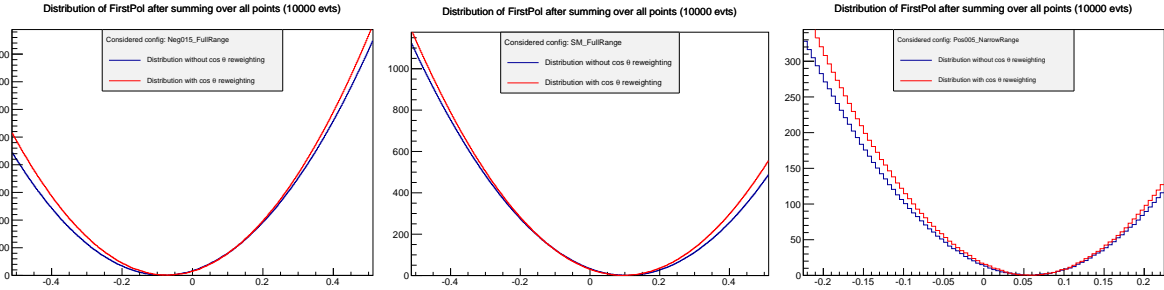


Figure 19.6: Influence of the $\cos \theta^*$ reweighting procedure for the three g_R configurations currently studied.

Remark: Rather unexpected that the influence of this $\cos \theta^*$ reweighting procedure is so small, especially when keeping in mind the large shape difference obtained in the V_R case. The implementation used seems to be correct since the goal of this reweighting is to include an event with weight x x times in the sum over the events. (*Or should it also be inside the logarithm??*)

19.2.2 Adding additional constraint on slope of fit

A second point which has been studied in order to further improve the $\ln(\mathcal{L})$ distributions for the different g_R configurations was the value of the second derivative which gives an idea whether the $\ln(\mathcal{L})$ distribution has the desired minimum-like shape or the maximum-like shape. Since the g_R distributions can be fitted with a simple 2nd polynomial fit it makes sense to require this second derivative to be positive.

When looking at all the events which have been studied rather a lot actually have this undesired maximum-like shape as can be seen from Figure 19.7 which shows the value of this second derivative for the first polynomial fit.

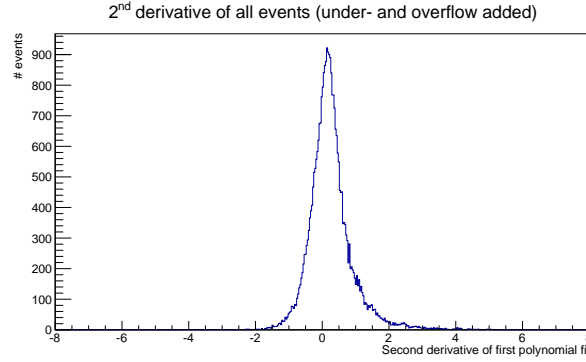


Figure 19.7: Distribution of second derivative of polynomial fit (Neg015 case).

Therefore the $\ln(\mathcal{L})$ distributions obtained when requiring this second derivative to be positive were created and compared to the ones obtained when combining all events. Strangely enough this requirement does not result in a nice minimum-like overall $\ln(\mathcal{L})$ distribution but gives a distribution which does not agree at all with the expectations. This is shown in Figure 19.8 which contains the $\ln(\mathcal{L})$ distributions for events with positive second derivative.

So this requirement is clearly not sufficient and does not result in the desired improvement. Hence detailed study of the events removed by this requirement should be done

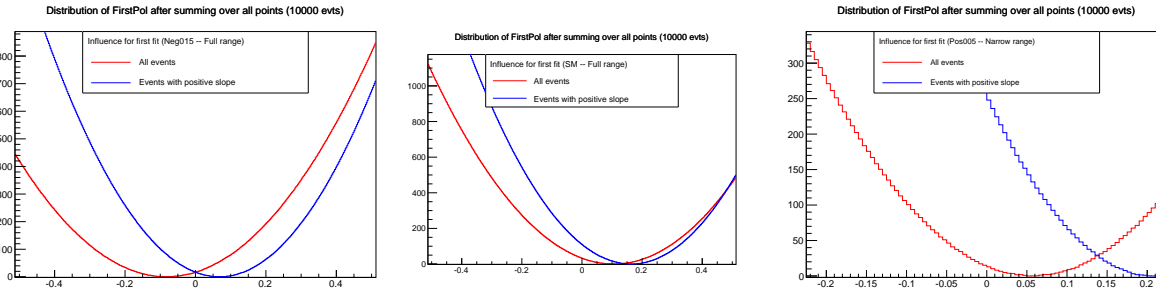


Figure 19.8: Comparison between the $\ln(\mathcal{L})$ distribution (first polynomial fit) when all events are used (red) and when only the events which have a positive second derivative are considered (blue). This selection requirement clearly does not result in the desired improvement ...

since this result seems to suggest that in order to obtain a correct $\ln(\mathcal{L})$ minimum the so-called *wrong* events have to be incorporated in order to end up with an overall shape which matches with expectation. It still is very strange that the obtained result is so sensitive to these type of constraints and therefore a sample with 50 000 instead of the currently studied 10 000 events is being processed by MadWeight. This will hopefully be able to help decide whether these large changes can be caused by a kind of statistical fluctuations or whether there is really a profound physics reason behind...

Another variable which was considered in order to serve as a “weight cleaning” requirement was the *slope steepness*. This variable looks at the difference in value between the outermost point and the expected minimum point such that it gives an idea of the sharpness of the individual $\ln(\mathcal{L})$. From Figure 19.9 can be seen that the slope steepness does not have the same sign as the second derivative of the fit and can therefore maybe be combined with this previous constraint. Figure 19.10 confirms that the same behaviour is recovered for the Standard Model case and the *Neg015* one.

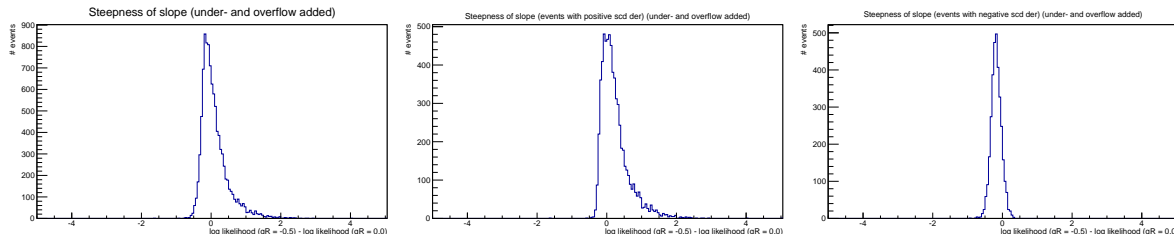


Figure 19.9: Steepness of the slope using MadWeight probabilities (so no fit information is used) for the Standard Model configuration.

Rather strange that these two plots are so identical ... Would expect much less steep slope in the “Neg015” case since the two points are located much closer together than in the “SM” case.

But also this does not result in the desired improvement, it even seems that requiring this “slope steepness” to be positive again makes the position of the minimum deviate further from the expected minimum ... The example given in Figure 19.11 is the distribution obtained for the Standard Model configuration. It contains the comparison between the original $\ln(\mathcal{L})$ distribution, the one where only the slope is required to be positive and finally the distribution where both slope and steepness are constrained.

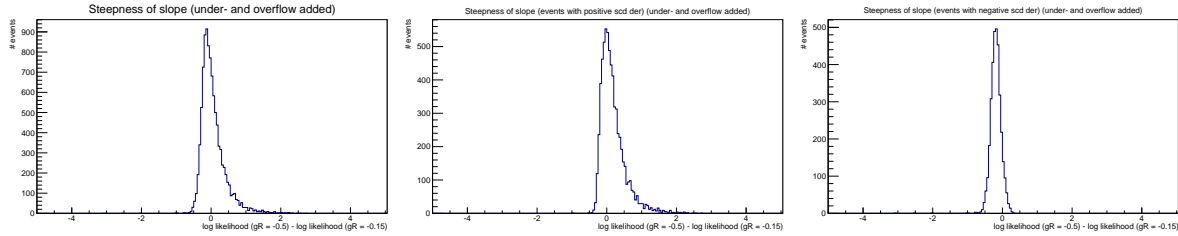


Figure 19.10: Steepness of the slope using MadWeight probabilities (so no fit information is used) for the *Neg015* configuration.

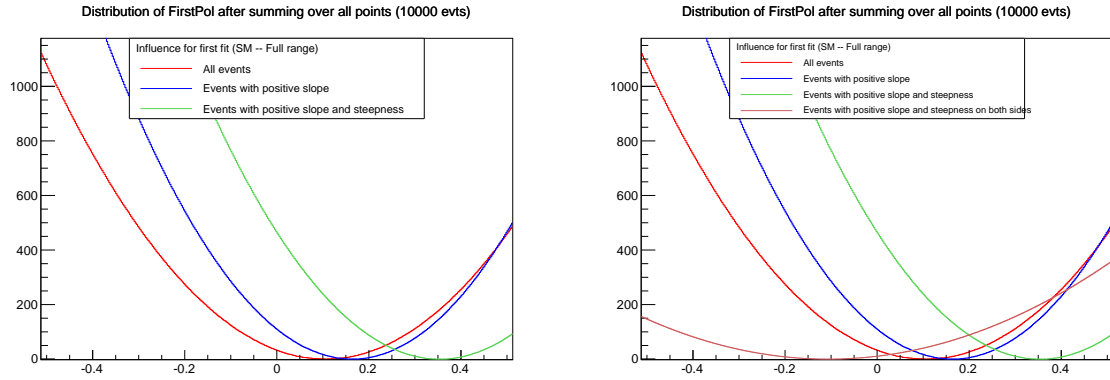


Figure 19.11: Comparing the $\ln(\mathcal{L})$ distributions for events with a positive second derivative (obtained from fit) and a positive difference between the outermost g_R point (-0.5) and the expected minimum value (0.0) for the Standard Model case. The second distribution also contains the additional requirement that the slope on the other side should be negative.

19.3 Cross-section dependency

As a test to determine how sensitive the obtained $\ln(\mathcal{L})$ distributions are to the used cross-section value for normalisation a sort of scaling of the cross-section has been applied. This is applied by multiplying the cross-section value for a specific g_R configuration with the following function:

$$f(g_R) = 1 + g_R * x \quad \text{with } x = \{-0.1, -0.05, 0, 0.05, 0.1\} \quad (19.5)$$

Since the cross-section normalisation term is a logarithmic term it was expected that even small changes in the cross-section can have enormous effects, and this is indeed what is found and summarised in Figure 19.12. Strangely enough the event selection constraints applied for the bottom two configurations do not seem to reduce the dependency on this cross-section value. Since here the cross-section values are drastically reduced by these cuts it would seem more logical that the variations between the different scalings considered become less pronounced, but this is clearly not the case ...

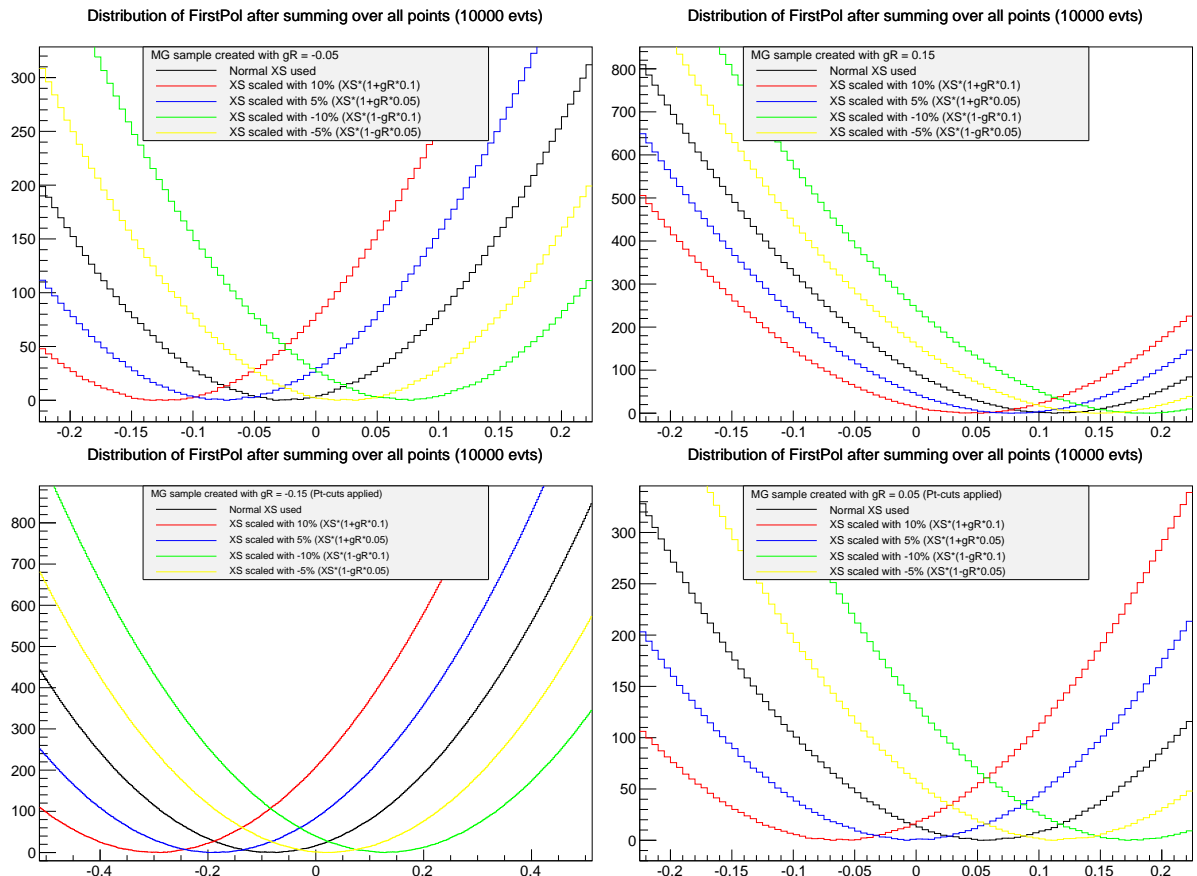


Figure 19.12: Influence of the considered cross-section scaling both with and without event selection constraints applied.